Inaugural dissertation

for

obtaining the doctoral degree

of the

Combined Faculty of Mathematics, Engineering and Natural Sciences

of the

Ruprecht - Karls - University

Heidelberg

Presented by

Iris Christiane Müller

born in Worms, Germany

Oral examination: 27.11.2023

Inhibiting glucocorticoid receptor signalling in tumour-associated macrophages for anti-tumour immune response

Referees:

Prof. Dr. Viktor Umansky

Prof. Dr. Astrid Schmieder

Summary

Cancer immunotherapy has made strong impact on the treatment of many cancers, particularly malignant melanoma. However, primary and secondary resistance remains a major challenge. Tumour-associated macrophages (TAMs) represent the most abundant immune cell type within the tumour, and despite their inherent potential for immune stimulation, TAMs predominantly exert tumour-promoting functions through immune suppression. This occurs due to signals from the tumour microenvironment (TME) that drive TAMs towards a pro-tumour phenotype, thus promoting a tumour-permissive milieu. Recently, tumour-derived glucocorticoids (GCs) were identified as a mechanism for evading the immune response in tumours, impeding both anti-tumour T cell responses and the effectiveness of cancer immunotherapy. The impact of tumour-derived GCs on the function of TAMs remains largely unknown. The present thesis aimed to investigate the role of GC-responsive TAMs in melanoma that is resistant to aPD-1 checkpoint immunotherapy. Genetic ablation of the glucocorticoid receptor (GR) in monocyte-macrophage lineage cells decreased tumour growth and restored effectiveness of checkpoint immunotherapy in aPD-1–resistant melanoma. This was accompanied by reprogramming of immunosuppressive TAMs towards a more anti-tumour phenotype, however only moderate changes were observed in the T cell activation state. Bone marrow-derived macrophages (BMDM) were polarized with TCM/DEX/IL4 towards a TAM-like phenotype, characterized by strong upregulation of M2 phenotypic markers and high functional capacity to inhibit T cell proliferation. This was associated with increased HSD11B1 activity, amplifying local GC levels in a positive feed-forward mechanism. Notably, strong upregulation of HSD11B1 expression was also observed in checkpoint immunotherapy-resistant melanoma upon PD-1 mAb treatment. The small molecule GR inhibitor mifepristone (MF) readily inhibited TAM-like polarization and interrupted the self-reinforcing mechanism of GCs and HSD11B1 in BMDM. To test the capability of MF to repolarize GC-response immunosuppressive TAMs *in vivo*, lipid nanoparticles (LNPs) incorporating MF were produced by microfluidic mixing and conjugated to CD169 antibodies via click chemistry for active targeting of TAMs in the TME. MF-aCD169 LNPs efficiently reprogrammed immunosuppressive TAMs and improved the anti-tumour T cell response, restoring efficiency of checkpoint immunotherapy in aPD-1–resistant melanoma. Collectively, this thesis demonstrates that GC-responsive TAMs play a prominent role in suppressing anti-tumour immunity in aPD-1–resistant melanoma. Additionally, this thesis represents the first approach to reprogram immunosuppressive TAMs by GR blockade, sensitizing melanoma to checkpoint immunotherapy.

Zusammenfassung

Krebsimmuntherapien haben einen großen Beitrag zur Behandlung vieler Krebsarten geleistet, insbesondere des malignen Melanoms. Dennoch stellen primäre und sekundäre Resistenzen nach wie vor eine große Herausforderung dar. Tumor-assoziierte Makrophagen (TAM) sind die häufigste Immunzellart im Tumor und trotz ihrer Fähigkeit zur Immunstimulation üben TAM vorwiegend tumorfördernde Funktionen aus. Dies geschieht aufgrund von Signalen aus der Tumormikroumgebung (TME), die TAM zu einem protumoralen Phänotyp polarisieren und somit ein tumorbegünstigendes Milieu schaffen. Kürzlich wurde die Freisetzung von Glucocorticoiden (GCs) aus dem Tumor als Mechanismus zur Umgehung der Immunantwort im Tumor identifiziert. Der Einfluss der vom Tumor freigesetzten GCs auf die Funktion der TAM ist weitgehend ungeklärt. Die vorliegende Thesis hatte zum Ziel, die Rolle GC-empfänglicher TAM in Melanomen zu untersuchen, die gegen aPD-1 Checkpoint-Inhibitoren resistent sind. Genetische Ausschaltung des GC Rezeptors (GR) in Zellen der Monozyten-Makrophagen-Linie verringerte das Tumorwachstum und stellte die Wirksamkeit der Checkpoint-Inhibitoren in aPD-1-resistenten Melanomen wieder her. Dies ging einher mit der Reprogrammierung der TAM zu einem stärker antitumoralen Phänotyp, allerdings wurden nur moderate Veränderungen im Aktivierungszustand der T-Zellen beobachtet. Knochenmarksmakrophagen (KMM) wurden mit TCM/DEX/IL4 zu einem TAM-ähnlichen Phänotyp polarisiert, was sich durch eine starke Expression von M2-Phänotyp-Markern und einer hohen funktionellen Kapazität zur Hemmung der T-Zell-Proliferation zeigte. Dies ging einher mit einer erhöhten HSD11B1 Aktivität, die die lokalen GC-Spiegel in einem positiven Rückkopplungsmechanismus verstärkte. Bemerkenswerterweise wurde auch in immuntherapieresistenten Melanomen nach PD-1-mAb-Behandlung eine starke HSD11B1 Expression beobachtet. Der Small Molecule GR-Inhibitor Mifepriston (MF) hemmte die TAM-ähnliche Polarisation und unterbrach den selbstverstärkenden Mechanismus von GCs und HSD11B1 in KMM. Um den Effekt von MF auf TAM *in vivo* zu testen, wurden MF-beladene Lipidnanopartikel durch Microfluidic Mixing hergestellt, und über click chemistry an CD169-Antikörper gekoppelt, um ein aktives Targeting der TAM im TME zu ermöglichen. MF-aCD169-LNPs programmierten immunsuppressive TAM effizient um und verbesserten die antitumorale Antwort der T-Zellen, was die Wirksamkeit der Checkpoint-Inhibitoren in aPD-1-resistenten Melanomen wiederherstellte. Zusammenfassend zeigt diese Thesis, dass GC-empfängliche TAM eine wichtige Rolle bei der Unterdrückung der antitiumoralen Immunität in aPD-1-resistenten Melanomen spielen. Darüber hinaus stellt diese Thesis den ersten Ansatz zum Umprogrammieren immunsuppressiver TAMs durch GR-Blockade dar um das Melanom für eine Checkpoint-Immuntherapie zu sensibilisieren.

Table of contents

List of abbreviations v
List of tables vii
List of figures vii
1 Introduction 1
1.1 Cancer immunology 1
1.2 Malignant melanoma 2
1.2.1 Targeted therapy 3
1.2.2 Immunotherapy 3
1.3 Tumour-associated macrophages (TAM) 4
1.3.1 Origin and role of macrophages in cancer 4
1.3.2 Functions of TAMs in the tumour microenvironment 5
1.3.3 TAM targeting for cancer immunotherapy 6
1.3.4 Specific targeting of CD169+ TAMs for cancer immunotherapy 7
1.4 Glucocorticoids 7
1.4.1 Glucocorticoid biosynthesis 7
1.4.2 Regulation of glucocorticoid production and activity 8
1.4.3 Glucocorticoid receptor signalling 10
1.5 Nanocarriers for drug delivery 11
1.5.1 Nanocarrier systems 11
1.5.2 Passive targeting of nanocarriers 12
1.5.3 Active targeting of nanocarriers 13
2 Aim of the study 14
3 Materials 15
3.1 Technical equipment 15
3.2 Software 15
3.3 Consumables 16
3.4 Chemicals, solvents and reagents 16
3.5 Antibodies 18
3.5.1 Unconjugated antibodies 18
3.5.2 Conjugated antibodies 18
3.5.3 Therapeutic antibodies 19
3.6 Growth factors, stimulants and drugs 20

3.6.1 Growth factors 20
3.6.2 Stimulants 20
3.6.3 Drugs 20
3.7 Commercial kits 20
3.8 Buffers and media 20
3.9 Primers 21
3.9.1 PCR Primer 21
3.9.2 qPCR Primer 21
3.10 Mice and cell lines 22
3.10.1 Mice 22
3.10.2 Cell lines 22
4 Methods 23
4.1 Cell culture methods 23
4.1.1 Cell lines 23
4.1.2 Cell counting 23
4.1.3 Cell line freezing and thawing 23
4.1.4 Preparation of tumour-conditioned medium 24
4.2 *In vivo* studies 24
4.2.1 Mouse breeding and keeping 24
4.2.2 Initiation of mouse melanoma models 25
4.2.3 *In vivo* imaging and biodistribution of lipid nanoparticles 25
4.3 Tissue dissection and isolation of primary cells 26
4.3.1 Skin tumour preparation 26
4.3.2 Splenocyte isolation 26
4.3.3 Kupffer cell isolation 26
4.3.4 Bone marrow cell isolation 27
4.3.5 *Ex vivo* culture of tissue explants 27
4.4 Cell separation 27
4.4.1 Flow cytometry 27
4.4.2 Magnetic-activated cell sorting (MACS) 28
4.5 Primary cell culture 28
4.5.1 Generation and polarization of bone marrow-derived macrophages 28
4.5.2 Fluorometric assay of Calc-aCD169 treated BMDM 28
4.6 Functional assays 29
4.6.1 Enzyme-linked immunosorbent assay (ELISA) 29

4.6.2 11β-HSD1 activity assay 29
4.6.3 Suppression of T cell proliferation assay 29
4.7 Gene expression 29
4.7.1 RNA extraction, reverse transcription, and quantitative PCR (qPCR) 29
4.7.2 DNA extraction, PCR, and agarose gel electrophoresis 30
4.8 Formulation of lipid nanoparticles 30
4.8.1 Preparation of lipid nanoparticles 30
4.8.2 Particle size determination 31
4.8.3 Determination of drug loading 31
4.8.4 Antibody functionalization and conjugation to lipid nanoparticles 31
4.9 Statistical analysis 32
5 Results 33
5.1 Expression of steroidogenic enzymes in murine tumour tissue 33
5.2 Knockout of GR in TAM reduces tumour growth in murine melanoma models 34
5.3 Expression patterns of Cre recombinase in macrophage-Cre mouse strains 40
5.4 Ablation of TAM expressed GR restores effectiveness of checkpoint immunotherapy in aPD-1–resistant melanoma 42
5.5 Macrophages are polarized towards an immunosuppressive phenotype by GCs 46
5.5.1 Generation of TAM-like BMDM *in vitro* by GR activation 46
5.5.2 Mifepristone (RU-486) inhibits activation of the GR signalling pathway 47
5.5.3 GR-mediated inhibition of pro-inflammatory mediator release 47
5.6 The positive feed-forward mechanism of GCs and 11β-HSD1 48
5.6.1 GR activation induces high expression of *HSD11B1* in BMDM 48
5.6.2 *HSD11B1* is upregulated in tumours that fail to respond to antiPD-1 checkpoint immunotherapy 50
5.6.3 *HSD11B1* expression in human melanomas 52
5.7 Capacity of GR-activated TAM-like BMDM in inhibiting T cell proliferation 53
5.8 Functionalized nanoparticles targeting TAMs as cancer therapy 54
5.8.1 Production and characterization of MF-loaded LNPs 54
5.8.2 Influence of flow rate ratio and total flow rate on the limit size of LNPs 54
5.8.3 Influence of the lipid composition on the limit size of LNPs 56
5.8.4 MF can be efficiently loaded into limit size LNPs 57
5.8.5 Modification of MF-loaded LNPs for CD169 targeting 59
5.8.6 Specificity and cellular uptake of CD169-targeting LNPs 60
5.8.7 CD169-targeted MF inhibits immunosuppressive polarization of BMDM 61

5.8.8 *In vivo* biodistribution of CD169-targeted LNPs in tumour-bearing mice.....62
5.9 Administration of MF-aCD169 and PD-1 mAbs produced an anti-tumour effect in aPD-1-resistant melanoma.....64
6 Discussion.....70
6.1 Conclusion.....79
7 References.....80
8 Acknowledgments.....96

List of abbreviations

11-DHC	11-dehydrocorticosterone
ACTH	adrenocorticotropic hormone
BMC	bone marrow cells
BMDM	bone marrow-derived macrophages
B-Raf	B-rapidly accelerated fibrosarcoma
Calc	calcein
CBG	corticosteroid binding globulin
CCL2	CC chemokine ligand 2
CCR2	CC chemokine receptor type 2
CFS-1	macrophage colony-stimulating factor 1
CFSE	carboxyfluorescein succinimidyl ester
Ciita	class II major histocompatibility complex transactivator
CM	cutaneous melanoma
COX	cyclooxygenase
CRH	corticotropin releasing hormone
CTLA-4	T-lymphocyte-associated antigen 4
Ctrl	control
CXCL	C-X-C motif ligand
Cyp	cytochrome P450
DBD	DNA-binding domain
DC	dendritic cell
DEX	dexamethasone
DLS	dynamic light scattering
DNA	deoxyribonucleic acid
EDTA	ethylenediamine tetraacetic acid
EGF	epidermal growht factor
ELISA	enzyme-linked immunosorbent assay
ER	endoplasmatic reticulum
ERK	extracellular signal-regulated kinase
FACS	fluorescence-activated cell sorting
FBS	fetal bovine serum
FMO	fluorescence minus one
FRR	flow rate ratio
GC	glucocorticoid
GEPIA	gene expression profiling interactive analysis
GM-CSF	granulocyte-macrophage colony-stimulating factor
GR	glucocorticoid receptor
GRE	GC responsive element
HEPES	4-(2-hydroxyethyl) piperazine-1-ethanesulfonic acid
HPA	hypothalamic-pituitary-adrenal
HPLC	high performance liquid chromatography
HSD11B	11β-hydroxysteroid dehydrogenase
i.p.	intraperitoneal
i.v.	intravenous

ICI	immune checkpoint inhibitor
ICOS	inducible T cell costimulator
IFN	interferon
IL	interleukin
KC	kupffer cell
LAG-3	lymphocyte-activation gene 3
LBD	ligand binding domain
LNP	lipid nanoparticle
mAb	monoclonal antibody
MACS	magnetic-activated cell sorting
MAPK	mitogen-activated protein kinase
MARCO	macrophage receptor with collagenous structure
M-CSF	macrophage colony-stimulating factor
MEK	mitogen-activated protein kinase kinase
MF	mifepristone (RU-486)
mG	membrane-targeted EGFP
MHC-II	major histocompatibility complex class II
MMP	matrix metallopeptidase
MN	monocyte
Mrc1	mannose receptor C-type 1
mT	membrane-targeted tdTomato
NEAA	non-essential amino acids
NK cell	natural killer cell
Nr3c1	nuclear receptor subfamily 3 group c member 1
N-Ras	neuroblastoma RAS viral oncogene homolog
NTA	nanoparticle tracking analysis
NTD	N-terminal transactivation domain
P/S	penicillin/streptomycin
PBS	phosphate-buffered saline
PCR	polymerase chain reaction
PD	polydispersity
PD-1	programmed cell death protein 1
PFS	progression-free survival
POMC	proopiomelanocortin
qPCR	quantitative polymerase chain reaction
RBC	red blood cell
RES	reticuloendothelial system
RP-HPLC	reversed phase high performance liquid chromatography
RPM	red-pulp macrophage
RT	room temperature
s.c.	subcutaneous
SERPIN	serpin protease inhibitor
SHM	staggered herringbone micromixer
SKCM	skin cutaneous melanoma
Sn	sialoadhesin
STAB1	Stabilin-1

StAR	steroidogenic acute regulatory protein
TAM	tumour-associated macrophage
TCGA	the cancer genome atlas
TCM	tumour-conditioned medium
TFR	total flow rate
TGF	transforming growth factor
TIL	tumour-infiltrating leukocyte
TIM-3	T cell immunoglobulin and mucin domain-containing protein 3
TME	tumour microenvironment
Treg	regulatory T cell
Tris	tris(hydroxymethyl)-aminomethan
T-VEC	talimogen laherparevec
UV	ultraviolet
VEGF	vascular endothelial growth factor
VISTA	V-domain immunoglobulin suppressor of T cell activation
WPM	white-pulp macrophage

List of tables

Table 1. Polydispersity of LNP formulations at different TFR and FRR. 56
Table 2. Polydispersity of LNP formulations from different lipid ratios. 57
Table 3. Polydispersity of LNP formulations encapsulating MF. 59

List of figures

Figure 1. The cancer immunoediting concept. 1
Figure 2. Glucocorticoid biosynthesis. 8
Figure 3. Schematic representation of the regulation of glucocorticoid levels by the hypothalamic-pituitary-adrenal axis and by 11β-hydroxysteroid dehydrogenase (11β-HSD) in peripheral tissue. 9
Figure 4. Representation of the LysM-cre x GR flox crossbreeding. 24
Figure 5. Representation of the CD163-cre x GR flox crossbreeding. 25
Figure 6. Expression of *Cyp11A1*, *HSD11B1* and *Nr3c1* in murine skin, spleen and tumour tissue. 33
Figure 7. Growth curves of B16-F10*luc2* tumours in $GR^{f/fLysMcre}$ mice. 34
Figure 8. FACS analysis of B16-F10*luc2* tumours in $GR^{f/fLysMcre}$ mice. 35
Figure 9. Growth curves of YUMM1.7 tumours in $GR^{f/fLysMcre}$ mice. 36
Figure 10. FACS analysis of YUMM1.7 tumours in $GR^{f/fLysMcre}$ mice. 37
Figure 11. Growth curves of B16-F10*luc2* tumours in $GR^{f/fCD163cre}$ mice. 38
Figure 12. Growth curves and FACS analysis of YUMM1.7 tumours in $GR^{f/fCD163cre}$ mice. 39
Figure 13. Schematic diagram of the *mT/mG* construct before and after Cre-mediated recombination. 40
Figure 14. Cre-mediated deletion in the spleen of LysM-cre and CD163-cre mT/mG reporter mice. 41
Figure 15. Response to aPD-1 checkpoint immunotherapy in $GR^{f/fLysMcre}$ mice. 42
Figure 16. Characterization of TAMs in PD-1 mAbs treated YUMM1.7 tumour-bearing $GR^{f/fLysMcre}$ mice. 43
Figure 17. Gating strategy of TILs in PD-1 mAbs treated YUMM1.7 tumour-bearing $GR^{f/fLysMcre}$ mice. 44
Figure 18. Characterization of TILs in PD-1 mAbs treated YUMM1.7 tumour-bearing $GR^{f/fLysMcre}$ mice. 45
Figure 19. GR inhibition blocks polarization towards an immunosuppressive phenotype in BMDM. 46
Figure 20. DEX and TCM/DEX/IL4 selectively inhibit IL-12 production by BMDM. 48

Figure 21. Upregulation of *HSD11B1* in BMDM upon GR activation. 49
Figure 22. Conversion of 11-DHC to corticosterone by 11β-HSD1 in TAM-like BMDM. 50
Figure 23. Expression of steroidogenic enzymes in tumour tissue. 51
Figure 24. Local production of corticosterone in the TME. 51
Figure 25. Correlation analysis of human SKCM TCGA datasets using the GEPIA tool. 52
Figure 26. Suppression of T cell proliferation by TAM-like BMDM. 53
Figure 27. Effect of FRR and TFR on the limit size of LNPs. 55
Figure 28. Effect of lipid composition on the limit size of LNPs. 57
Figure 29. LNP formulations encapsulating MF. 58
Figure 30. Schematic representation of antibody functionalization and conjugation to LNPs. 60
Figure 31. Time-resolved release of LNP-incorporated calcein targeted to CD169+ BMDM. 61
Figure 32. Delivery of MF to BMDM using aCD169-conjugated LNPs. 62
Figure 33. *In vivo* biodistribution of CD169-targeting LNPs in tumour-bearing mice. 63
Figure 34. Administration of MF-aCD169 and PD-1 mAbs inhibited tumour progression. 64
Figure 35. Gating strategy for TAMs. 65
Figure 36. Characterization of TAMs in MF-aCD169/PD-1 mAbs treated YUMM1.7 tumours. 66
Figure 37. Gating strategy for TILs. 67
Figure 38. Characterization of TILs in MF-aCD169/PD-1 mAbs treated YUMM1.7 tumours. 68

1 Introduction

1.1 Cancer immunology

The interplay between the tumour microenvironment (TME) and cancer cells is critical in understanding tumour development and progression. The TME comprises various cell types, including fibroblasts, extracellular matrix components, vasculature, and importantly, immune cells (Hanahan and Weinberg 2011, Fouad and Aanei 2017).

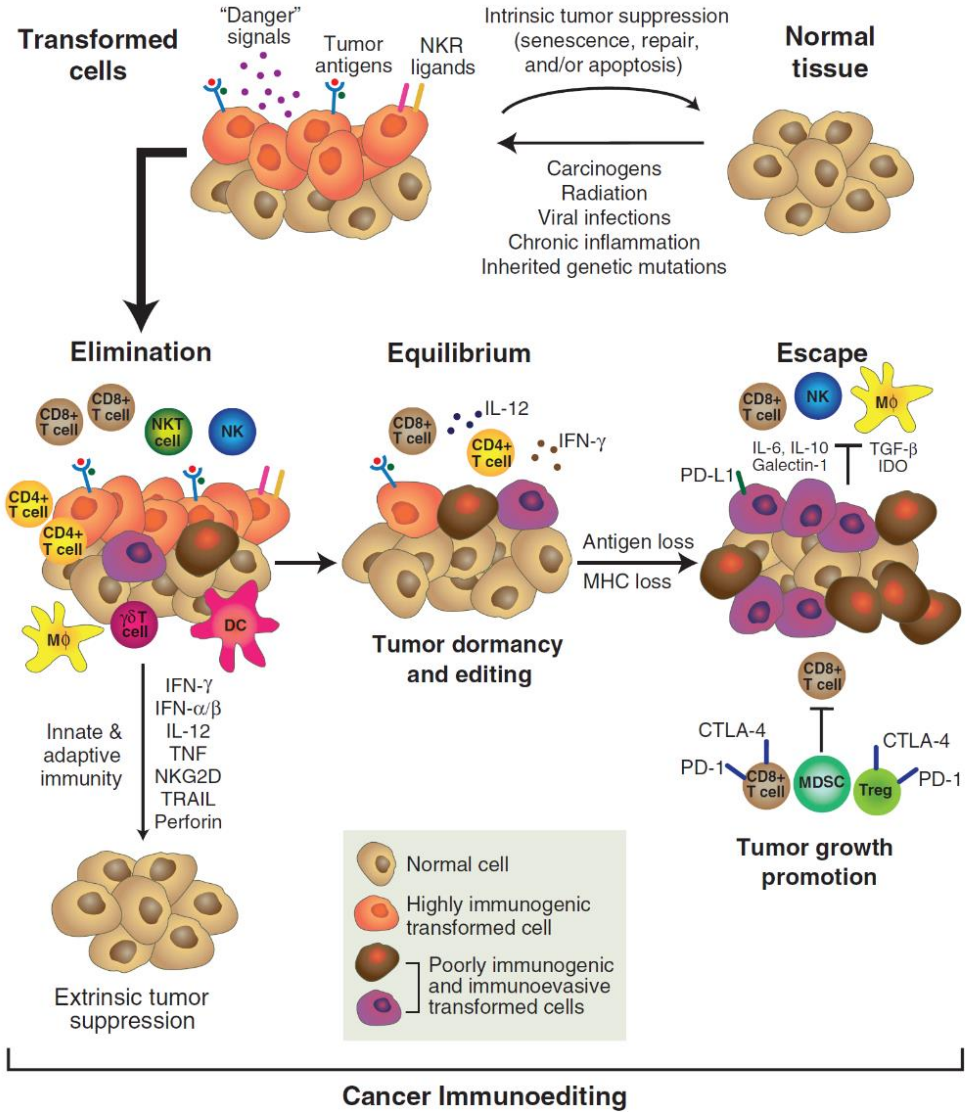

Figure 1. The cancer immunoediting concept.
From Schreiber, Robert D., Lloyd J. Old, and Mark J. Smyth. "Cancer immunoediting: integrating immunity's roles in cancer suppression and promotion." *Science* 331.6024 (2011): 1565-1570. Reprinted with permission from AAAS.

The immune system plays a dual role in cancer: It either suppresses tumour growth by destroying cancer cells and inhibiting their outgrowth, but also promotes tumour progression by selecting for tumour cells that are more fit to survive in an immunocompetent host or by establishing conditions within the TME that facilitate tumour development. The concept of cancer immunoediting, introduced by Robert Schreiber, describes three phases (Schreiber, Old et al. 2011) (**Figure 1**): **(a)** the persistence of aberrant malignant cells capable of triggering immune reprogramming (equipoise phase), **(b)** survival of irregular malignant cells which can activate immune reprogramming (equipoise phase), and **(c)** the establishment of an immunosuppressive TME and development of low-immunogenic tumours (escape phase). This concept highlights the potential for therapeutic interventions targeting the immune system, aiming to either enhance its anti-tumour responses or disrupt the mechanisms enabling tumours to evade immune surveillance.

1.2 Malignant melanoma

Malignant melanoma is a type of skin cancer that arises from melanocytes, the melanin-producing cells localized in the basal layer of the human epidermis (Gray-Schopfer, Wellbrock et al. 2007), the most frequently occurring form being cutaneous melanoma (CM) with 90% of all melanoma cases (Ali, Yousaf et al. 2013). It is characterized by its fast progression, invasiveness, high metastatic potential and resistance to conventional therapies like chemo- and radiotherapy (Testori, Rutkowski et al. 2009, Kalal, Upadhya et al. 2017). With an estimated 325,000 new cases in 2020, CM accounts for 1.7% of global cancer diagnoses according to the Global Cancer Observatory (GCO) (Ferlay, Ervik et al. 2018). The incidence of CM continues to rise globally, becoming one of the most common cancers seen in young adults. Risk factors for malignant melanoma include excessive sun exposure, history of sunburns, family history of melanoma, and certain genetic factors. The most frequent mutations in malignant melanoma occur in the neuroblastoma RAS viral oncogene homolog (N-Ras) and B-rapidly accelerated fibrosarcoma (B-Raf) genes. Approximately 15-20% of patients exhibit N-Ras mutations, while B-Raf mutations are found in 40-60% of cases, with the V600E and V600K mutations being the most prevalent (Platz, Egyhazi et al. 2008). Both of these mutations induce an activation of the mitogen-activated protein kinase (MAPK) pathway, involving the kinases mitogen-activated protein kinase kinase (MEK) and extracellular signal-regulated kinase (ERK) leading to uncontrolled cell growth (Shtivelman, Davies et al. 2014).

1.2.1 Targeted therapy

Targeted therapies revolutionized melanoma treatment, when the first therapies were approved by the FDA in 2011 and the two potent tyrosine kinase inhibitors vemurafenib and dabrafenib are highly effective in the treatment of a B-Raf^{V600}-mutant metastatic melanoma. In a clinical trial, vemurafenib showed an objective response rate (ORR) of 48% vs. 5% for dacarbazine in B-Raf^{V600E} mutation-positive advanced and unresectable melanoma, with a median progression-free survival (PFS) of 5.3 months with vemurafenib vs. 1.6 months with dacarbazine (Flaherty, Puzanov et al. 2010, Ravnan and Matalka 2012). The second B-Raf inhibitor came soon after the first one, with similar promising results (Hauschild, Grob et al. 2012, Ascierto, Minor et al. 2013), however, clinical benefits were usually transient, because of the rapid emergence of drug resistance (Aplin, Kaplan et al. 2011). The main cause of resistance to B-Raf inhibitors is the reactivation of the MAPK pathway, occurring in 80% of B-Raf inhibitor resistant tumours (Czarnecka, Bartnik et al. 2020). Combining B-Raf inhibitors with MEK inhibitors such as trametinib therefore delays the development of resistance (Long, Stroyakovskiy et al. 2015).

1.2.2 Immunotherapy

Given that only about half of patients with metastatic melanoma express the B-Raf mutation, other treatment options are needed. The field of immunotherapy has seen significant progress with the development of immune checkpoint inhibitors (ICIs), which boost T cell activity and have shown great impact on cancer therapy, particularly malignant melanoma (Ugurel, Röhmel et al. 2017). Under physiological conditions, immune checkpoint pathways control the balance between effective immunity and self-tolerance. However, tumours can exploit these pathways by upregulating inhibitory checkpoints leading to T cell arrest and immunosuppression, thereby facilitating tumour growth (Nirschl and Drake 2013). The two most important inhibitory immune checkpoints that have been studied are the cytotoxic T lymphocyte antigen 4 (CTLA-4) and the programmed cell death protein 1 (PD-1). The discovery in the 1990s of the role played by these two molecules in regulating tumour immune responses led to the awarding of the Nobel Prize in Physiology or Medicine in 2018 to Dr. James Allison and Dr. Tasuku Honjo (Rotte, D'Orazi et al. 2018).

Ipilimumab, a monoclonal antibody against CTLA-4 approved in 2011, increased median overall survival of patients with metastatic melanoma to 10.1 months in comparison with gp100 alone in a clinical trial (Hodi, O'day et al. 2010). Additionally, monoclonal antibodies against PD-1 (nivolumab and pembrolizumab) were approved in 2014. Nivolumab achieved a progression-free

survival (PFS) of 6.9 months in melanoma patients, which was increased to 11.4 months in combination with ipilimumab (Postow, Chesney et al. 2015). Pembrolizumab reached a PFS of over 24 months with a response rate of 33% in a clinical trial, whereas ipilimumab alone had a response rate of 12% in the same trial (Robert, Schachter et al. 2015).

In 2015, talimogen laherparevec (T-VEC), a drug consisting of an oncolytic herpes virus that selectively replicates in melanoma cells, was approved for intratumoural injection in nonresectable skin melanoma lesions (Pol, Kroemer et al. 2016). The virus leads to the lysis of melanoma cells and induces the production of granulocyte-macrophage colony-stimulating factor (GM-CSF) by melanoma cells enhancing local and systemic anti-tumour immune responses. The median overall survival was 23.3 months with T-VEC vs. 18.9 months with GM-CSF in a clinical trial (Andtbacka, Chastain et al. 2015).

1.3 Tumour-associated macrophages (TAM)

1.3.1 Origin and role of macrophages in cancer

Macrophages are innate immune cells of the mononuclear phagocyte system, which include macrophages resident in peripheral tissues and circulating monocytes newly recruited at sites of inflammation and tissue damage (e.g., tumours). In solid tumours, macrophages represent the main immune cell population and are present in all stages of tumour progression. Tumour-associated macrophages (TAMs) are generally considered to be mostly tumour-promoting, supporting tumour growth, angiogenesis and metastasis, as well as contributing to an immunosuppressive milieu (Allavena and Mantovani 2012).

Macrophages can be divided into two major populations: monocyte-derived macrophages and tissue resident macrophages. TAMs mostly arise from circulating monocytes that are recruited through inflammatory signals such as CC-chemokine ligand 2 (CCL2) or macrophage colony-stimulating factor (CSF-1) released by the tumour, where they differentiate into TAMs and facilitate tumour progression (Qian, Li et al. 2011, Arwert, Harney et al. 2018). TAMs can also derive from tissue resident macrophages originally present in the tissue that later develops into tumour (Cortez-Retamozo, Etzrodt et al. 2012, Movahedi and Van Ginderachter 2016). They are derived from embryonic precursors and are mostly maintained by local proliferation (Hashimoto, Chow et al. 2013). Notably, TAMs derived from different origins demonstrate distinct phenotypes and functionality. While monocyte-derived TAMs are responsive to polarization, the specific role of tissue resident TAMs is different, as they can retain their tissue specific phenotype (Wynn, Chawla et al. 2013, Zhu, Herndon et al. 2017, Etzerodt, Moulin et al. 2020, Casanova-Acebes, Dalla et al.

2021). Recently, it was shown that tissue-resident TAMs closely associate with tumour cells early in tumour development, contributing to both tumour invasiveness and tissue remodelling (Casanova-Acebes, Dalla et al. 2021).

The M1/M2 macrophage nomenclature that mimics the Th1/Th2 paradigm of T lymphocytes was first described by Mills and colleagues in 2000. It is based on the results from the *in vitro* stimulation of macrophages with IFNγ or lipopolysaccharide (LPS), or both (classically activated or M1), and IL-4 (alternatively activated or M2) (Mills, Kincaid et al. 2000). However, this traditional classification of macrophage polarisation oversimplifies their responses in tissue. Instead, *in vivo*, macrophages exhibit a dynamic responsiveness to a combination of factors present in the microenvironment. This leads to the formation of complex, sometimes mixed phenotypes, wherein both M1 and M2 signatures can be expressed simultaneously (Martinez and Gordon 2014). During initial stages of tumour development, macrophages can directly promote anti-tumour responses by killing tumour cells or indirectly recruit and activate other immune cells. However, during tumour progression, stimuli from the TME drive macrophages towards a pro-tumour phenotype, thereby promoting a tumour-permissive milieu. These pro-tumour macrophages support cancer progression by several mechanisms including immune suppression, growth factor production, promotion of angiogenesis and tissue remodelling.

1.3.2 Functions of TAMs in the tumour microenvironment

Accumulation of TAMs is correlated with poor clinical outcome in many cancer types (Mantovani, Marchesi et al. 2017) and similarly, the expression of macrophage growth factors or their chemoattractant, such as CSF-1 and CCL2, in tumours or the circulation is often associated with poor prognosis (Achkova and Maher 2016, Xu, Wang et al. 2021). TAMs promote tumour progression by secreting growth factors such as epidermal growth factor (EGF), enhancing tumour motility and inducing stem-cell-like properties (Haque, Moriyama et al. 2019). Additionally TAMs secrete pro-angiogenic factors such as vascular endothelial growth factor (VEGF) and chemokines (CXCL8 and CXCL12) (Lin and Pollard 2007). TAMs can alter the extracellular matrix (ECM) by producing proteases, including cathepsins, matrix-remodelling enzymes such as SPARC and lysyl oxidase, and upregulate metalloproteinases (MMP9), facilitating invasion into blood vessels and dissemination to distant sites (Paolillo and Schinelli 2019). Secretion of TGFβ by TAMs induces epithelial-mesenchymal-transition of tumour cells at the invasive front, a mechanism also linked to metastasis (Bonde, Tischler et al. 2012). TAM-mediated immune suppression is caused via several major mechanisms. TAMs express immune checkpoint ligands, such as PD-

L1, PDL-2, B7-1 (CD80) and B7-2 (CD86) (Dong, Strome et al. 2002, Kleffel, Posch et al. 2015, Haque, Moriyama et al. 2019), which directly inhibit T cell functions. They also secret several cytokines (IL-10, TGFβ) that support immunosuppression in the TME by inhibiting CD4+ and CD8+ T cells and by inducing regulatory T cell (Treg) expansion (Chen, Jin et al. 2003), and release chemokines such as CCL2, CCL3, CCL4, CCL5, and CCL20, contributing to the recruitment of Tregs into the TME. Moreover, TAMs deplete metabolites on which T cells are highly dependent by inducing amino acid metabolic starvation in T cells through the production of arginase and indoleamine 2,3-dioxygenase (IDO) (Rodriguez, Quiceno et al. 2004, Munn and Mellor 2007).

1.3.3 TAM targeting for cancer immunotherapy

To overcome the immunosuppressive and pro-tumour functions of TAMs, therapeutic strategies have focused on three major strategies: **(1)** Blocking the recruitment of monocytes and therefore TAMs to the tumour, **(2)** interfering with TAM survival, and **(3)** reprogramming TAMs into anti-tumour macrophages. Trafficking of monocytes from bone marrow to the tumour site requires the CCL2-CCR2 signalling axis (Xu, Wang et al. 2021). CCR2 inhibitors or anti-CCL2 antibodies inhibit TAM recruitment by blocking the mobilisation of bone marrow-derived monocytes (Yang, Zhang et al. 2020). The growth factor CSF-1 is involved in the survival and differentiation of tissue resident macrophages as well as MN-derived macrophages, and treatment with anti-CSF-1R antibodies results in depletion of macrophages/monocytes (Ries, Cannarile et al. 2014). However, these strategies have shown limited effects in some experimental models and clinical trials (Yang and Zhang 2017). Additionally, these drugs, target macrophages in all tissues, not just TAMs, and consequently patients experience significant toxic side effects (Han, Chitu et al. 2022, Pognan, Buono et al. 2022). There is growing evidence that macrophage reprogramming towards a pro-inflammatory activation state or specific depletion of immunosuppressive TAM subsets, rather than pan depletion, may represent a better strategy for TAM-targeting in cancer treatment. Targeting surface molecules on TAMs, such as scavenger receptors CD163, CD206, macrophage receptor with collagenous structure (MARCO) and Stabilin-1 (STAB1), takes the extensive heterogeneity among TAM subsets into account and maintains TAM subsets associated with good prognosis in patients (De Vos van Steenwijk, Ramwadhdoebe et al. 2013, Ino, Yamazaki-Itoh et al. 2013, Etzerodt, Tsalkitzi et al. 2019). Targeting the co-stimulatory molecule CD40 (Kashyap, Schmittnaegel et al. 2020) or CD47 (a phagocytosis inhibitory receptor) (Feng, Jiang et al. 2019)

are among the many strategies used to reprogram TAMs towards a proinflammatory phenotype (Beltraminelli and De Palma 2020).

1.3.4 Specific targeting of CD169+ TAMs for cancer immunotherapy

The diversity of TAM subsets emphasizes the need for precise targeting strategies. One potential subset of interest is distinguished by the endocytotic scavenger receptor CD169, also known as Siglec1 or Sialoadhesin (Sn), a member of the sialic acid binding immunoglobulin-like lectin (siglecs) family (Crocker and Varki 2001). CD169 is expressed on specific subsets of tissue resident macrophages, including expression on bone marrow macrophages, alveolar macrophages, white pulp (metallophilic) macrophages in the spleen, and subcapsular sinus macrophages in the lymph nodes (Crocker, Kelm et al. 1991, Crocker, Mucklow et al. 1994, Nauwynck, Duan et al. 1999, Hartnell, Steel et al. 2001, Gray and Cyster 2012). It is a cell adhesion molecule that mediates interaction with dendritic cells for CD8+ T cell cross-priming (Backer, Schwandt et al. 2010, van Dinther, Veninga et al. 2018). Cassetta et al. demonstrated that tumour cells have the capacity to induce CD169 expression in monocyte-derived TAMs. Importantly, the elevated CD169 expression was found to be a prognostic marker for poor survival in patients, strongly suggesting a relevance of CD169 as target for specific TAM reprogramming strategies (Cassetta, Fragkogianni et al. 2019). Furthermore, CD169 emerges as an early marker in TAM differentiation within the TME. It is detected in both immature and mature TAMs, with a distinct CD169+ and F4/80- cell population identified in the initial stages of subcutaneous murine tumours. This population primarily consists of immature TAMs, believed to progress towards a mature phenotype over time (Etzerodt, Tsalkitzi et al. 2019, Etzerodt, Moulin et al. 2020). Gaining insight into the signalling pathways responsible for polarizing TAMs towards a pro-tumour phenotype is crucial for elucidating the differentiation mechanisms of TAMs.

1.4 Glucocorticoids

1.4.1 Glucocorticoid biosynthesis

Glucocorticoids (GCs) are steroid hormones that are crucial to various physiological processes, including metabolism, development and inflammation. Cortisol, the main GC in humans, is synthesised by the zona fasciculata of the adrenal cortex in the adrenal gland from cholesterol (**Figure 2**). The first step of cortisol biosynthesis is the transport of cholesterol into mitochondria by the steroidogenic acute regulatory protein (StAR), followed by the side chain cleavage to pregnenolone, a precursor of all steroids, by Cyp11A1 (cholesterol side chain cleavage enzyme), bound

to the inner mitochondrial membrane. Pregnenolone can either serve as substrate for 3β-hydroxysteroid dehydrogenase (3-βHSD), which converts it to progesterone or be converted to 17α-hydroxypregnenolone by Cyp17A1, followed by the conversion to 17α-hydroxyprogesterone. 3-βHSD can be found both in the mitochondria and the endoplasmic reticulum (ER) and pregnenolone appears to exit the mitochondria unaided. 17α-hydroxyprogesterone is converted to cortisol by Cyp21A2 and Cyp11B1 again taking place in the mitochondria. How cortisol is released from mitochondria is not well defined. Presumably it is driven by the concentration gradient from the mitochondrial matrix, the cytoplasm, and systemic blood circulation, facilitated by the hydrophobic nature of steroid hormones allowing them to diffuse through lipid membranes (Miller 2013, Picard, McEwen et al. 2018).

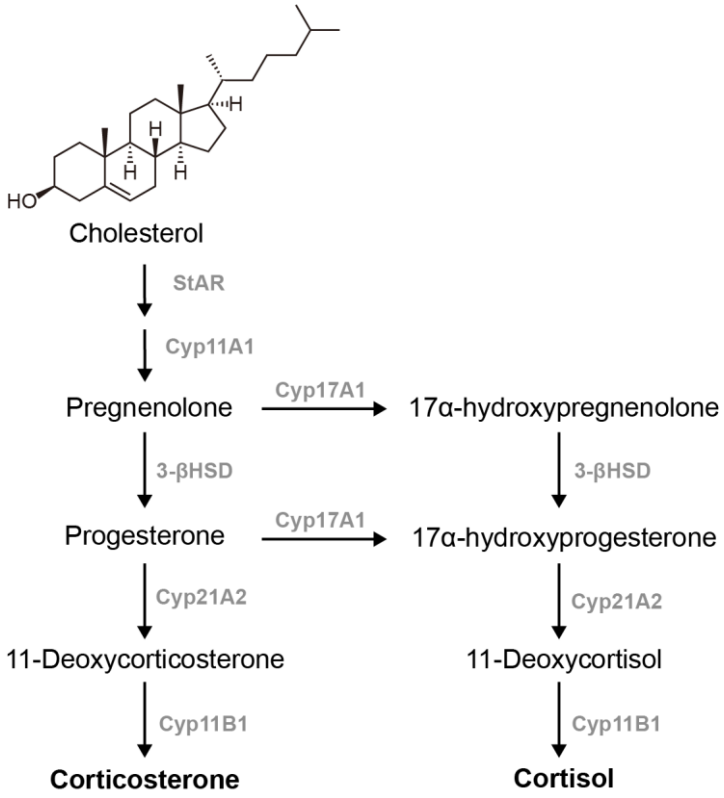

Figure 2. Glucocorticoid biosynthesis.

1.4.2 Regulation of glucocorticoid production and activity

The secretion of GCs is controlled by the hypothalamic-pituitary-adrenal (HPA) axis (**Figure 3**): Inflammation and other stressors trigger the hypothalamus to release corticotropin releasing hormone (CRH), which acts on the anterior pituitary to stimulate the secretion of adrenocorticotropic hormone (ACTH). ACTH then acts on the adrenal cortex to stimulate the production and secretion

of GCs. In a classic negative feedback loop, GCs suppress expression of the precursor proopiomelanocortin (POMC), as well as production and release of CRH in the hypothalamus and ACTH in the anterior pituitary, thereby maintaining homeostasis in GC levels. The synthesis and release of GCs is under dynamic circadian and ultradian regulation with peak levels linked to the start of the activity phase. Circulating cortisol, the main GC in humans, reaches its peak in the early morning, while in rodents the main GC is corticosterone that peaks in late afternoon, around the transition point of light/dark cycle (Veniant, Hale et al. 2009, Scherholz, Schlesinger et al. 2019).

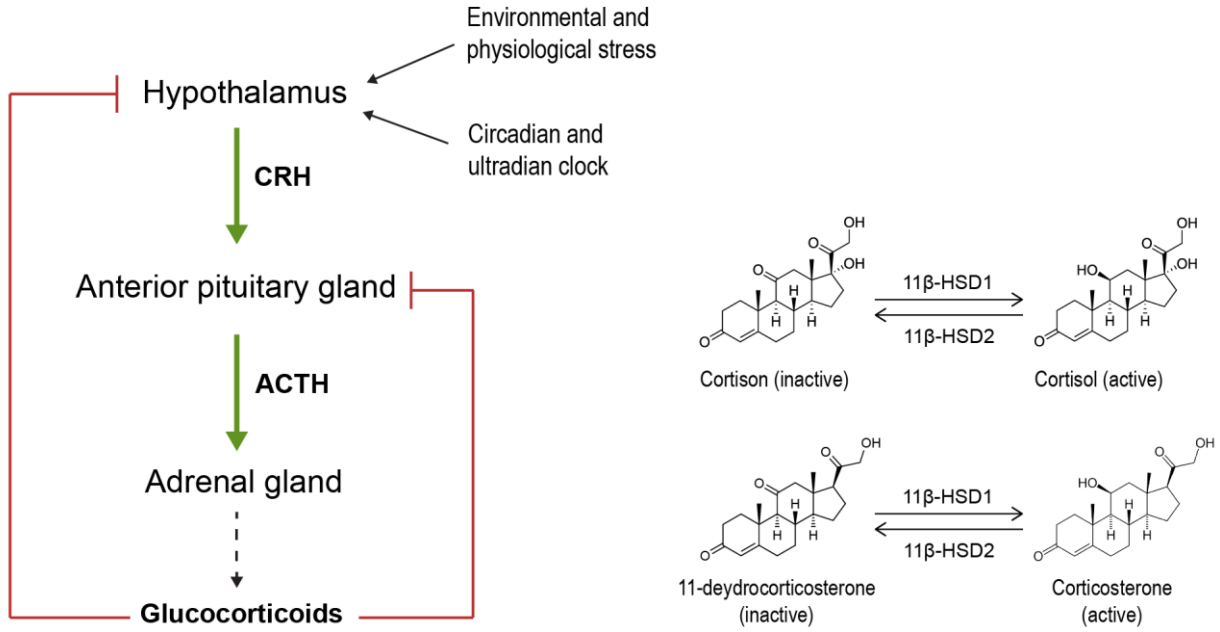

Figure 3. Schematic representation of the regulation of glucocorticoid levels by the hypothalamic-pituitary-adrenal axis and by 11β-hydroxysteroid dehydrogenase (11β-HSD) in peripheral tissue.

While adrenal steroidogenesis drives systemic changes in GC concentrations, local GC activity in tissues is regulated by the intracellular enzyme 11β-hydroxysteroid dehydrogenase (11β-HSD) and extracellular corticosteroid binding globulin (CBG, transcortin) in serum. CBG is member of the serine protease inhibitor (SERPIN) family that transports GCs and progesterone in the blood circulation, thereby modulating the tissue availability of these hormones (Gardill, Vogl et al. 2012). 11β-HSD1 is a bidirectional enzyme that acts predominantly as an oxidoreductase converting inactive cortison to active cortisol in humans or 11-dehydrocorticosterone (11-DHC) to corticosterone in rodents. Its isoenzyme, 11β-HSD2, is a dehydrogenase and catalyses the opposite reaction. 11β-HSD1 is primarily expressed in liver, adipose and brain, while the expression of

11β-HSD2 is largely restricted to the classical aldosterone (mineralocorticoid)-target tissues, primarily the kidney. The mineralocorticoid receptor (MR) has two ligands with similar affinity, aldosterone and cortisol. In the normal state, plasma GC levels are more than 100 times higher than aldosterone levels, and MRs are occupied by GCs. The action of aldosterone at the MR is conveyed by the activity of 11β-HSD2 that metabolises cortisol to inactive cortisone, which is unable to bind the MR, and thus, aldosterone, which is not a substrate for 11β-HSD, activates the MR (White, Mune et al. 1997, Wyrwoll, Holmes et al. 2011).

Finally, although GCs are mainly synthesized in the adrenal gland, there is also evidence of extra-adrenal steroidogenesis, including production or recycling of GCs in immune cells, skin, brain, lymphoid tissue, intestine, and tumour cells (Taves, Gomez-Sanchez et al. 2011, Slominski, Tuckey et al. 2020, Anderson and Acharya 2022, Gomez-Sanchez and Gomez-Sanchez 2022).

1.4.3 Glucocorticoid receptor signalling

Because of the powerful anti-inflammatory and immunosuppressive actions of GCs, synthetic GCs are one of the most widely prescribed drugs in the world today and are used for the treatment of asthma, Crohn's disease, and rheumatoid arthritis, among other chronic conditions. The physiological and pharmacological actions of GCs are mediated by the ubiquitously expressed glucocorticoid receptor (GR, encoded by *Nr3c1*), a member of the nuclear receptor superfamily of ligand-dependent transcription factors.

The GR protein is composed of three major domains, an N-terminal transactivation domain (NTD), a central DNA-binding domain (DBD), and a C-terminal ligand binding domain (LBD). The LBD contains a hydrophobic pocket for binding GCs and is separated from the DBD by a flexible hinge region. The DBD contains two zinc-finger motifs that recognize and bind target DNA sequences called GC-responsive elements (GREs). The NTD houses a transcriptional activation function that interacts with co-regulators and transcription machinery and is the primary site for post-translational modifications. Different GR isoforms are generated by alternative splicing, with GRα and GRβ being the most important. The isoform associated with transcriptional regulation by GCs is GRα, whereas GRβ is a splice variant that cannot bind GCs but is believed to exert a negative regulatory influence on GRα. However, some studies have reported instances of direct transcriptional activity.

In the absence of GCs, the GR resides in the cytoplasm in a multiprotein complex that contains chaperone proteins (hsp90, hsp70, and p23) and immunophilins (FKBP51 and FKBP52). These proteins maintain the receptor in a conformation that is transcriptionally inactive but favours high

affinity ligand binding. Upon binding GCs, the GR undergoes a conformational change resulting in the dissociation of the associated proteins followed by translocation to the nucleus. Inside the nucleus, the GR binds directly to GREs located in the promoter region of target genes and regulates gene expression. Binding of the GR to positive GREs leads to increased transcription of anti-inflammatory and immunosuppressive proteins, e.g., IL-10, annexin A1 and inhibitor of NFκB (IκB) (transactivation), and binding to negative GREs inhibits the transcription of genes encoding proteins such as AP-1 or NFκB (transrepression). This represses the transcription of pro-inflammatory proteins, e.g., IL-1, IL-2, IL-6, COX-2, TNF and prostaglandins. Additionally, the GR physically interacts with, or "tethers", other transcription factors without contacting DNA, inhibiting their effect on gene expression. Genomic effects of GR signalling are typically evident within hours or days. However, GCs can also induce immediate effects through non-genomic mechanisms, involving non-specific interactions with the cell membrane, or specific interactions with cytosolic GRs or membrane-bound GRs (Stahn and Buttgereit 2008, Kadmiel and Cidlowski 2013, Panettieri, Schaafsma et al. 2019).

GCs are potent regulators of inflammation and exert their anti-inflammatory role by acting on nearly all cell types of the immune system. Among other processes, GCs repress the expression of pro-inflammatory cytokines by immune cells, or the expression of adhesion molecules, which prevents rolling, adhesion and extravasation of neutrophils to the site of inflammation. Furthermore, GCs limit the maturation and activation of dendritic cells (DCs) that are central for T cell responses. Chronic exposure to GCs induces a switch in the resident macrophages gene expression profile from pro-inflammatory to anti-inflammatory, and increases macrophages phagocytic activity. The effect of GCs on T cells is specific to the subtype of T cells. GCs induce apoptosis in Th1 T cells, while exerting pro-survival effects in regulatory T cells (Baschant and Tuckermann 2010, Zen, Canova et al. 2011, Cain and Cidlowski 2017).

1.5 Nanocarriers for drug delivery

1.5.1 Nanocarrier systems

Nanocarriers are drug delivery systems of submicron size and high versatility. They include liposomes, polymeric, lipid and inorganic nanoparticles, nanotubes, nanocomplexes, niosomes and many other systems. Nanocarriers function as vehicles that determine the pharmacokinetics of transport and distribution instead of the active drug. Advantages that nanocarriers offer over free drugs include protection against the degradation of active drugs, inhibiting premature interaction of the drug with the biological environment, enhancing cellular uptake, controlling pharmacokinetic

and drug tissue distribution profile, and improving accumulation of the drug in target tissue, e.g., the tumour. Currently, the most advanced drug delivery method are the lipid-based nanocarrier systems, which, due to the nature of the materials used, offer easy large-scale manufacturing, biocompatibility and biodegradability, low toxicity, the possibility of controlled and modified drug release, improvement of drug solubility, and the potential to incorporate both hydrophilic and lipophilic drugs (Priya, Desai et al. 2022). The two types of lipid-based nanocarriers are vesicular, including liposomes, and nonvesicular, including solid lipid nanoparticles (LNPs), nanostructured lipid carriers, or nanoemulsions (Verma and Utreja 2019). Liposomes are composed of phospholipids that form one or more lipid bilayers (unilamellar or oligo-/multilamellar liposomes) enclosing an aqueous core, and can solubilize both hydrophilic and lipophilic drugs. Disadvantages of liposomes include the lack of affordable preparation methods and the relatively low drug loading capacity and stability. Smaller liposomes have an unfavourable ratio of intraliposomal volume to the amount of lipid applied and tend to fuse due to their high curvature. Larger liposomes are rapidly decomposed in the human body before the therapeutic effect can be achieved, showing significantly reduced efficacy (Mayer, Tai et al. 1989, Swenson, Perkins et al. 2001). LNPs consist of a lipid core matrix that can dissolve lipophilic drugs, and do not have a bilayer system as in liposomes. LNPs are physically stable frameworks with longer shelf live compared to liposome formulations, and the release profile of the drug is improved by the low drug mobility in solid lipids, making LNPs the favoured drug delivery system (Mehnert and Mäder 2012).

1.5.2 Passive targeting of nanocarriers

Nanocarriers were initially developed to reduce toxicity in patients by targeting chemotherapeutic drugs more efficiently to tumour tissue. In healthy tissue, blood vessels are surrounded by a dense endothelium allowing only small molecules to exit the blood stream, while larger structures are retained. Due to their rapid growth, tumours exhibit abnormal angiogenesis and neovasculature with wider fenestrations (Hobbs, Monsky et al. 1998). After intravenous application, nanocarriers preferentially exit the blood stream through the leaky tumour vasculature, and are subsequently retained in the tumour tissue due to reduced lymphatic drainage. This phenomenon leads to accumulation of nanocarriers in tumour tissue and is known as the “enhanced permeability and retention” (EPR) effect. It was first introduced by Matsumura and Maeda in 1986 (Matsumura and Maeda 1986). The EPR effect in tumours is limited by the high pressure of the interstitial fluid, the dense extracellular matrix, and the occluded or embolized blood vessels of the tumour. Additionally, nanocarriers can accumulate in tissues of the reticuloendothelial system (RES), which is

primarily localized in the liver, spleen and bone marrow. With respect to nanocarrier clearance, the liver and spleen are the most active organs. Nanocarriers in the blood circulation are rapidly opsonized by serum proteins and phagocytosed by cells of the mononuclear phagocyte system (MPS), especially macrophages. Therefore, long circulating nanocarriers were generated by polymer surface coating that sterically shields the nanocarrieres, so called “stealth” nanocarriers. This reduces opsonisation and premature clearance, increases blood circulation time and potentially enhances accumulation in the tumour (Salmaso and Caliceti 2013). Surface modifications with polyethylene glycol (PEG) are the most widely used (Scherphof, Morselt et al. 1994), as seen in examples such as Caelyx®, a formulation of PEGylated liposomal doxorubicin, approved in 1996. Compared to free doxorubicin, Caelyx® exhibits significantly prolonged half-life in the blood, accompanied by less severe side effects such as bone marrow depressant and cardiotoxicity that are often dose limiting (Gabizon, Shmeeda et al. 2003).

1.5.3 Active targeting of nanocarriers

Passive targeting has demonstrated relevant progress in cancer therapy. However, with tumour specificity of 20–30% in delivery increase compared to normal organs, effectiveness is often insufficient. EPR-based tumour targeting is dependent on the intrinsic tumour biology, specifically on the extent of angiogenesis and lymph angiogenesis, perivascular tumour growth and the intratumour pressure. Additionally, the size of the nanocarrier is important for the permeation and retention in the tumour and limited by the fenestrations in tumour vessels (200-800 nm), renal extraction (< 6 nm) and clearance through the RES (> 500 nm) (Attia, Anton et al. 2019). Moreover, PEGylation of nanocarriers leads to reduced cellular interaction and endocytosis, posing a significant disadvantage, especially for drugs that are poorly taken up by the target cell after release or are rapidly degraded extracellularly (Ernsting, Murakami et al. 2013). Active targeting can increase the quantity of drug delivered to the target cells compared to free drug, increasing drug efficiency after accumulation in the tumour tissue. This is achieved through conjugation of ligands binding to proteins overexpressed in the tumour on the surface of the nanocarrier, resulting in increased cellular uptake by receptor-mediated endocytosis and intracellular release of the drug. This mechanism relies on the interaction between conjugated ligands on the nanocarrier surface receptors and antigens on the surface of the target cells. Depending on the target cell, small molecules, oligonucleotides and peptides, including monoclonal antibodies or antibody fragments, can be used as ligands for active targeting (Zhou, Drummond et al. 2007, Chen, Ke et al. 2013, Goodall, Jones et al. 2015, Wang, McGuirk et al. 2020).

2 Aim of the study

Primary and secondary resistance is a major challenge in cancer immunotherapy. Therefore, gaining a better understanding of the mechanisms underlying immunotherapy resistance is critical to improve therapeutic outcomes. TAMs represent the most abundant immune cell type within the tumour. Despite their inherent potential for immune stimulation, TAMs predominantly exert tumour-promoting functions through immune suppression. This occurs due to signals from the TME that drive TAMs towards a pro-tumour phenotype, thus promoting a tumour-permissive milieu. Recently, tumour-derived GCs were identified as a mechanism for evading the immune response in tumours, hindering both anti-tumour T cell responses and the effectiveness of checkpoint immunotherapy. However, the impact of tumour-derived GCs on the function of TAMs remains largely unknown.

Therefore, the objective of this thesis was to investigate the role of GC-responsive TAMs in promoting immunosuppression in a melanoma model that is resistant to checkpoint immunotherapy. Additionally, the goal was to develop functionalized lipid nanoparticles for targeted drug delivery, aiming to reprogram immunosuppressive TAMs towards an activated, anti-tumour phenotype through GR blockade. This approach is expected to enhance tumour immunity and overcome resistance to checkpoint immunotherapy.

3 Materials

3.1 Technical equipment

Name	Supplier
Cell culture incubator Hera cell 150	Heraeus
Centrifuge 5810 R	Eppendorf
Centrifuge biofuge pico	Heraeus
Chromolith® RP-18 endcapped	Merck
Countess II	Thermo Fisher Scientific
Cytek Northern Light Spectral Flow Cytometer	Cytek Biosciences
Dionex UltiMate 3000 HPLC system	Thermo Fisher Scientific
DynaPro NanoStar	Wyatt Technology Europe GmbH
FACS Lyric Flow Cytometer	BD Biosciences
IVIS Lumina LT Series III	Caliper Life Science
Laminar flow hood Hera safe	Heraeus
FACS LSRFortessa	BD Biosciences
Magnetic bead column holder MACS multistand	Miltenyi Biotec
Mr. Frosty freezing container	Thermo Fisher Scientific
NanoAssemblr	Precision NanoSystems
Precellys	Bertin Technologies
Tecan infinite M200	Tecan
Vortexer VF2	IKA
ZetaView	Particle Metrix GmbH

3.2 Software

Name	Supplier
Chromeleon software, version 7.1.3.2425	Thermo Fisher Scientific
FACS Diva, version 9	BD Biosciences
FACSuite	BD Biosciences
FlowJo, version 10.8.1	BD Biosciences
GraphPad Prism, version 9.5.0	GraphPad
Living Image Sofware, version 4.8.0	PerkinElmer
Microsoft Office 365, 2016	Microsoft Corporation
MxPro qPCR	Stratagene
SpectroFlo, version 3.0	Cytek Bioscience
Tecan i-control, version 2.0.10.0	Tecan
ZetaView, version 8.05.16 SP2	Particle Metrix GmbH

3.3 Consumables

Name	Supplier	Cat. No.
Cell counting chamber slides	Thermo Fisher Scientific	C10283
Cell strainer, 70 µm	NeoLab/Migge	352350
MACS columns LS	Miltenyi Biotec	130-042-401
96-well, U-bottom	Greiner	650180
96-well, F-bottom, black	Greiner	655090
24-well, F-bottom	Sarstedt	833,922,500
6-well, F-bottom	Stemcell	100-0096
qPCR plate seals	Thermo Fisher Scientific	AB1170
96-well qPCR plates	Thermo Fisher Scientific	AB1400150
Cell culture dish, 10 cm	Greiner	664160
Cell culture flask, T175	Greiner	660160
Tubes, 15 ml	Falcon	352096
Tubes, 50 ml	Falcon	352070
Cryo tubes, 2 ml	Greiner	122263
Dialysis tubing, 12-14 kD MWCO	Repligen	132700
Needle, 25G	BD Biosciences	3086982
Needle, 30G ½	BD Biosciences	304000
Syringe, 1 ml	B. Braun	9161502
Syringe, 5 ml	B. Braun	C541.1
Tubes, 1.5 ml	Eppendorf	30120086
Tubes, 2 ml	Eppendorf	30120094
Serological pipette, 10 ml	Sarstedt	861,254,001
Serological pipette, 25 ml	Sarstedt	861,685,001
Serological pipette, 5 ml	Sarstedt	861,253,001
ELISA plates, uncoated	Biolegend	423501
Plate sealers	Biolegend	423601
Pipette filter tips, 10 µl	Biozym	VT0200
Pipette filter tips, 100 µl	Biozym	VT0230
Pipette filter tips, 200 µl	Biozym	VT0240
Pipette filter tips, 1250 µl	Biozym	VT0270
Pipette tips, 10 µl	Biozym	VT0104
Pipette tips, 200 µl	Biozym	VT0144
Pipette tips, 1250 µl	Biozym	VT0174
Precellys ceramic kit, 2 ml	VWR	431-0170
Plate Sealers	Biolegend	423601

3.4 Chemicals, solvents and reagents

Name	Supplier	Cat. No.
11-Dehydrocorticosterone (11-DHC)	MedChemExpress	MCE-HY-113447
2-Propanol	Sigma-Aldrich	33539-M
7-AAD	BD Biosciences	559925
Acetonitrile	Sigma-Aldrich	34998
Agarose	Sigma-Aldrich	A9539

Bovine Serum Albumin Fraction V (BSA)	Sigma-Aldrich	10735078001
Brilliant stain buffer	BD Biosciences	566349
Carboxyfluorescein succinimidyl ester (CFSE)	Biolegend	423801
Chloroform	Sigma	288306
Collagenase II	Sigma-Aldrich	C6885
Compensation beads	Thermo Fisher Scientific	01-1111-42
Dimethyl sulfoxide (DMSO)	Sigma-Aldrich	D2438
D-Luciferin, potassium salt	Hölzel	AGSC-L-1207
DMEM F-12	Sigma-Aldrich	D8437
DMEM GlutaMAX	Gibco	61965059
DNAse I	Sigma-Aldrich	11284932001
DNase/RNase-free distilled water	Thermo Fisher Scientific	10977035
dNTP Mix	Thermo Fisher Scientific	R0193
DSPE-PEG5000-DBCO	Avanti Polar Lipids	880226P
Dulbecco's phosphate-buffered saline (DPBS)	Gibco	14190094
Enzyme free cell dissociation solution	Sigma-Aldrich	S-014-B
Ethanol	Carl Roth	5054.4
Ethylene diamine Tetraacetic acid (EDTA)	Thermo Fisher Scientific	15575-38
FcR blocking reagent, mouse	Miltenyi Biotech	130-092-575
Fetal bovine serum (FBS)	Gibco	10270106
innuMIX qPCR DSGreen Standard	IST Innuscreen	845-AS-1320200
Isoflurane	WDT	21311
Loading Dye, 6x	Thermo Fisher Scientific	R0611
Lympholyte-M	Cedarlane Labs	CL5035
Lysing buffer	BD Biosciences	555899
Maxima Reverse Transcriptase	Thermo Fisher Scientific	EP0743
MEM non-essential amino acids (NEAA)	Sigma-Aldrich	M7145
mPEG2000-DSPE	Lipoid	NA
N-(2-Hydroxyethyl)piperazine-N′-(2-ethanesulfonic acid) (HEPES)	Gibco	15630056
Nancy 520	Sigma-Aldrich	1494
Oligo(dT)18 primer	Thermo Fisher Scientific	SO132
Penicillin-Streptomycin (P/S)	Thermo Fisher Scientific	15140122
POPC	Lipoid	NA
Proteinase K from Tritrachium	Sigma-Aldrich	P6556
RNase inhibitor	Thermo Fisher Scientific	EO0382
RNaseZAP	Sigma-Aldrich	R2020-6X250ML
RPMI-1640 GlutaMAX	Gibco	61870010
Sodium azide	Carl Roth	K305.1
Sodium pyruvate	Sigma-Aldrich	P5280
Stop Solution for TMB Substrate	Biolegend	423001
TAE buffer	Carl Roth	CL86.2

Taq DNA-Polymerase	Thermo Fisher Scientific	EP0406
Trifluoroacetic acid	Sigma-Aldrich	302031
Triolein	Sigma-Aldrich	92860
Trypan blue solution	Thermo Fisher Scientific	T10282
TrypLE	Gibco	A1217701
Zombie Aqua fixable viability dye	Biolegend	BLD-423102
Zombie NIR fixable viability dye	Biolegend	423105
β-Mercaptoethanol	Sigma-Aldrich	M3148

3.5 Antibodies

3.5.1 Unconjugated antibodies

Specifity	**Clone**	**Supplier**	**Cat. No.**
CD28	37.51	BD Biosciences	553294
CD3	17A2	Biolegend	100202
CD169	Ser4		

3.5.2 Conjugated antibodies

Cytek Northern Light Spectral Flow Cytometer

Antibody	**Clone**	**Fluorescent Tag**	**Supplier**	**Cat. No.**
MHC-II	M5/114.15.2	BV480	BD Bioscience	566088
Siglec-F	E50-2440	BV510	BD Bioscience	740158
PD-1	J43	BV605	BD Bioscience	563059
CD25	PC61.5	BV480	BD Bioscience	566202
CD27	LG.3A10	BV510	BD Bioscience	563605
CD45	30-F11	APC-Fire 810	Biolegend	103174
F4/80	BM8	BV785	Biolegend	123141
CD163	S15049I	KIRAVIA Blue 520	Biolegend	155318
PD-L1	10F.9G2	PE-Dazzle594	Biolegend	124324
PD-L1 Isotype	Rat IgG2b	PE-Dazzle594	Biolegend	400660
CD86	GL-1	APC	Biolegend	105012
Ly6C	HK1.4	APC-Fire 750	Biolegend	128046
CD206	C068C2	PE-Fire 700	Biolegend	141741
CD8	53-6.7	Spark Blue 550	Biolegend	100780
FoxP3	MF-14	Alexa Fluor 700	Biolegend	126422
ICOS	15F9	PE-Fire 700	Biolegend	107716
TIM-3	B8.2C12	APC	Biolegend	134008
CD11b	M1.70	APC-R700	BD Bioscience	564985
Ly6G	1A8	PerCP-Cy5.5	BD Bioscience	560602
CD169	SER-4	PE	eBioscience	12-5755-82
CD4	RM4-5	APC-Cy7	Biolegend	100526
PD-1	J43	BV605	BD Bioscience	563059

FACS Lyric Flow Cytometer

Antibody	Clone	Fluorescent Tag	Supplier	Cat. No.
CD45	30-F11	FITC	Biolegend	103108
CD11b	M1/70	APC-R700	BD	564985
F4/80	BM8	APC-Cy7	Biolegend	123117
CD169	SER-4	PE	eBioscience	12-5755-82
CD163	S150491	BV421	Biolegend	155309
MHC-II	M5/114.15.2	AF647	BD	562367
CD86	GL1	BV605	BD	563055
Ly6G	PerCP-Cy5.5	PerCP-Cy5.5	BD Bioscience	560602
Ly6C	HK1.4	BV605	Biolegend	128035
CD4	RM4-5	APC-Cy7	Biolegend	100526
CD8	53-6.7	BV421	Biolegend	100753
PD-1	J43	PE	Invitrogen	PA5-35011
TIM-3	5D12	BV605	BD	747624
LAG-3	C9B7W	APC	BD	562346

FACS LSRFortessa

Antibody	Clone	Fluorescent Tag	Supplier	Cat. No.
MHCII	M5/114.15.2	AF647	BD Biosciences	562367
CD11b	M1/70	BB700	BD Biosciences	566417
F4/80	6F12	BV650	BD Biosciences	744338
CD45.2	104	BV786	BD Biosciences	563686
CD163	S15049I	BV421	Biolegend	155309
CD169	SER-4	PE	eBioscience	12-5755-82
Ly6C	AL-21	FITC	BD Biosciences	561085
Siglec F	E50-2440	PE-CF594	BD Biosciences	562757
CD3	145-2C11	PE-CF594	BD Biosciences	562286
CD19	1D3	PE-CF594	BD Biosciences	562329
NK1.1	PK136	PE-CF594	BD Biosciences	562864
Ly6G	1A8	PE-CF594	BD Biosciences	562700
CD11c	HL3	PE-Cy7	BD Biosciences	558079

FACS analysis was performed using the FACS Lyrik Flow Cytometer (Figure 10, Figure 16, Figure 17, Figure 18), FACS LSFortessa (Figure 8) or Cytek Spectral Flow Cytometer (all other figures).

3.5.3 Therapeutic antibodies

Specifity	Clone	Supplier	Cat. No.	Concentration
PD-1	RMP1-14	BioXcell	BE0146	12.5 mg/kg
Rat IgG2a Isotype	2A3	BioXcell	BE0089	12.5 mg/kg

3.6 Growth factors, stimulants and drugs

3.6.1 Growth factors

Name	Supplier	Cat. No.	Concentration
M-CSF	PeproTech	315-02	30 ng/ml

3.6.2 Stimulants

Name	Supplier	Cat. No.	Concentration
Lipopolysaccharide (E.coli)	Sigma-Aldrich	L5418-2ml	100 ng/ml
IFNγ	PeproTech	315-05	10 ng/ml
IL4	PeproTech	214-14	10 ng/ml

3.6.3 Drugs

Name	Supplier	Cat. No.	Concentration
Dexamethasone	Sigma-Aldrich	D2915	100 nM
Mifepristone, RU-486	Sigma-Aldrich	M8046	100 nM

3.7 Commercial kits

Name	Supplier	Cat. No.
CD8a+ T cell isolation Kit, mouse	Miltenyi Biotec	130-104-075
innuprep RNA Mini Kit 2.0	IST Innuscreen	845-KS-2040250
Corticosterone ELISA Kit	Biozol	AAY-K014-H1
IL-12/IL-23 (p40) ELISA Kit	Biolegend	431604
FoxP3/Transcription Factor Staining Buffer Set	eBioscience	00-5523-00

3.8 Buffers and media

Collagenase II digestion mix
DMEM GlutaMAX
0.1% BSA
1 mg/ml Collagenase II
10 µg/ml DNAse I

FACS buffer
PBS
2% BSA
1 mM EDTA
0.1% NaN3
50% brilliant stain buffer

MACS buffer
PBS
0.5% BSA
2 mM EDTA

BMDM growth medium	DMEM GlutaMAX 10% FBS 1% P/S
B16-F10*luc2* growth medium	RPMI-1640 GlutaMAX 10% FBS 1% P/S
T cell growth medium	RPMI-1640 GlutaMAX 10% FBS 1% P/S 10 mM HEPES 50 µM β-mercaptoethanol 1 mM MEM NEAA 1 mM sodium pyruvate
YUMM1.7 growth medium	DMEM F-12 10% FBS 1% P/S 1% MEM NEAA 0,05% sodium pyruvate

3.9 Primers

3.9.1 PCR Primer

Gene	Forward Sequence 5' to 3'	Reverse Sequence 5' to 3'
Cre	AAGAACCTGATGGACATGTTCAGG	CGGTGCTAACCAGCGTTTTCGTTC
GR flox	GGCATGCACAATTACGGCCTTCT	CCTTCTCATTCCATGTCAGCATGT
iCre tg	AAGCTGAACAACAGGAAATGGTTC	GGAGATGTCCTTCACTCTGATTCT
iCre wt	TGACCACAGCTGCATCTTCA	CCCCACTTCCTCCAACCTTC

3.9.2 qPCR Primer

Gene	Forward Sequence 5' to 3'	Reverse Sequence 5' to 3'
bAktin	ACCCGCGAGCACAGCTTC	CTTTGCACATGCCGGAGC
CD163	GCCATAACTGCAGGCACAAA	GTTGGTCAGCCTCAGAGACA
Ciita	TGCGTGTGATGGATGTCCAG	CCAAAGGGGATAGTGGGTGTC
Cyp11A1	CTGGCGACAATGGTTGGCTA	GCCCAGCTTCTCCCTGTAAAT
Erp44	CTGGTGTCGTTTCAGCCAGAT	TCCTGTACCTCTGGGCTATATCA
HSD11B1	TGGCCTCATAGACACAGAAACA	ACACCTCGCTTTTGCGTAGA
Mrc1	TTCAGCTATTGGACGCGAGG	GAATCTGACACCCAGCGGAA
Nr3c1	GGCAAAGGCGATACCAGGATT	AGGAGCAAAGCATAGCAGGT

3.10 Mice and cell lines

3.10.1 Mice

Mouse strain	Genetic Background	Supplier
mT/mG	B6.129(Cg)-Gt(ROSA)26Sortm4(ACTB-tdTomato,-EGFP)Luo/J	MedMa
LysM-cre	B6N.129P2(B6)-Lyz2tm1(cre)Ifo/J	MedMa
CD163-cre	B6N-Cd163tm1(cre)Tla	
GR flox	B6.129S6-Nr3c1tm2.1Ljm/J	MedMa
C57BL/6J	1001: C57BL/6JRj	Janvier

3.10.2 Cell lines

B16-F10*luc2*
YUMM1.7

4 Methods

4.1 Cell culture methods

4.1.1 Cell lines

B16-F10/*luc2* and YUMM1.7 cells were cultured in T175 flasks at 37°C and 5% CO_2 in RPMI-1640 GlutaMAX supplemented with 10% FBS and 1% Penicillin/Streptomycin (P/S) or DMEM/F-12 supplemented with 1% non-essential amino acids (NEAA), 0.05% sodium pyruvate, 10% FBS and 1% P/S, respectively. For sub-cultivation, adherent cells were washed with PBS followed by treatment with trypsin/EDTA for 5 min at 37°C or at RT. Complete growth medium was added to stop the reaction. Cell suspensions were centrifuged at 300 x g for 5 min to pellet the cells and resuspended in the respective complete growth medium at a ratio of 1:3, 1:5, 1:10 or at a defined cell number for further cultivation. For *in vivo* experiments, 2.5 x 10^6 cells/T175 were seeded 24 h prior to the experiment. For harvesting, cells were washed with PBS and detached by incubation with enzyme-free cell dissociation buffer for 15 min at 37°C or RT. The reaction was stopped by adding PBS and cell suspensions were centrifuged at 300 x g for 5 min to pellet the cells. Cell concentration was adjusted to 2.5 x 10^6 cells/ml with PBS and cells were stored at 4°C until usage or 2 h maximum. Cell lines were regularly tested for mycoplasma contamination, and cell growth as well as cell morphology were controlled under an inverted microscope.

4.1.2 Cell counting

For cell number determination, 10 µl of cell suspension were diluted with 10 µl trypan blue. After transferring 10 µl of the solution into a chamber slide, trypan blue negative cells were counted on Countess II automated cell counter.

4.1.3 Cell line freezing and thawing

For cryopreservation of cell lines, 80–90% confluent cells were harvested and resuspended at 2.5 x 10^6 cells/ml in respective complete growth medium containing 10% DMSO. 1 ml of cell suspension was immediately distributed to freezing tubes and frozen at –80°C in a Mr. Frosty™ freezing container filled with isopropanol. After 24 h, cryovials were transferred to the liquid nitrogen tank for long term storage. Frozen cells were thawed quickly at 37°C, washed with complete growth medium and transferred to a T175 flask containing 20 ml of respective complete growth medium for culture at 37°C and 5% CO_2.

4.1.4 Preparation of tumour-conditioned medium

YUMM1.7 cells were thawed and cultivated in complete growth medium until 90% confluent, after which they were split 1:3 in multiple T175. When they reached 90% confluency, cells were detached and 4 x 10^6 cells/T175 were plated and cultivated again for 72 h at 37°C and 5% CO_2. Conditioned medium was collected, pooled, filtered through a 0.45 µm syringe filter and aliquots were stored at –80°C.

4.2 *In vivo* studies

4.2.1 Mouse breeding and keeping

C57BL/6J #1001 8 week-old female wild type mice were obtained from Janvier Labs. LysM-cre x GRfl/fl (**Figure 4)**, LysM-cre x mT/mG (Clausen, Burkhardt et al. 1999, Tronche, Kellendonk et al. 1999, Tuckermann, Kleiman et al. 2007), CD163-cre x GRfl/fl (**Figure 5**), and CD163-cre x mT/mG transgenic mice (Etzerodt, Tsalkitzi et al. 2019) were bred at the animal facility of the UMM Zentrum für Medizinische Forschung (ZMF) Mannheim and genotyping was performed by PCR using DNA extracted from mouse ear tissue. The primers for the floxed GR allele were 5′ GGCATGCACATTACTGGCCTTCT 3′ and 5′ CCTTCTCATTCCATGTCAGCATGT 3′. Primers for detection of Cre were 5′ AAGAACCTGATGGACATGTTCAGG 3′ and 5′ CGGTGCTAACCAGCGTTTTCGTTC 3′ (LysM-cre), or 5′ AAGCTGAACAACAGGAAATGGTTC 3′ and 5′ GGAGATGTCCTTCACTCTGATTCT 3′ (CD163-cre). All mice were housed under specified pathogen free conditions at the animal facility at ZMF Mannheim with water and food *ad libitum* and 12-h/12-h night/daylight cycle.

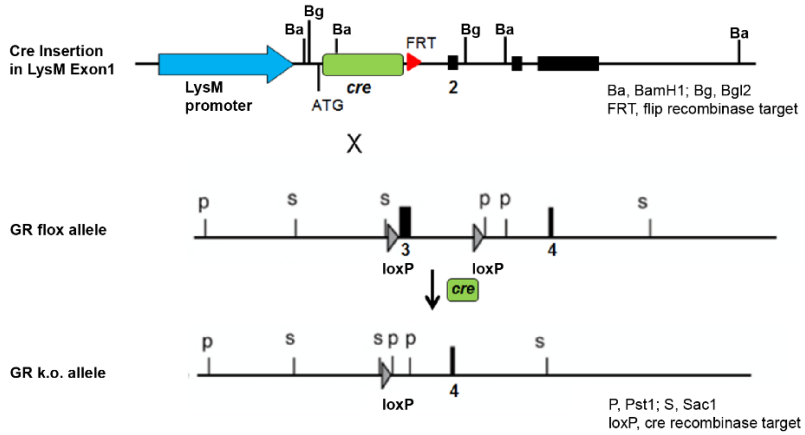

Figure 4. Representation of the LysM-cre x GR flox crossbreeding.
In the LysM-cre line, a Cre recombinase is expressed instead of exon 1 in the gene of the glucocorticoid receptor. In the floxed GR flox variant, exon 3 is flanked by loxP sites. After expression of Cre, exon 3 is deleted, resulting in a GR "loss of function" allele (GR k.o.).

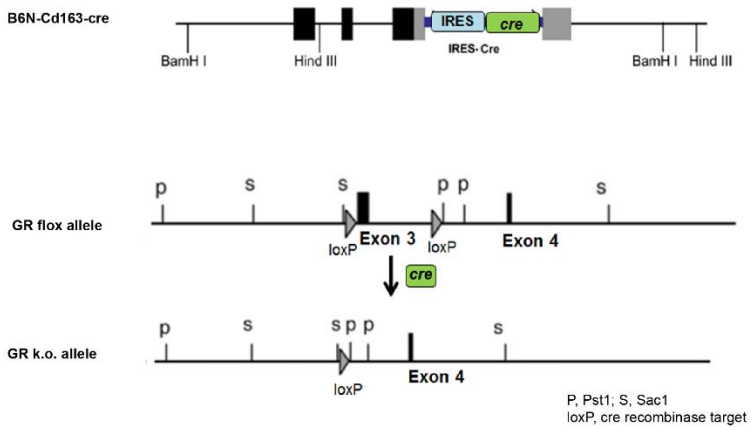

Figure 5. Representation of the CD163-cre x GR flox crossbreeding.
In the Cd163-cre line, a Cre protein is expressed on an allele next to the Cd163 protein. In the floxed GR flox variant, exon 3 is flanked by loxP sites. After expression of cre, exon 3 is removed, resulting in a GR "loss of function" allele (GR k.o.).

4.2.2 Initiation of mouse melanoma models

Subcutaneous tumours were established in 8–12 week-old female mice by s.c. injection of 2.5 x 10^5 B16-F10*luc2* or YUMM1.7 cells in 100 µl sterile PBS, pH 7.4, on the right flank. Tumour size was measured using a digital caliper in x, y, and z and volume was calculated using the equation for volume of an ellipsoid (volume = 0.5233xyz). *In vivo* bioluminescence imaging of B16-F10*luc2* tumours was performed 10 min after i.p. injection of 150 µl 30 mg/ml D-luciferin on an IVIS Spectrum *in vivo* imaging system with 45 sec exposure time and images were analysed using the Living Image Software (version 4.7.2). For aPD-1 antibody treatment, mice received 12.5 mg/kg aPD-1 antibody (clone RMP1-14), or isotype control IgG2a (clone 2A3) by i.p. injection twice a week, with first injection on day 6 after tumour cell inoculation. For treatment with lipid nanoparticles, mice were injected intravenously with 5 ml/kg LNPs by retroorbital injection using a 30G needle attached to a 1 ml syringe three times per week, with first injection 1 day after tumour cell inoculation. For organ preparation, mice were anaesthetised with isofluorane and sacrificed by cervical dislocation. All animal experiments were approved and performed in accordance with the limiting principles for using animal in testing (the three Rs: replacement, reduction, and refinement) and approved by the local authorities (Regierungspräsidium Karlsruhe, approval number G-337/19 and internal approval number I-23/08).

4.2.3 *In vivo* imaging and biodistribution of lipid nanoparticles

Tumour-bearing C57BL/6J mice were injected intravenously with 5 ml/kg PBS, non-targeted IgG or CD169-targeted calcein (Calc)-loaded LNPs (0.5 mM lipid) (n=1) and accumulation of LNPs

was measured at 15, 45, 90 min post injection using an IVIS Spectrum *in vivo* imaging system equipped with filters for ex490/em520 visualization.

4.3 Tissue dissection and isolation of primary cells

4.3.1 Skin tumour preparation

Skin tumours from melanoma bearing mice were excised using sterile forceps, cut into small pieces (~ 1–2 mm) and incubated with 1 ml digestion buffer (DMEM GlutaMAX, 0.1% BSA, 1 mg/ml Collagenase II, 10 µg/ml DNAse I) at 37°C for 30 min under gentle agitation (750 rpm). Following incubation, samples were immediately transferred on ice to slow the enzymatic digestion, strained through a 70 µm cell strainer with PBS/2 mM EDTA and red blood cell (RBC) lysis was performed by incubation with 2 ml RBC lysis buffer for 5 min at RT. The reaction was stopped by adding ice-cold PBS/2 mM EDTA and cells were washed at 400 x g for 5 min at 4°C. Cells were counted and concentration adjusted to 1 x 10^7 cells/ml. 100 µl of cell suspension were transferred to 96-well U-bottom plates for FACS analysis.

4.3.2 Splenocyte isolation

Mouse spleen was removed using sterile forceps and collected in a plate containing ice-cold PBS. Single cell suspension was obtained by cutting the spleen in small pieces and mashing it through a 70 µm cell strainer. Cells were washed with PBS at 400 x g for 5 min at 4°C followed by incubation with 2 ml RBC lysis buffer for 5 min at RT for red blood cell lysis. The reaction was stopped by adding ice-cold PBS/2 mM EDTA and cells were washed at 400 x g for 5 min at 4°C. Splenocytes were resuspended in appropriate buffer for further analysis.

4.3.3 Kupffer cell isolation

Mouse liver was removed using sterile forceps, cut into small pieces (~ 1–2 mm) and incubated with 10 ml digestion buffer (DMEM GlutaMAX, 0.1% BSA, 1 mg/ml Collagenase II, 10 µg/ml DNAse I) at 37°C for 30 min under gentle agitation (750 rpm). Following incubation, samples were immediately transferred on ice to slow the enzymatic digestion, strained through a 70 µm cell strainer with PBS/2 mM EDTA and red blood cell lysis was performed by incubation with 2 ml RBC lysis buffer for 5 min at RT. The reaction was stopped by adding ice-cold PBS/2 mM EDTA and cells were washed at 400 x g for 5 min at 4°C. To separate hepatocytes, cell suspensions were centrifuged at 50 x g for 3 min at 4°C and the top aqueous phase mainly containing KCs,

sinusoidal endothelial cells and satellite cells was transferred to 96-well U-bottom plates for FACS analysis.

4.3.4 Bone marrow cell isolation

Mouse femur and tibiae were removed using sterile forceps, cleaned with EtOH and cut at both ends under sterile conditions. Bone marrow was flushed with ice-cold DMEM GlutaMAX medium using a 10 ml syringe with a 25G needle and the flow through was strained through a 70 µm cell strainer. Bone marrow cells (BMC) were centrifuged at 400 x g for 5 min at 4°C and resuspended in DMEM GlutaMAX for cell counting. BMC were resuspended in appropriate buffer for further analysis or cryopreserved in liquid nitrogen in 1 ml FBS containing 10% DMSO at 10×10^6 BMC/ml until usage.

4.3.5 *Ex vivo* culture of tissue explants

Tumour explants were isolated and cultured in YUMM1.7 complete growth medium for 24 h at 37°C and 5% CO_2. Supernatants were collected and corticosterone measured by ELISA.

4.4 Cell separation

4.4.1 Flow cytometry

2×10^5–2×10^6 cells/well were transferred to 96-well U-bottom plates and washed with PBS at 400 x g for 5 min at 4°C. If subsequent intracellular staining was planned, cells were resuspended in 30 µl PBS containing 1:100 Zombie Aqua or 100 µl PBS containing 1:1500 Zombie NIR fixable viability dye and incubated for 20 min at 4°C in the dark, followed by washing with PBS. For extracellular staining only, cells were incubated with 100 µl PBS containing 1:200 7-AAD 10 min prior to measurement instead. After the last wash, cells were resuspended in 50 µl Fc block and incubated for 20 min at 4°C in the dark, to block unspecific binding of antibodies via the Fc receptors. Cells were then incubated with FACS buffer containing the conjugated antibodies for extracellular staining for 30 min at 4°C in the dark. After washing, the pellet was resuspended in 100 µl FACS buffer for subsequent analysis or intracellular staining was performed. For intracellular staining, cells were first fixed and permeabilized by incubation with 50 µl of Fix/Perm solution (Fixation/Permeabilization Concentrate 1:4 diluted in Fixation/Permeabilization Diluent) for 30 min at 4°C in the dark. After washing the cells with 150 µl of PermWash (10X Permeabilization Buffer diluted 1:10 in ddH_2O), the pellet was resuspended in 50 µl of PermWash buffer containing the

antibodies for intracellular staining and cells were incubated for 30 min at RT in the dark. Subsequently, cells were washed with 150 µl of PermWash buffer and resuspended in 100 µl of PermWash buffer. Flow cytometry analyses were performed with a FACSLyric, LSRFortessa (BD Bioscience) or Cytek Northern Light Spectral Flow Cytometer (Cytek Biosciences) and data was analyzed using FlowJo software (Tree Star).

4.4.2 Magnetic-activated cell sorting (MACS)

CD8+ T cells were isolated from splenocytes by the CD8a+ T cell isolation Kit (mouse) from Miltenyi Biotec according to the manufacturer's instructions. With this kit, CD8+ T cells are isolated by negative selection (negative for CD4, CD11b, CD11c, CD19, CD45R (B220), CD49b (DX5), CD105, MHC-II, Ter-119, and TCRγ/δ).

4.5 Primary cell culture

4.5.1 Generation and polarization of bone marrow-derived macrophages

7×10^6 fresh or 10×10^6 thawed BMC were plated in 10 ml DMEM GlutaMAX containing 10% FBS, 1% P/S and 30 ng/ml recombinant macrophage colony-stimulating factor (M-CSF) in uncoated 10 cm petri dishes. On day 3, the cells were supplemented with 10 ml complete growth medium containing 30 ng/ml M-CSF. On day 6, adherent cells were washed with PBS and trypsinized until the cells started to detach as verified under the microscope. The cells were flushed off the petri dish using complete growth medium, centrifuged at 400 x g for 5 min at 4°C, counted, and plated at an appropriate concentration in 24-well plates with 30 ng/ml M-CSF containing complete growth medium. Bone marrow-derived macrophages (BMDM) were treated with 50% TCM, 100 nM DEX, 10 ng/ml IL-4, 100 ng/ml LPS or 10 ng/ml IFNg ± pre-treatment with 100 nM MF for 30 min as indicated.

4.5.2 Fluorometric assay of Calc-aCD169 treated BMDM

BMDM were seeded in complete growth medium in black clear-bottom 96-well plates at 30,000 cells/well and incubated with non-targeted IgG and CD169-targeted calcein (Calc)-loaded LNPs for 1 h. After three washes in complete growth medium, fluorescence was measured from the bottom of 96-well plates using the Tecan Infinite M200 plate reader at ex490/em520 and indicated time points.

4.6 Functional assays

4.6.1 Enzyme-linked immunosorbent assay (ELISA)

The corticosterone and IL-12p40 ELISA was used according to the manufacturer's instructions.

4.6.2 11β-HSD1 activity assay

BMDM were incubated with 100 nM 11-dehydrocorticosterone (11-DHC) for 3 h at 37°C and 5% CO_2. Formation of corticosterone was determined in the supernatants by ELISA.

4.6.3 Suppression of T cell proliferation assay

Splenic CD8+ T cells were isolated from healthy wild type mice using MACS (see 4.4.2). T cells from one spleen were resuspended in 2 ml of 1 mM CFSE cell proliferation dye dissolved in PBS and incubated for 5 min at 37°C protected from light. T cells were washed with T cell growth medium (RPMI-1640 GlutaMAX supplemented with 10% FBS, 1% P/S, 10 mM HEPES, 50 µM β-mercaptoethanol, 1 mM MEM NEAA, 1 mM sodium pyruvate), centrifuged at 400 x g for 5 min and resuspended in growth medium for counting. To activate T cells, U-bottom 96-well plates were coated with anti-CD3 and anti-CD28 antibodies (0.1 µg/ml each) for 3 h at 37°C. BMDM were stimulated with DEX or TCM/DEX/IL4 for 24 h, after which stimulants were removed and cells were washed three times with PBS to remove residual stimulants. BMDM were detached using an enzyme-free cell dissociation buffer, counted and resuspended in T cell growth medium. Subsequently, 25,000 T cells were co-cultured with stimulated BMDM (MΦ:T cell ratios 1:2 and 1:1.5) at 37°C and 5% CO_2 in 200 µl of T cell growth medium. After incubation for 72 h, cells were stained for CD8 and the proliferation of CD8+ T cells was estimated by measuring the dilution of CFSE staining on the Cytek Northern Light Spectral Flow Cytometer (Cytek Biosciences).

4.7 Gene expression

4.7.1 RNA extraction, reverse transcription, and quantitative PCR (qPCR)

RNA was isolated from tissue or cells with the innuPREP RNA Mini Kit 2.0 (IST innuscreen), according to the manufacturer's instructions, followed by determination of RNA concentration using the microplate reader Tecan Infinite M200 and a Nanoquant plate. Similar amounts of RNA were used for cDNA synthesis (Maxima Reverse Transcriptase, Thermo Fisher Scientific) and quantitative PCR (qPCR) was performed with the MX3000P sequence detection system (Stratagene) under standard conditions. The reaction mix contained 5 ng cDNA, innuMIX qPCR

DSGreen Standard (IST innuscreen), 0.25 µM forward primer, and 0.25 µM reverse primer in a total volume of 20 µl. Relative gene expression compared to two housekeeping genes (β-actin, Erp44) was calculated using the ΔΔCt method.

4.7.2 DNA extraction, PCR, and agarose gel electrophoresis

Tissue samples were treated with 50 µl lysis buffer (100 mM Tris HCl pH 8.0 – 8.5, 0.5 mM EDTA, 0.2% SDS, 200 mM NaCl, 0.3 mg/ml proteinase K) overnight at 56°C with agitation, following dilution with 500 µl ddH_2O and inactivation of proteinase K at 95°C for 10 min. PCR was performed using 1 µl of DNA solution, 0.05 U/µl DFS-Taq DNA Polymerase, 1X buffer (with $MgCl_2$), 0.2 mM dNTP, 0.03 pmol/µl forward primer, 0.03 pmol/µl reverse primer, in a total volume of 20 µl on a thermal cycler using protocol A (LysM-cre, GRflox) or B (CD163-cre).

Protocol A:

95°C, 3 min	
95°C, 30 sec 60°C, 30 sec 72°C, 45 sec	34x
72°C, 5 min	

Protocol B:

95°C, 3 min	
95°C, 25 sec 65°C, 20 sec (-0.5°C per cycle) 72°C, 1 min	10x
95°C, 25 sec 60°C, 30 sec 72°C, 1 min	34x
72°C, 5 min	

Agarose gel electrophoresis of PCR products were performed on a 1.2% agarose gel containing 10% Nancy-520 at 100 V for 30 min and DNA was visualized using the Intas Gel Stick Imager.

4.8 Formulation of lipid nanoparticles

4.8.1 Preparation of lipid nanoparticles

Lipid nanoparticles (LNPs) were formulated from a mixture of 1,2,3-tri(*cis*-9-octadecenoyl) glycerol (triolein), 1-palmitoyl-2-oleyl-*sn*-glycero-3-phosphocholine (POPC), N-(carbonyl-methoxypolyethylene glycol-2000)-1,2-distearoyl-*sn*-glycero-3-phosphoethanolamin, (mPEG2000-DSPE), 1,2-distearoyl-*sn*-glycero-3-phosphoethanolamine-n-[dibenzocyclooctyl(polyethylene glycol)-5000] (DSPE-PEG5000-DBCO), and ± mifepristone (MF, RU-486) (molar ratios as indicated) using a microfluidic mixing method on a NanoAssemblr Ignite. Briefly, lipids and MF were dissolved in absolute EtOH and the EtOH-lipid solution was injected in the first inlet, and 0.9% NaCl into the second inlet of the micromixer. The appropriate flow rate ratios (FRR, ratio of aqueous stream volumetric flow rate to ethanolic volumetric flow rate) were set by maintaining a constant flow rate

of 5 ml/min in the ethanolic channel and varying the flow rates of the aqueous channel. Aqueous dispersions of LNPs were collected and dialyzed twice against 154 mM NaCl overnight at 4°C (molecular weight cut-off of 14 kDa) to remove the residual ethanol.

4.8.2 Particle size determination

All LNP formulations were tested by dynamic light scattering (DLS) on the DynaPro NanoStar (Wyatt Technology Europe GmbH, Dernbach, Germany) to determine their size (diameter) and polydispersity. Nanoparticle Tracking Analysis (NTA) was performed using a ZetaView.

4.8.3 Determination of drug loading

Drug loading was analyzed by high performance liquid chromatography (HPLC) on a Dionex UltiMate 3000 HPLC system (Thermo Scientific, Dreieich, Germany), equipped with a reverse phase column (Nucleodur C18 Gravity, 100 x 4 mm, analytical), and a UV-diode array detector (205 nm, 300 nm). The solvent system used was a gradient of MeOH:water (containing 0.9% TFA) (0–10 min: 10–99% MeOH) at a flow rate of 1 ml/min. Loading efficiencies were determined by quantitating both MF and lipid levels by HPLC after removing external MF from LNP encapsulated MF by dialysis against 154 mM NaCl overnight at 4°C (molecular weight cut-off of 14 kDa) and separation of precipitated drug by centrifugation. Loading efficiencies were calculated using the following formula:

$$\text{Loading efficiency } [\%] = \frac{(\text{MF-to-lipid ratio in LNPs})}{(\text{MF-to-lipid ratio in formulation})} \times 100$$

4.8.4 Antibody functionalization and conjugation to lipid nanoparticles

Briefly, 2.5 ml of freshly made 10 mM sodium periodate solution ($NaIO_4$) was added to 2.5 ml of antibody solution (2 mg/ml) in reaction buffer (0.15 M NaCl, 0.1 M sodium acetate, pH 5.5), and incubated for 60 min at RT. After incubation, samples were washed 5 times with reaction buffer (0.15 M NaCl, 0.1 M sodium acetate, pH 5.5) using 50 kDa cut-off spin columns to reduce the remaining excess $NaIO_4$. While vortexing, aminooxy-PEG3-azide solution and an aniline catalyst was added to the purified oxidized antibody and the mixture was incubated overnight at 4°C in an end-over-end mixer. The molar ratio of oxidized antibody and aminooxy-PEG3-azide was 1:20. After incubation, free aminooxy-PEG3-azide and aniline catalyst were washed away, using the same procedure for washing as described above. The azide-functionalized antibody was then conjugated to DBCO-PEG5000-LNPs overnight at 4°C in an end-over-end mixer.

4.9 Statistical analysis

Statistical analysis was conducted using the GraphPad Prism software on at least three biological replicates. Two groups were compared with the unpaired two-tailed Student's t test assuming Gaussian distribution of the data. The Mann-Whitney test was employed for not normal distributed data. *, $P < 0.05$; **, $P < 0.01$; ***, $P < 0.001$; ****, $P < 0.0001$.

5 Results

5.1 Expression of steroidogenic enzymes in murine tumour tissue

The immune system has the capacity to fight cancer, however signals present within the tumour microenvironment (TME) actively suppress anti-tumour immune responses. Glucocorticoids (GCs) are steroid hormones with potent immunosuppressive properties and the sensitivity of the immune system to GCs is well-described. The primary source of GCs is the adrenals, where they are generated via de novo synthesis from cholesterol, the first step catalysed by the rate-limiting enzyme Cyp11A1. A second pathway recycles active GCs from inactive metabolites via the activity of 11β-hydroxysteroid dehydrogenase type 1 (11β-HSD1, encoded by *HSD11B1*).

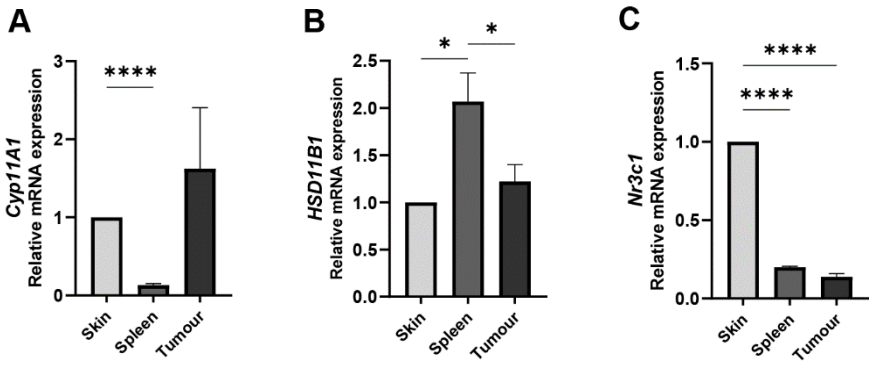

Figure 6. Expression of *Cyp11A1*, *HSD11B1* and *Nr3c1* in murine skin, spleen and tumour tissue.
(A) Relative gene expression of *Cyp11A1*, **(B)** *HSD11B1*, and **(C)** *Nr3c1* in murine skin, spleen and YUMM1.7 tumour tissue. Data are represented as mean ± SEM of n=3. Statistically significant differences were calculated using an Unpaired t test. *, P < 0.05; ****, P < 0.0001.

First, it was investigated if there was evidence of extra-adrenal steroidogenesis in the tumour, potentially leading to evasion of anti-tumour immunity. cDNA was generated from RNA isolated from spleen and skin from healthy wild type mice, as well as from tumour tissue from YUMM1.7 tumour-bearing wild type mice, and qPCR analysis was performed. Gene expression analysis revealed similar expression levels of *Cyp11A1* in tumour tissue compared to skin and spleen (**Figure 6. A**). The expression of *HSD11B1* was 2-fold higher in the spleen compared to skin and tumour tissue (**Figure 6. B**), while *Nr3c1*, the gene encoding for the glucocorticoid receptor (GR), showed highest expression in the skin (**Figure 6. C**). These findings are in line with previously reported evidence of extraadrenal steroidogenesis in the tumour and other (Slominski, Tuckey et al. 2020, Anderson and Acharya 2022).

5.2 Knockout of GR in TAM reduces tumour growth in murine melanoma models

Tumour-associated macrophages (TAMs) are the most abundant immune cells found in solid tumours, and their contribution to tumour progression is well documented. To analyse the effect of GR-responsive TAMs on tumour development, tumour growth was analysed in mice with conditional targeting of the *Nr3c1* gene, crossed with mice expressing the Cre recombinase under the control of the lysozyme (LysM) promoter to induce selective ablation of the *Nr3c1* gene in myeloid cells ($GR^{f/fLysMcre}$) (**Figure 4**).

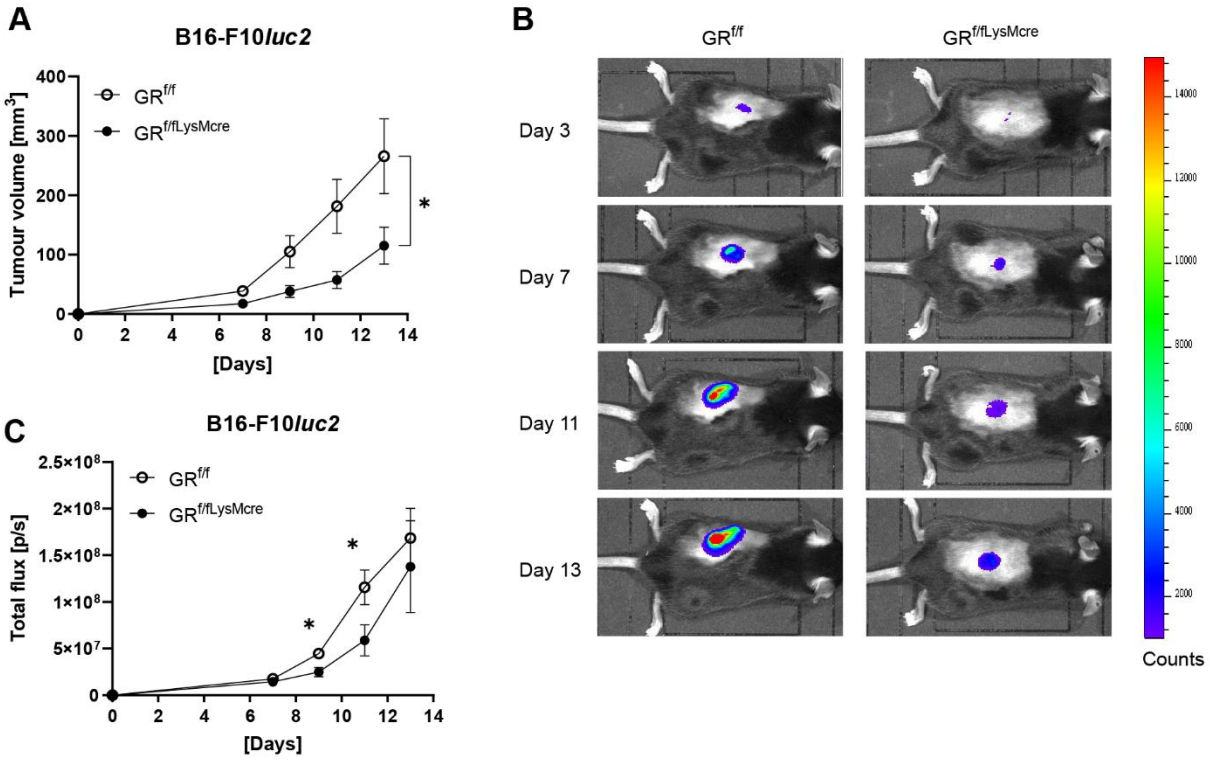

Figure 7. Growth curves of B16-F10*luc2* tumours in $GR^{f/fLysMcre}$ mice.
(A) B16-F10*luc2* tumour cells (2.5 x 10^5) were s.c. injected into wild type (○ $GR^{f/f}$) and transgenic (● $GR^{f/fLysMcre}$) mice on day 0 and tumour growth was monitored. **(B)** Representative bioluminescence images after i.p. injection of D-luciferin acquired using an IVIS *in vivo* imaging system. All images were adjusted to the bioluminescence scale bar shown at right, with red being the most intense and violet the least intense. **(C)** Semi-quantitative results of the tumour burden measured by bioluminescence. Data are represented as mean ± SEM of n=9. Statistically significant differences were calculated using an Unpaired t test. *, $P < 0.05$.

Transgenic $GR^{f/fLysMcre}$ mice showed improved control of B16-F10*luc2* tumours with the mean tumour volume at endpoint reduced by 56.75% compared to their wild type litter mates ($GR^{f/f}$: 265.87 mm^3 ± 59.35 mm^3; $GR^{f/fLysMcre}$: 115.00 mm^3 ± 29.44 mm^3; p=0.0475) (**Figure 7. A**)

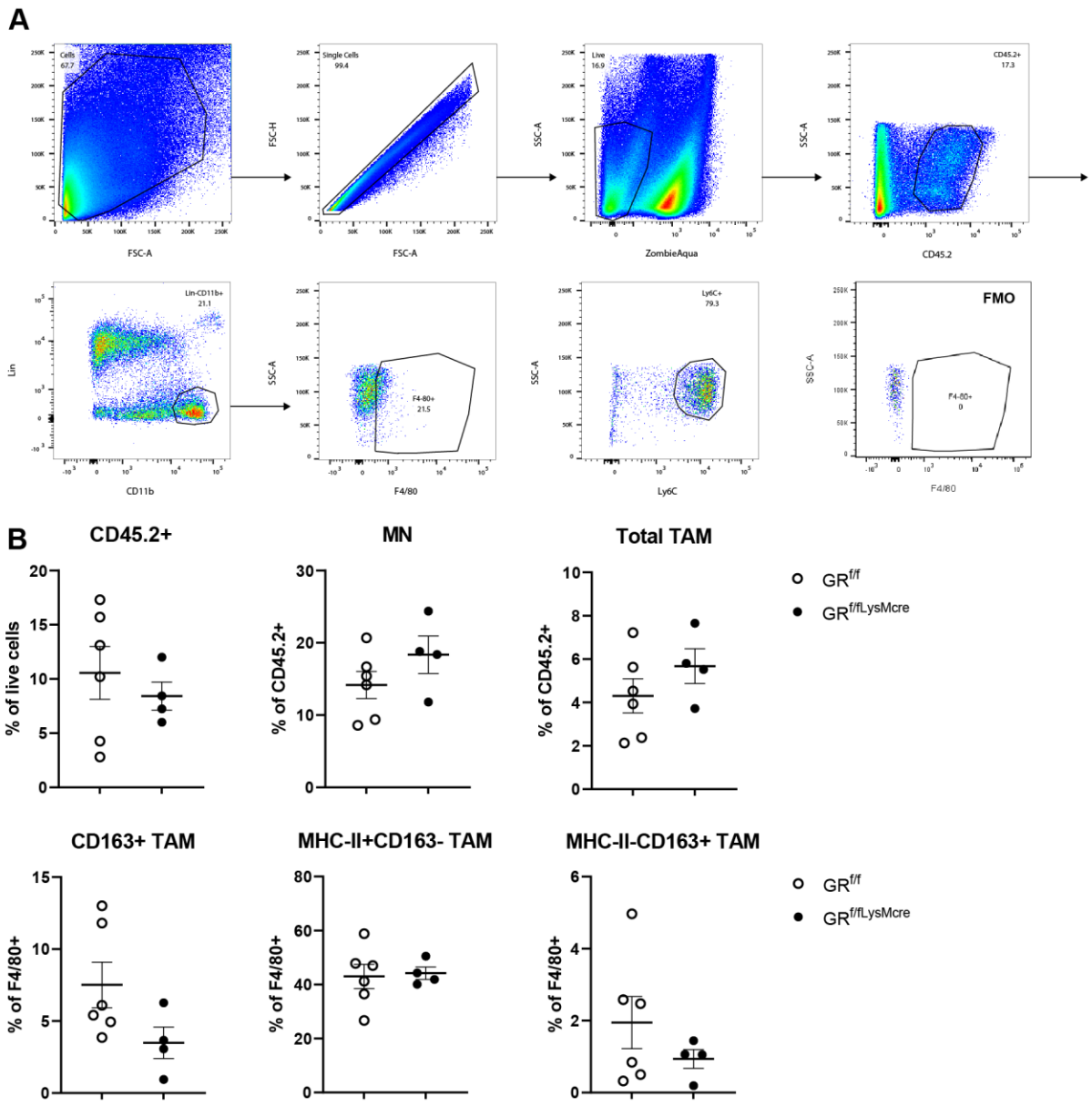

Figure 8. FACS analysis of B16-F10*luc2* tumours in GR$^{f/fLysMcre}$ mice.
(A) Gating strategy. MNs were defined as CD45.2+ Lin-(CD19, CD3, NK1.1, Ly6G, SiglecF) CD11b+ Ly6C+ and TAMs as CD45+ Lin-(CD19, CD3, NK1.1, Ly6G, SiglecF) CD11b+ F4/80+. **(B)** FACS analysis of B16-F10*luc2* tumours from wild type (○ GR$^{f/f}$) and transgenic (● GR$^{f/fLysMcre}$) mice. Data are represented as mean ± SEM of n=4-6.

This was further validated by bioluminescence imaging for semi-quantitative tumour burden assessment using i.p. administration of D-luciferin (GR$^{f/f}$: 1.68E+08 ± 3.01E+07 total flux; GR$^{f/fLysMcre}$: 1.38E+08 ± 4.65E+07 total flux; p=0.2973 on day 13; GR$^{f/f}$: 1.16E+08 ± 1.76E+07 total flux; GR$^{f/fLysMcre}$: 5.89E+08 ± 1.57E+07 total flux; p=0.0370 on day 11) (**Figure 7. B, C**). Subsequently, to analyse the effect of GR-depletion on the frequency and phenotype of monocytes (MNs) and TAMs, flow cytometry analysis was performed. MNs were gated as CD45.2+ Lin-(CD19, CD3,

NK1.1, Ly6G, SiglecF) CD11b+ Ly6C+, TAMs as CD45+ Lin-(CD19, CD3, NK1.1, Ly6G, SiglecF) CD11b+ F4/80+ and the expression of CD163 and major histocompatibility complex class II (MHC-II) was analysed. The expression of CD163 by TAMs is associated with an immunosuppressive, pro-tumoural phenotype and has been shown to be a particularly strong indicator of poor prognosis in human melanoma (Jensen, Schmidt et al. 2009, Bronkhorst, Ly et al. 2011, Lee, Lee et al. 2019). Downregulation of MHC-II by TAMs restrains their antigen-presenting function and is associated with a pro-tumour phenotype (Wang, Li et al. 2011). No changes in the frequency of infiltrating MNs and TAMs, as well as the TAM phenotype assessed by the expression of CD163 and MHC-II was detected (**Figure 8**).

In contrast to the relatively high immunogenicity observed in human melanomas, the B16-F10 syngeneic melanoma model exhibits low immune infiltration and lacks human-relevant driver mutations (Zhong, Myers et al. 2020). These differences suggest that the B16-F10 model does not fully recapitulate features of human tumour populations from the same tissue. Activating mutations in BRAF are the most prevalent in human melanoma and are often accompanied by loss of tumour suppressor loci such as PTEN and CDKN2A. YUMM1.7 (Yale University Mouse Melanoma) cells are derived from a genetically engineered, spontaneous melanoma mouse model harbouring the human-relevant driver mutations $Braf^{V600E}$, $Pten^{-/-}$ and $Cdkn2a^{-/-}$, and exert higher immunogenicity compared to the B16-F10 model (Meeth, Wang et al. 2016).

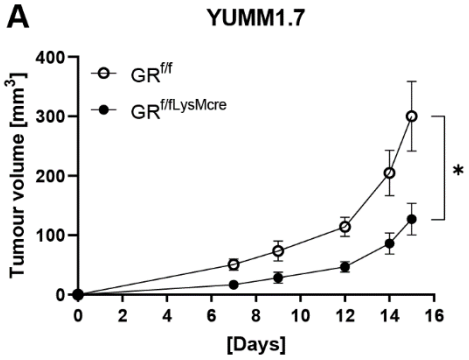

Figure 9. Growth curves of YUMM1.7 tumours in $GR^{f/fLysMcre}$ mice.
(A) YUMM1.7 tumour cells (2.5 x 10^5) were s.c. injected into wild type (○ $GR^{f/f}$) and transgenic (● $GR^{f/fLysMcre}$) mice on day 0 and tumour growth was monitored. Data are represented as mean ± SEM of n=9. Statistically significant differences were calculated using an Unpaired t test. *, $P < 0.05$.

Development of YUMM1.7 tumours was significantly decreased in transgenic $GR^{f/fLysMcre}$ mice, with the mean tumour volume at endpoint reduced by 57.67% compared to their wild type littermates ($GR^{f/f}$: 300.17 mm^3 ± 55.34 mm^3; $GR^{f/fLysMcre}$: 127.06 mm^3 ± 25.55 mm^3; p=0.0163) (**Figure 9**). Subsequent flow cytometry analysis revealed lower infiltration of CD163+ TAM in $GR^{f/fLysMcre}$

transgenic mice compared to their wild type littermates. In line with this, MHC-II- CD163+ TAM subsets and CD86- CD163+ TAM subsets were also reduced in GR$^{f/fLysMcre}$ transgenic mice compared to their wild type littermates (**Figure 10. B, C**).

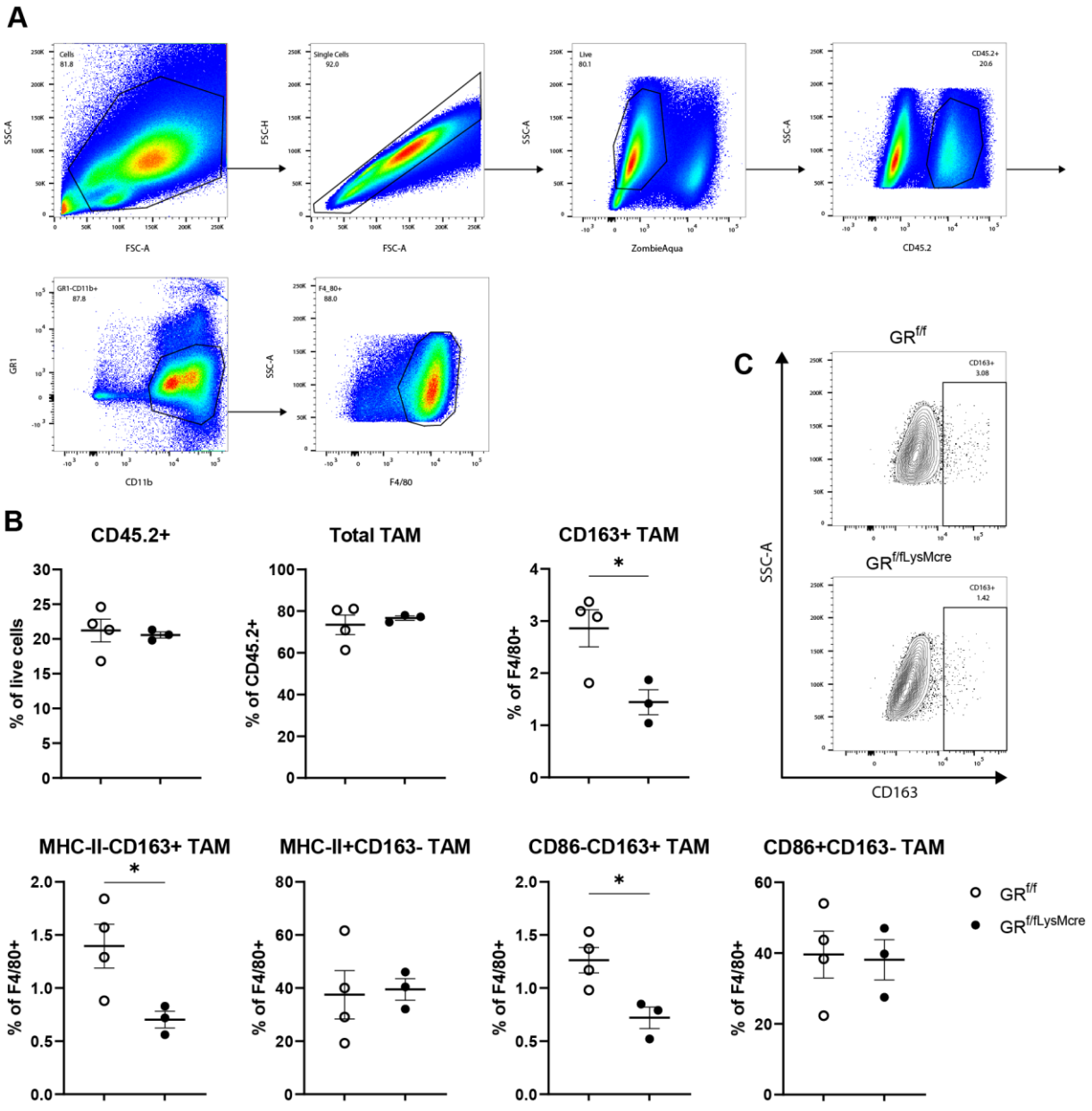

Figure 10. FACS analysis of YUMM1.7 tumours in GR$^{f/fLysMcre}$ mice.
(A) Gating strategy. TAMs were defined as CD45.2+ GR1- CD11b+ F4/80+. **(B)** FACS analysis of YUMM1.7 tumours from wild type (○ GR$^{f/f}$) and transgenic (● GR$^{f/fLysMcre}$) mice. **(C)** Representative FACS plots of CD163+ TAMs in GR$^{f/f}$ and GR$^{f/fLysMcre}$ mice. Data are represented as mean ± SEM of n=3-4.

Specific depletion of CD163+ TAMs has previously been shown to result in mobilization of inflammatory monocytes and strong infiltration of activated T cells, leading to anti-tumour immunity and tumour regression in a murine melanoma model (Etzerodt, Tsalkitzi et al. 2019). To decipher the

impact of GC-responsive CD163+ TAMs to tumour development, subcutaneous tumours were established in mice expressing Cre recombinase under the control of the CD163 promoter to induce selective ablation of the *Nr3c1* gene in CD163+ macrophage subsets ($GR^{f/fCD163cre}$) (**Figure 5**).

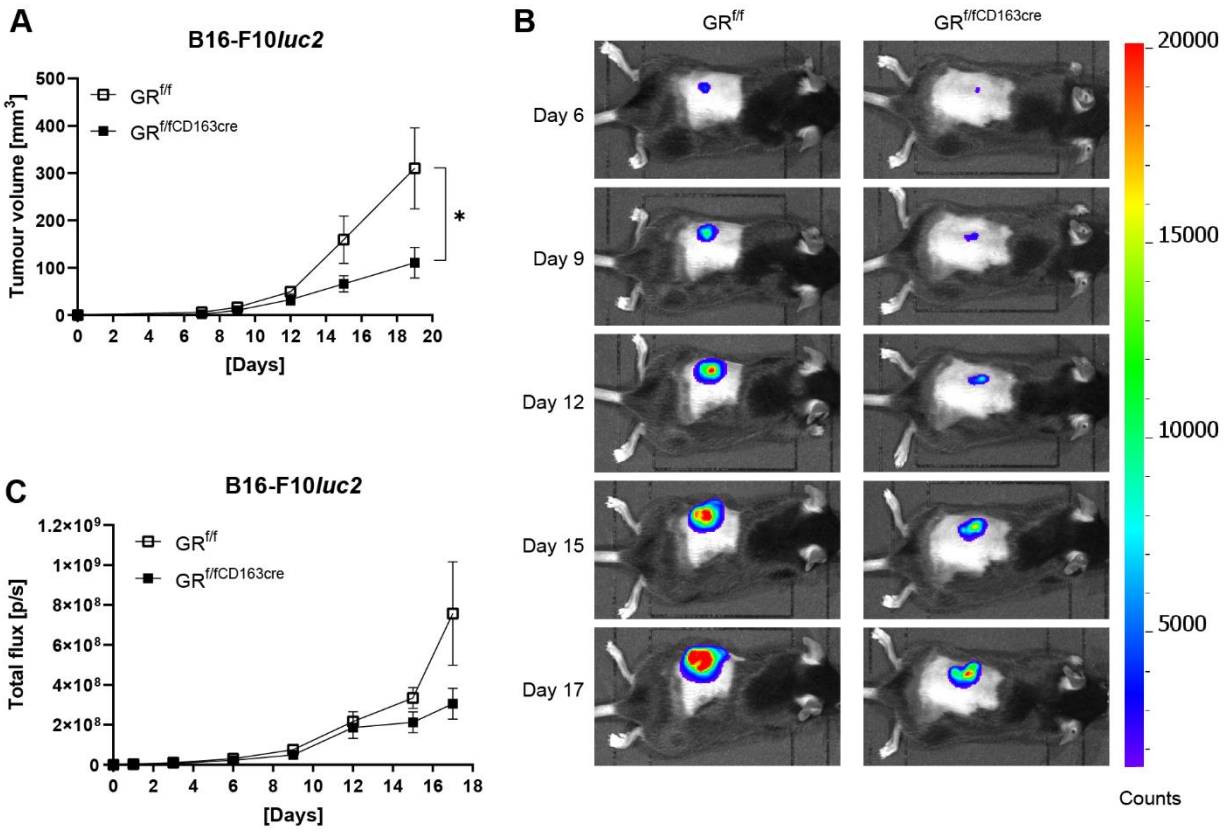

Figure 11. Growth curves of B16-F10*luc2* tumours in $GR^{f/fCD163cre}$ mice.
(A) B16-F10*luc2* tumour cells (2.5 x 10^5) were s.c. injected into wild type (□ $GR^{f/f}$) and transgenic (■ $GR^{f/fCD163cre}$) mice on day 0 and tumour growth was monitored. **(B)** Representative bioluminescence images after i.p. injection of D-luciferin acquired using an IVIS *in vivo* imaging system. All images were adjusted to the bioluminescence scale bar shown at right, with red being the most intense and violet the least intense. **(C)** Semi-quantitative results of the tumour burden measured by bioluminescence. Data are represented as mean ± SEM of n=5-6. Statistically significant differences were calculated using an Unpaired t test. *, $P < 0.05$.

B16-F10*luc2* tumour growth in $GR^{f/fCD163cre}$ transgenic mice demonstrated significant reduction of mean tumour volumes by 64.35% compared to their respective wild type littermates ($GR^{f/f}$: 310.00 mm^3 ± 76.40 mm^3; $GR^{f/fCD163cre}$: 110.52 mm^3 ± 29.55 mm^3; p=0.0435) (**Figure 11. A**). However, this could not be validated by bioluminescene imaging of the tumour burden after i.p. administration of D-luciferin ($GR^{f/f}$: 7.58E+08 ± 2.32E+08 total flux; $GR^{f/fCD163cre}$: 3.06E+08 ± 7.00E+07 total flux; p=0.1023) (**Figure 11. B, C**). In line with this, YUMM1.7 tumour growth and

TAM phenotype analysed by flow cytometry was not affected by the $GR^{f/fCD163cre}$ genotype, although a trend towards a decreased frequency of CD86- CD163+ TAMs was observed (p=0.0718) (**Figure 12. A, B**).

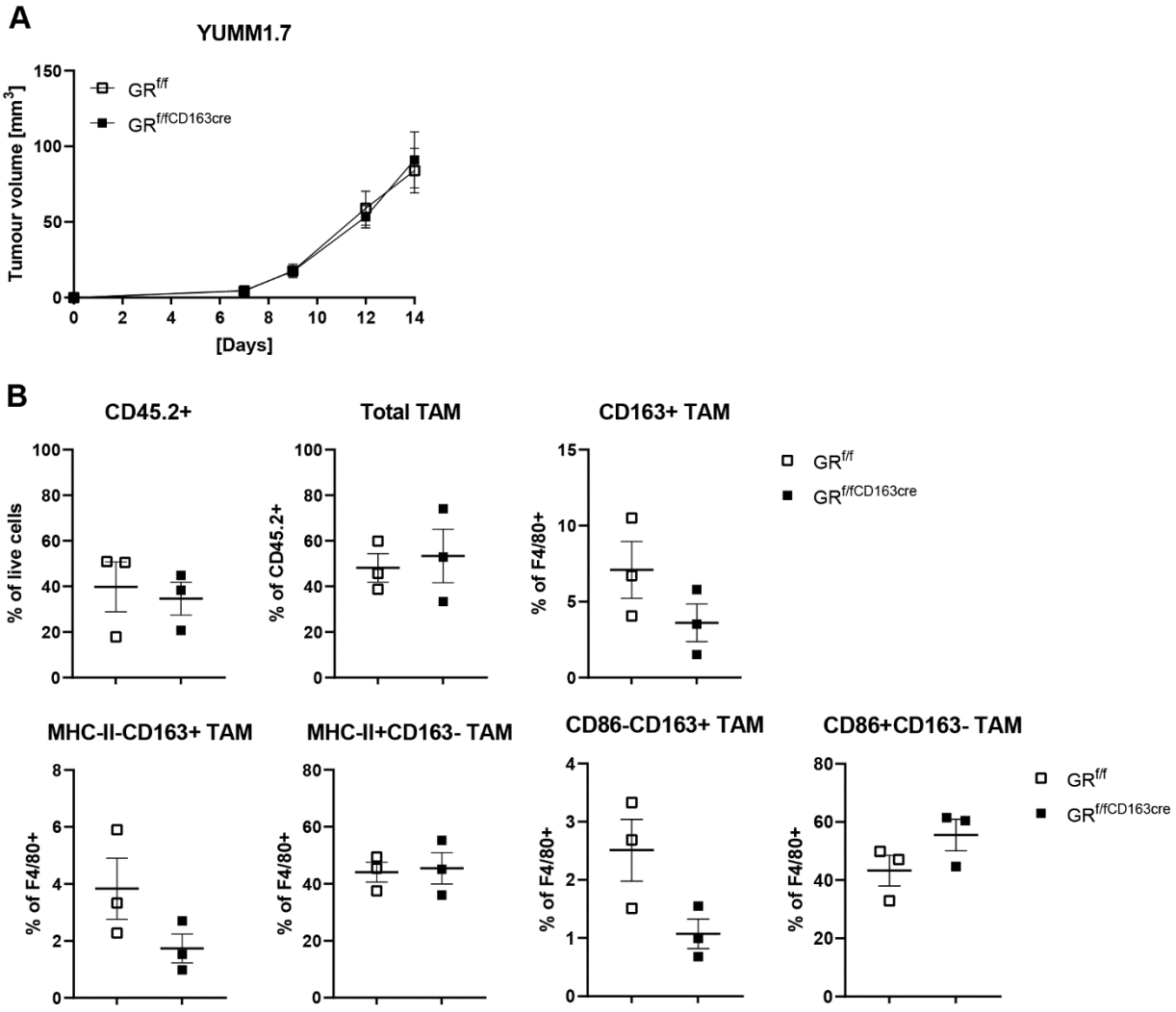

Figure 12. Growth curves and FACS analysis of YUMM1.7 tumours in $GR^{f/fCD163cre}$ mice.
(A) YUMM1.7 tumour cells (2.5×10^5) were s.c. injected into wild type (□ $GR^{f/f}$) and transgenic (■ $GR^{f/fCD163cre}$) mice on day 0 and tumour growth was monitored. Data are represented as mean ± SEM of n=9. **(B)** FACS analysis of YUMM1.7 tumours. Data are represented as mean ± SEM of n=3.

5.3 Expression patterns of Cre recombinase in macrophage-Cre mouse strains

Accurate knowledge of the specificity of Cre expression in $GR^{f/fLysMcre}$ and $GR^{f/fCD163cre}$ transgenic mice is critical in order to make conclusions about the contribution of specific cell types to the tumour growth control observed. Therefore, LysM-cre and CD163-cre mice were crossed to the global two-colour fluorescent mT/mG Cre-reporter mouse (Muzumdar, Tasic et al. 2007). These mice possess loxP sites on either side of a membrane-targeted tdTomato (mT) cassette and express strong red fluorescence in all tissues and cell types. When bred to Cre recombinase expressing mice, the offspring display deletion of the mT cassette in Cre-expressing tissue, allowing expression of the membrane-targeted EGFP (mG) cassette in both Cre recombinase-expressing cells and their subsequent cell lineages (**Figure 13**).

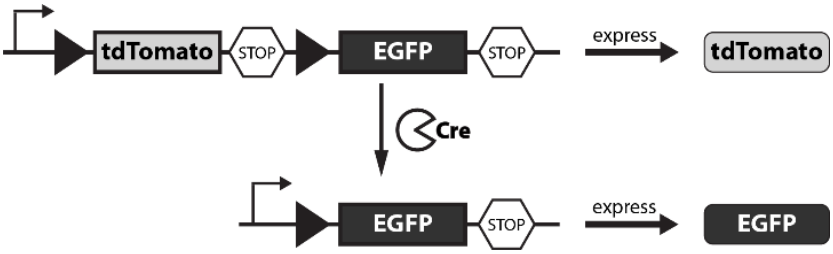

Figure 13. Schematic diagram of the *mT/mG* construct before and after Cre-mediated recombination.
mT/mG is a cell membrane-targeted, two-colour fluorescent Cre-reporter allele, expressing cell membrane-localized tdTomato (mT) fluorescence prior to, and cell membrane-localized EGFP (mG) following, Cre-mediated recombination. Arrows denote the direction of transcription. Triangles represent loxP target sites for Cre-mediated recombination.

The mouse spleen is divided into the white pulp (WP) and the red pulp (RP), separated by the marginal zone (MZ), and contains distinct macrophage populations. The predominant type of macrophages are the red pulp macrophages (RPM), characterized by expression of F4/80+ CD11b- and the presence of CD163, which plays a role in clearing aged red blood cells and regulating iron metabolism. Marginal zone macrophages (MZM) and white pulp macrophages (WPM) (also called metallophilic macrophages), have roles in the capture of microbes and viruses from the circulation. MZM and WPM are characterised by the expression of CD11b+ F4/80- and lack of CD163 expression, while WPM also express high levels of CD169 (Davies, Jenkins et al. 2013, Borges da Silva, Fonseca et al. 2015).

In LysM-cre mT/mG mice, high deletion efficiency was observed in monocytes (60.5%), mature macrophages (RPMs 83%; WPMs 52.1%), and granulocytes (75.7%). Partial deletion (9.8%) was detected in CD11c+ splenic dendritic cells which are closely related to the monocyte/macrophage

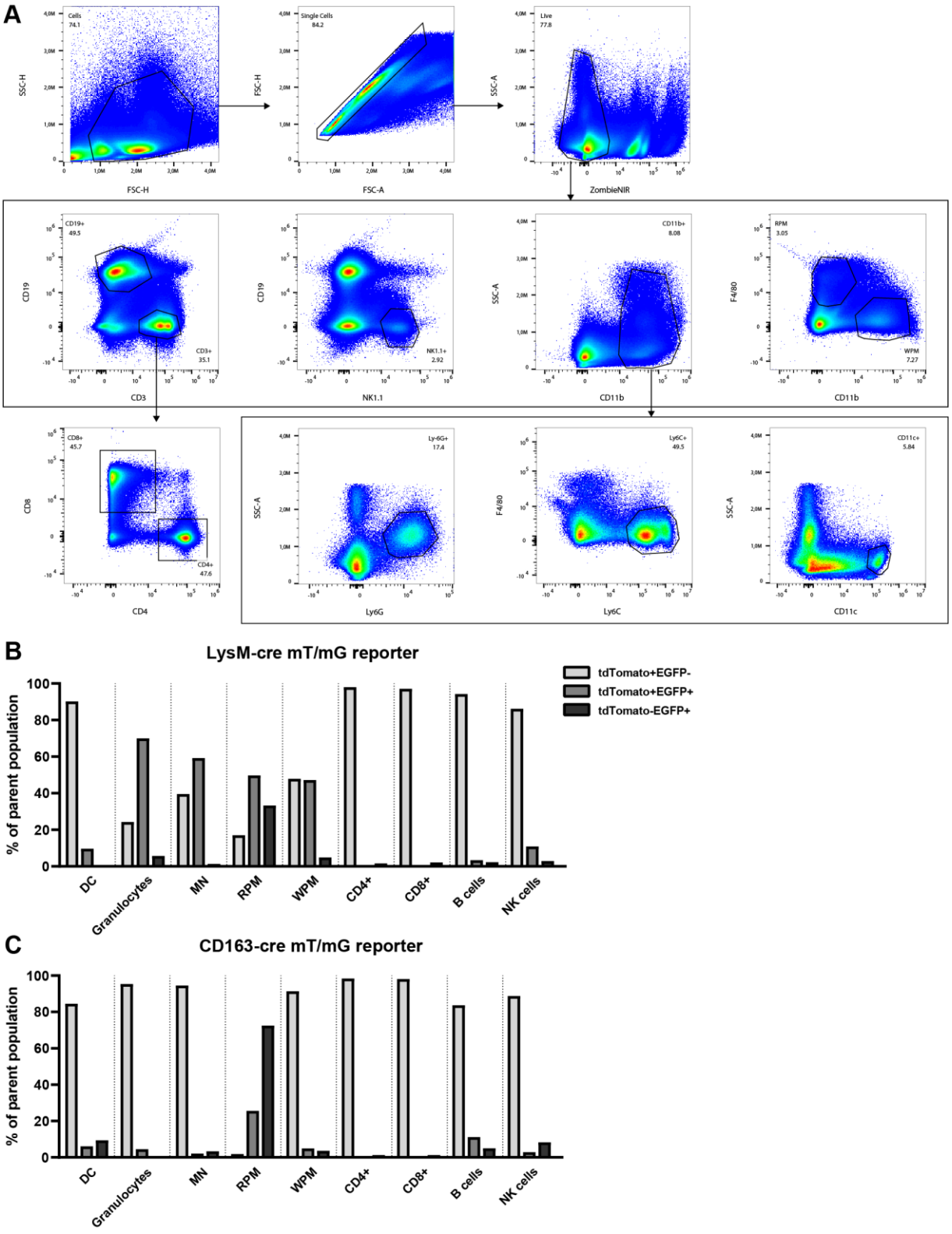

Figure 14. Cre-mediated deletion in the spleen of LysM-cre and CD163-cre mT/mG reporter mice.
(A) Gating strategy of cell types analysed by flow cytometry. Dendritic cells (DC) were defined as CD11b+ CD11c+, granulocytes as CD11b+ Ly6G+, monocytes (MN) as CD11b+ F4/80- Ly6C+, red-pulp macrophages (RPM) as CD11b+ F4/80-, white-pulp macrophages (WPM) as CD11b+ F4/80-, T cells as CD19- CD3+ CD4+ or CD8+, B cells as CD3-

CD19+, and natural killer cells (NK cells) were defined as CD19- NK1.1+. **(B)** Expression of tdTomato (EGFP+/-tdTomato+) and EGFP (EGFP+tdTomato-) in splenic cell populations in LysM-cre mT/mG (wt/tg; wt/tg) and **(C)** CD163-cre mT/mG (wt/tg; wt/tg) reporter mice (n=1).

lineage, and in NK cells (13.8%). In contrast, no relevant deletion was observed in T and B cells (**Figure 14. B**). In CD163-cre mT/mG, EGFP expression was mainly detected in RPMs (98.15%), which are known to express high levels of CD163, and to a lower extent in the myeloid compartment of WPMs (8.6%) and monocytes (5.5%) (**Figure 14. C**). These findings are in line with previously found deletion efficiencies and specificities of the LysM-cre and CD163-cre mouse strains (Abram, Roberge et al. 2014, Etzerodt, Tsalkitzi et al. 2019).

5.4 Ablation of TAM expressed GR restores effectiveness of checkpoint immunotherapy in aPD-1–resistant melanoma

TAMs modulate the efficacy of various forms of anticancer therapy (De Palma and Lewis 2013) and their ability to limit the efficacy of aPD-1 checkpoint immunotherapy has been demonstrated (Dong, Strome et al. 2002, Kleffel, Posch et al. 2015, Arlauckas, Garris et al. 2017, Tang, Liang et al. 2018).

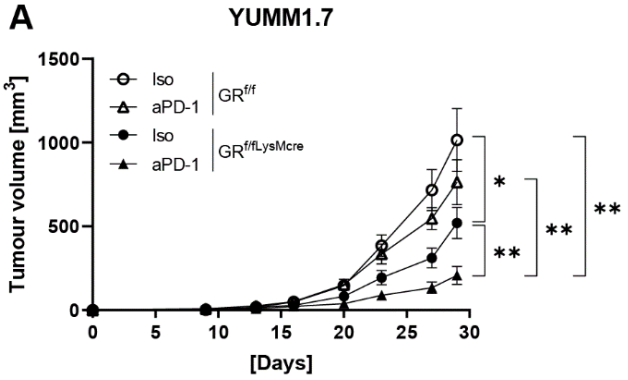

Figure 15. Response to aPD-1 checkpoint immunotherapy in $GR^{f/fLysMcre}$ mice.
(A) YUMM1.7 tumour-bearing $GR^{f/f}$ wild type or $GR^{f/fLysMcre}$ transgenic mice were treated with 12.5 mg/kg PD-1 mAbs (aPD-1) or isotype Ctrl (Iso) twice per week starting on day 6 after tumour cell inoculation, and tumour growth was monitored. Data are represented as mean ± SEM of n=12. Statistically significant differences were calculated using an Unpaired t test. *, $P < 0.05$; **, $P < 0.01$.

TAMs express ligand molecules for checkpoint receptors, such as PD-L1/2, CD80, CD86 and V-domain immunoglobulin suppressor of T cell activation (VISTA). The presence of checkpoint inhibitors different from those targeted by the current antibody treatment diminishes the benefit of

the therapy and maintains immunosuppression in the TME. Strategies to inhibit the interference of TAMs to block resistance to immunotherapy and promote T cell activation are currently tested. The impact of GC-responsive TAMs on the efficiency of aPD-1 checkpoint immunotherapy was investigated in the YUMM1.7 melanoma model, which is inherently resistant to PD-1 mAbs treatment (**Figure 15**). In line with previous findings, tumour growth was significantly reduced in $GR^{f/fLysMcre}$ transgenic mice with reduction in mean tumour volume of 48.86% compared to their $GR^{f/f}$ wild type littermates (Iso/$GR^{f/f}$: 1015.05 mm^3 ± 180.46 mm^3; Iso/$GR^{f/fLysMcre}$: 520.93 mm^3 ± 88.33 mm^3; p=0.0317).

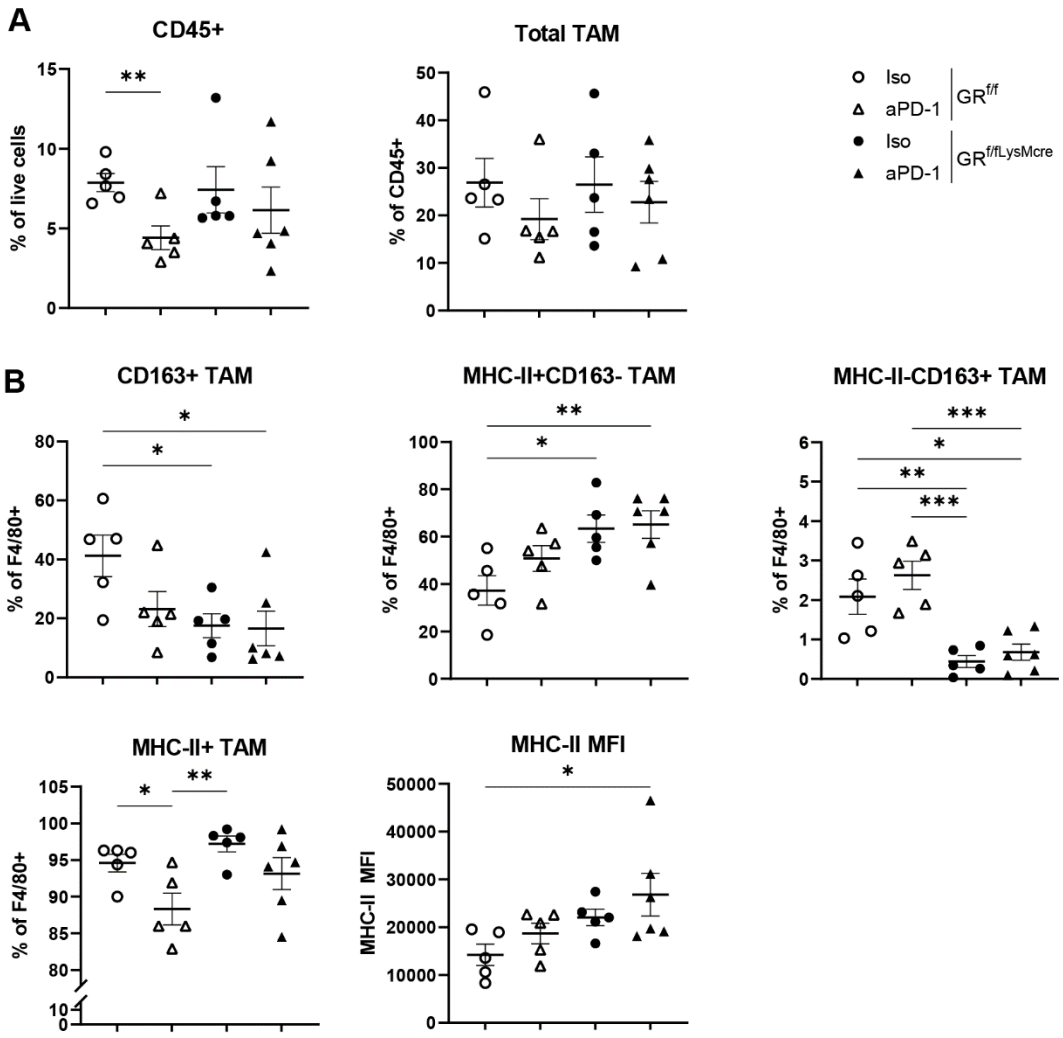

Figure 16. Characterization of TAMs in PD-1 mAbs treated YUMM1.7 tumour-bearing $GR^{f/fLysMcre}$ mice.
aPD-1 or isotype (Iso) treated $GR^{f/f}$ wild type or $GR^{f/fLysMcre}$ transgenic mice were analysed by flow cytometry. **(A)** Frequency of CD45+ cells and total TAMs (CD45+ CD11b+ Lin-(CD3-CD19, NK1.1, Ly6G, SiglecF) F4/80+). **(B)** Frequency of CD163 and **(C)** MHC-II expressing TAMs. **(D)** Co-expression of CD163 and MHC-II by TAMs. Data are represented as mean ± SEM of n=5. Statistically significant differences were calculated using an Unpaired t test. *, P < 0.05; **, P < 0.01.

As expected, aPD-1 treatment had no effect on tumour growth in $GR^{f/f}$ wild type mice, however, in the absence of TAM-expressed GR, aPD-1 treatment significantly restricted tumour growth rates, leading to an overall reduction in mean tumour volumes of 79.46% compared to Iso-treated and 72.71% compared to the aPD-1 treated $GR^{f/f}$ wild type littermates respectively (aPD-1/$GR^{f/f}$: 764.13 mm^3 ± 128.06 mm^3; aPD-1/$GR^{f/fLysMcre}$: 208.50 mm^3 ± 51.48 mm^3; p=0.017) (**Figure 15**). Subsequently, TAMs (CD45.2+ Lin-(CD3, CD19, NK1.1, Ly6G, SiglecF) F4/80+) cells) and infiltrating CD8+ T cells (CD45.2+ Lin-(CD19, NK1.1, Ly6G, SiglecF) CD4- CD8+ cells) and CD4+ T cells (CD45.2+ Lin-(CD19, NK1.1, Ly6G, SiglecF) CD8- CD4+ cells) were analysed by flow cytometry. Analysis of TAMs revealed lower infiltration of CD163+ and MHC-II- CD163+ TAMs in Iso/$GR^{f/fLysMcre}$ and aPD-1/$GR^{f/fLysMcre}$ mice. In line with this, frequencies of MHC-II+ TAMs and MHC-II+ CD163- TAM subsets were increased, suggesting a more anti-tumour phenotype in GC-nonresponsive TAMs.

Next, the effect of aPD-1 treatment on T cells was analysed. Interestingly, T cells demonstrated no changes in cell frequency upon PD-1 mAb treatment, however reduction of T cell exhaustion markers TIM-3 and LAG-3, as well as increase in CD8+ TIM-3- PD-1- T cells was observed in Iso/$GR^{f/fLysMcre}$ mice. Previously it was shown that CD8+ Tim-3- PD-1- double-negative TILs exhibit good effector function (Sakuishi, Apetoh et al. 2010, Anderson, Joller et al. 2016), suggesting a more activated T cell phenotype. However, due to limitations in FACS markers, this was not validated by parallel analysis of T cell activation marker.

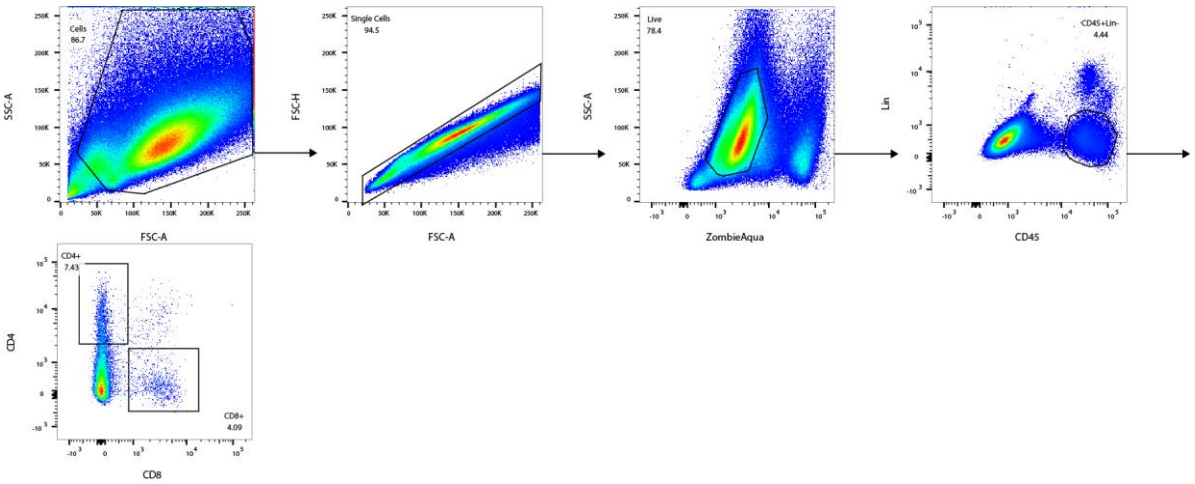

Figure 17. Gating strategy of TILs in PD-1 mAbs treated YUMM1.7 tumour-bearing $GR^{f/fLysMcre}$ mice.
T cells were gated as CD45.2+ Lin-(CD19, NK1.1, Ly6G, SiglecF) CD4- CD8+ cells or CD45.2+ Lin-(CD19, NK1.1, Ly6G, SiglecF) CD8- CD4+ cells.

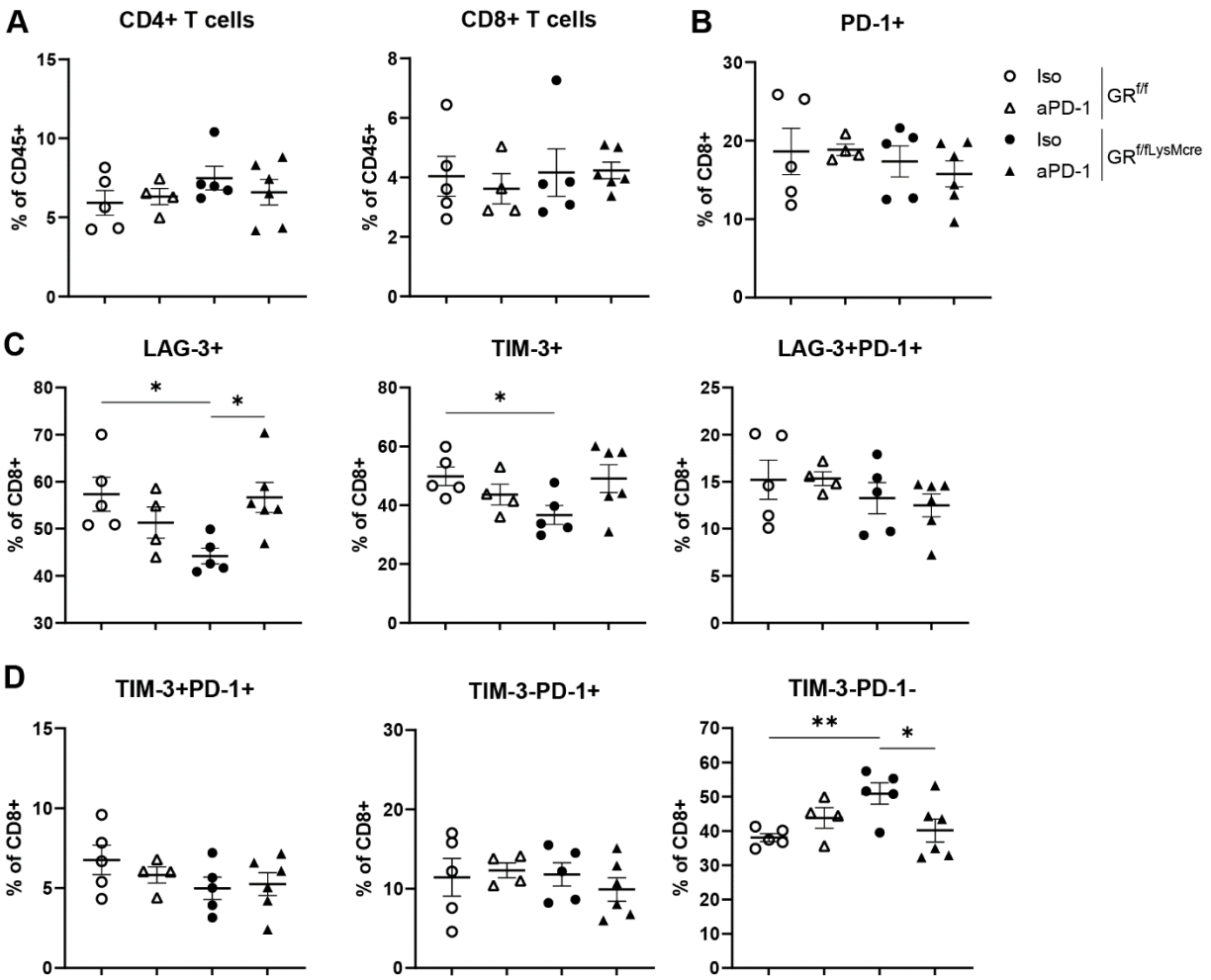

Figure 18. Characterization of TILs in PD-1 mAbs treated YUMM1.7 tumour-bearing GR$^{f/fLysMcre}$ mice.
aPD-1 or isotype (Iso) treated GR$^{f/f}$ wild type or GR$^{f/fLysMcre}$ transgenic mice were analysed by flow cytometry. **(A)** Frequency of CD4+ and CD8+ T cells. **(B)** Frequency of CD8+ PD-1+ T cells. **(C)** Expression of LAG-3, TIM-3 and co-expression of LAG-3 and PD-1 by CD8+ T cells. **(D)** Co-expression of TIM-3 and PD-1 by CD8+ T cells. Data are represented as mean ± SEM of n=4-5. Statistically significant differences were calculated using an Unpaired t test. *, $P < 0.05$; **, $P < 0.01$.

5.5 Macrophages are polarized towards an immunosuppressive phenotype by GCs

In the setting of cancer, monocytes are recruited from the circulation into solid tumours and differentiate to TAMs. Endogenous, tumour-derived GCs and GR signalling in the TME is a tumour intrinsic mechanism of immunosuppression (Acharya, Madi et al. 2020, Deng, Xia et al. 2021, Melo, Herrera-Rios et al. 2023), potentially promoting a pro-tumour M2-like phenotype in TAMs.

5.5.1 Generation of TAM-like BMDM *in vitro* by GR activation

Bone marrow-derived macrophages (BMDM) were generated by culturing bone marrow cells in the presence of macrophage colony-stimulating factor (M-CSF) for six days. To examine the effect of tumour-derived GCs on macrophage polarization, BMDM were stimulated with the GR agonist dexamethasone (DEX) alone or in combination with YUMM1.7 tumour cell conditioned medium (TCM) and IL-4 as an *in vitro* surrogate for the TME.

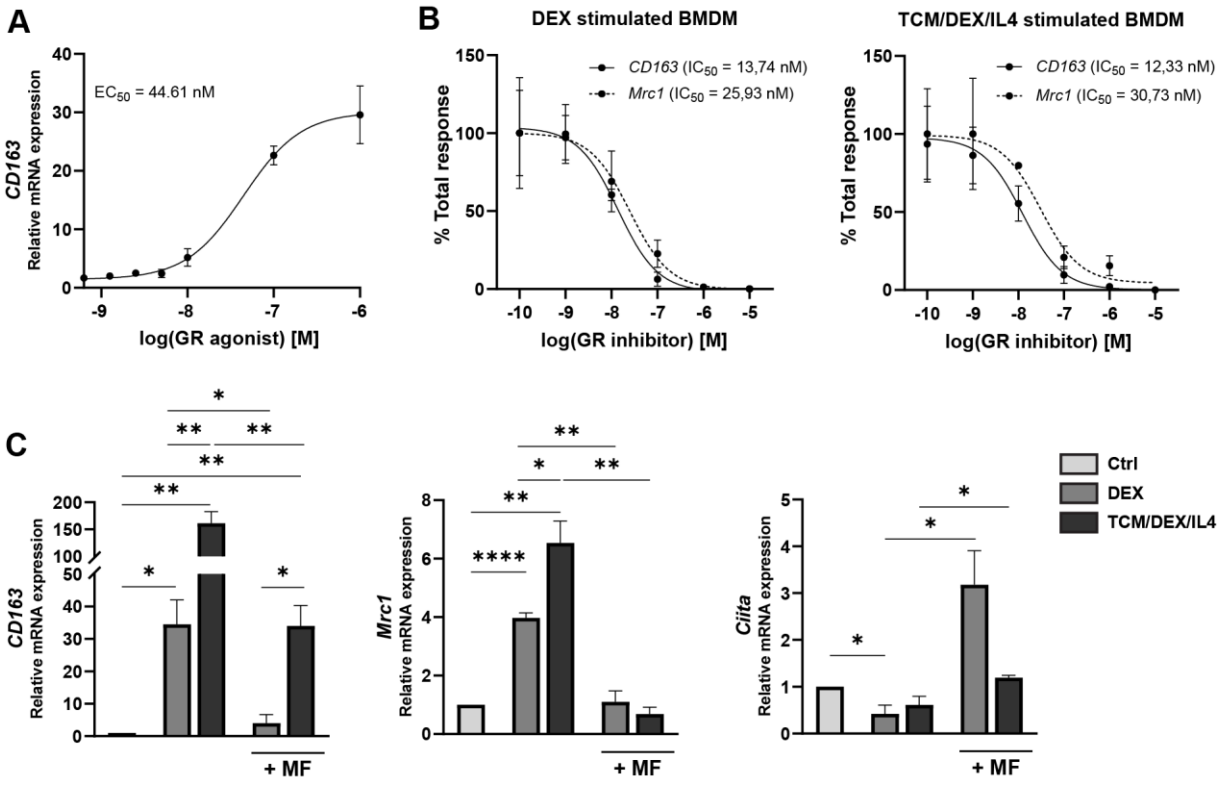

Figure 19. GR inhibition blocks polarization towards an immunosuppressive phenotype in BMDM.
(A) Dose titration of the GR agonist dexamethasone (DEX) in BMDM. EC_{50} value determined by nonlinear regression. **(B)** Dose response curve of the GR inhibitor mifepristone (MF) in DEX vs. TCM/DEX/IL4 stimulated BMDM normalized to BMDM stimulated with DEX or TCM/DEX/IL4 without inhibitor (100%). IC_{50} values determined by nonlinear regression. **(C)** Relative expression of *CD163*, *Mrc1*, and *Ciita* in DEX vs. TCM/DEX/IL4 stimulated BMDM ± MF. Data are represented as mean ± SEM of n=3. Statistically significant differences were calculated using an Unpaired t test. *, P < 0.05; **, P < 0.01; ****, P < 0.0001.

DEX strongly induced the expression of the M2 related marker *CD163* by BMDM in a dose-dependent manner and EC_{50} of 44.61 nM (**Figure 19. A**). GCs are the most potent stimulators of CD163 expression and the GC-mediated regulation of CD163 is also evidenced by the identification of three GR-binding sites in the promoter region of the CD163 gene (Etzerodt and Moestrup 2013). In human cancers, the expression of CD163 by TAMs has been shown to be a particularly strong indicator of poor prognosis melanoma (Jensen, Schmidt et al. 2009, Bronkhorst, Ly et al. 2011, Lee, Lee et al. 2019). In line with this, expression of the M2 phenotypic marker mannose receptor C-type 1 (*Mrc1*/CD206) was upregulated, while the M1 phenotypic marker class II major histocompatibility complex transactivator (*Ciita*), the master regulator of MHC class II gene transcription, was downregulated upon stimulation with 100 nM DEX (**Figure 19. C**). Compared to BMDM treated with DEX alone, the stimulation with TCM/DEX/IL4 resulted in a much stronger upregulation of *CD163* and *Mrc1*. This suggests that additional tumour-derived factors found in media conditioned from YUMM1.7 tumour cells increased BMDM sensitivity to DEX, resulting in an immunosuppressive M2-like phenotype resembling that of TAMs *in vivo*.

5.5.2 Mifepristone (RU-486) inhibits activation of the GR signalling pathway

To block GR mediated induction of an immunosuppressive phenotype, BMDM were incubated with the small molecule GR inhibitor mifepristone (MF, RU-486) prior to stimulation with DEX or TCM/DEX/IL4. MF decreased the DEX and TCM/DEX/IL4 induced expression of *CD163* (IC_{50} of 13.74 nM and 12.33 nM) and *Mrc1* (IC_{50} of 25.93 nM and 30.37 nM) in a dose-dependent manner (**Figure 19. B**), and showed strong inhibitory effects at 100 nM on both genes, reducing *Mrc1* expression to baseline levels. Next, it was tested whether MF, in addition to inhibiting anti-inflammatory genes, could also upregulate pro-inflammatory genes. Notably, MF not only blocked the DEX and TCM/DEX/IL4 induced reduction of *Ciita*, but also increased its expression (**Figure 19. C**). The results show that macrophages were polarized from a M2 phenotype to an anti-tumour M1-like phenotype by inhibiting GR signalling.

5.5.3 GR-mediated inhibition of pro-inflammatory mediator release

IL-12 is a pro-inflammatory cytokine produced by activated antigen-presenting cells (APCs) that promotes anti-tumour immunity by inducing proliferation and lytic function of NK cells and CD8+ T-lymphocytes, promoting TH1 cell differentiation, and enhancing IFNγ production by T and NK cells. Activation of T cells in the presence of IL-12 also reduces negative regulatory mechanisms

such as PD-1/PD-L1 signalling, augmenting the efficacy of aPD-1 checkpoint immunotherapy in preclinical models (Garris, Arlauckas et al. 2018).

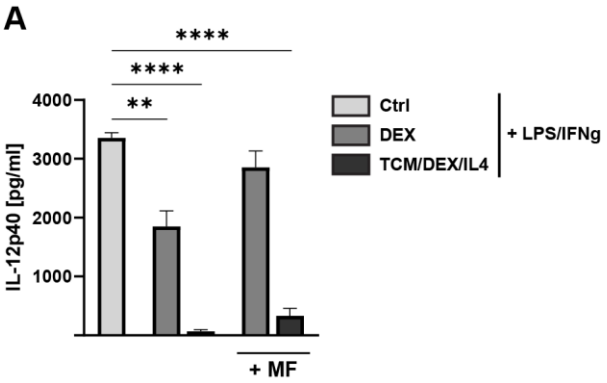

Figure 20. DEX and TCM/DEX/IL4 selectively inhibit IL-12 production by BMDM.
(A) BMDM were treated with DEX or TCM/DEX/IL4 ± MF for 1 h after which LPS/IFNγ was added for 24 h. Cell culture supernatants were collected and cytokine production was analysed by ELISA. Data are represented as mean ± SEM of n=3. Statistically significant differences were calculated using an Unpaired t test. *, P < 0.05; ****, P < 0.0001.

Therefore, it was tested if the inhibitory effects of GCs also applied to IL-12 production. BMDM were treated with DEX or TCM/DEX/IL4 for 1 h after which LPS/IFNγ was added to stimulate IL-12 secretion (**Figure 20**). LPS/IFNγ induced IL-12 production was strongly impaired in the presence of DEX, although this antagonizing effect was not complete, and failed to induce its production in TCM/DEX/IL4 stimulated BMDM, with IL-12p40 levels 1.8-fold lower in DEX treated and 50-fold lower in TCM/DEX/IL4 treated BMDM. MF showed a tendency to abrogate the inhibition of IL-12 by DEX, but not by TCM/DEX/IL4, indicating that this suppression was mainly GR-mediated. These data show that GCs not only induce an immunosuppressive phenotype, but also repress pro-inflammatory activation of macrophages.

5.6 The positive feed-forward mechanism of GCs and 11β-HSD1

5.6.1 GR activation induces high expression of *HSD11B1* in BMDM

High expression of *HSD11B1* predominantly by TAMs is associated with poor response to checkpoint immunotherapy in patients with melanoma (Melo, Herrera-Rios et al. 2023). Previous reports have indicated that in certain cell types, GCs act in an autocrine manner, stimulating the expression of 11β-HSD1, the enzyme catalysing the reduction of glucocorticoids from their inactive (11-dehydrocorticosterone, cortisone) to their active forms (corticosterone, cortisol), known as a positive feed-forward mechanism (Sun, He et al. 2002, Inder, Obeyesekere et al. 2012) (**Figure 21. A,**

B). To investigate, if 11β-HSD1 can be detected and induced in macrophages, BMDM were stimulated with increasing concentrations of DEX. Low concentrations of DEX had no effect on *HSD11B1* expression in BMDM, however, at concentrations above 100 nM (10^{-7} M), DEX was able to induce *HSD11B1* gene expression (**Figure 21. C**), while TCM/DEX/IL4 stimulation resulted in a several-fold higher *HSD11B1* expression compared to stimulation with DEX alone. MF efficiently abrogated the induction of *HSD11B1* for both stimulations, confirming GR-driven upregulation of *HSD11B1* expression (**Figure 21. B**). In contrast, DEX did not affect the expression of *Nr3c1* (**Figure 21. C**), the gene encoding for GR.

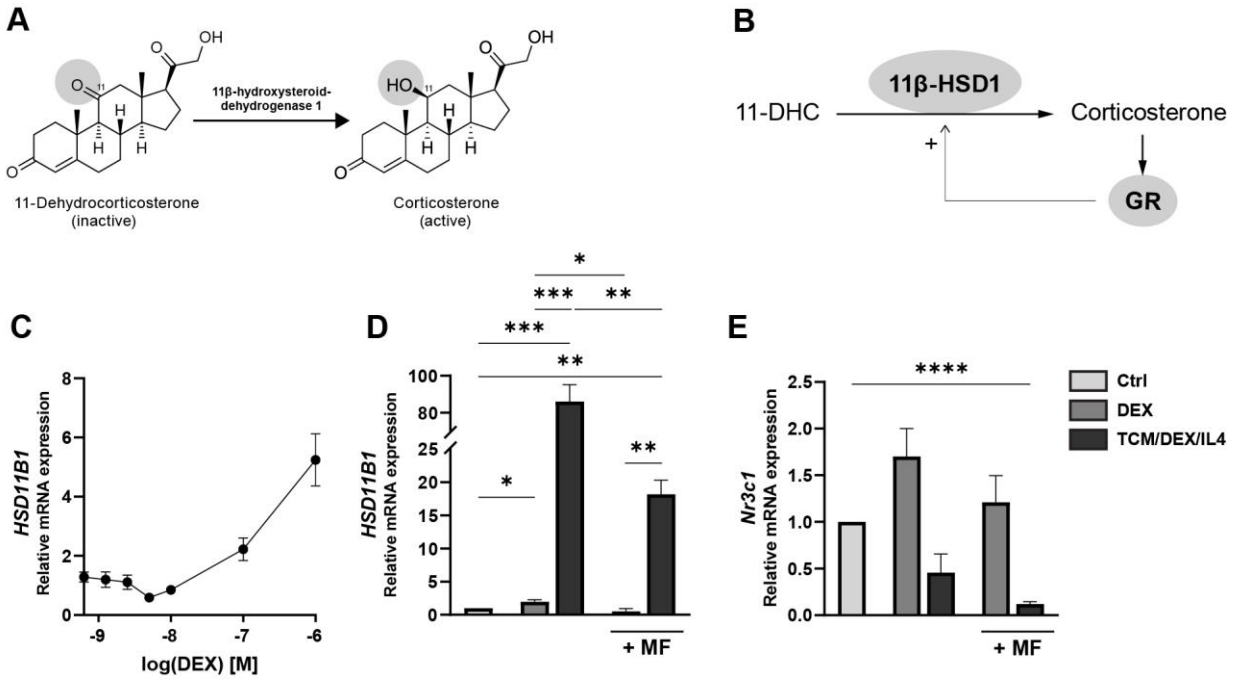

Figure 21. Upregulation of *HSD11B1* in BMDM upon GR activation.
(A) The interconversion of inactive 11-dehydrocorticosterone (11-DHC) to its active form corticosterone is catalysed by the enzyme 11β-hydroxysteroid dehydrogenase 1 (11β-HSD1, encoded by *HSD11B1*). **(B)** Schematic representation of the regulation of local GC levels by intracellular 11β-HSD1. 11β-HSD1 catalyses the regeneration of active GCs (cortisol, corticosterone), thus amplifying GC levels and its cellular action. GCs themselves increase 11β-HSD1 expression in an autocrine manner. **(C)** Relative expression of *HSD11B1* in BMDM stimulated with increasing concentrations of DEX. **(D)** Relative expression of *HSD11B1* and **(E)** *Nr3c1* in DEX (100 nM) vs. TCM/DEX/IL4 stimulated BMDM ± MF. Data are represented as mean ± SEM of n=3. Statistically significant differences were calculated using an Unpaired t test. *, P < 0.05; **, P < 0.01; ***, P < 0.001; ****, P < 0.0001.

To validate the function of GR-driven *HSD11B1* upregulation, BMDM were stimulated with DEX or TCM/DEX/IL4 for 24 h after which cells were washed to remove residual stimulants and incubated with 11-DHC for 3 h. Subsequently, conversion of 11-DHC to corticosterone by 11β-HSD1 was measured in the supernatants. Stimulation of BMDM with DEX alone did not increase 11β-

HSD1 activity compared to unstimulated BMDM (Ctrl), however, after stimulation with TCM/DEX/IL4 strong increase in 11β-HSD1 activity was observed (**Figure 22. A**). Notably, basal corticosterone levels were detected in supernatants from unstimulated BMDM and in cell free growth medium containing 10% FBS or 10% FBS/50% TCM (**Figure 22. B**). In line with earlier data, MF efficiently abrogated 11β-HSD1 activity, confirming GR-driven increase of 11β-HSD1 activity. This efficient mechanism by which GR-activated TAM-like BMDM generate corticosterone in an autocrine fashion will help to understand the complex effects of GCs on the TME.

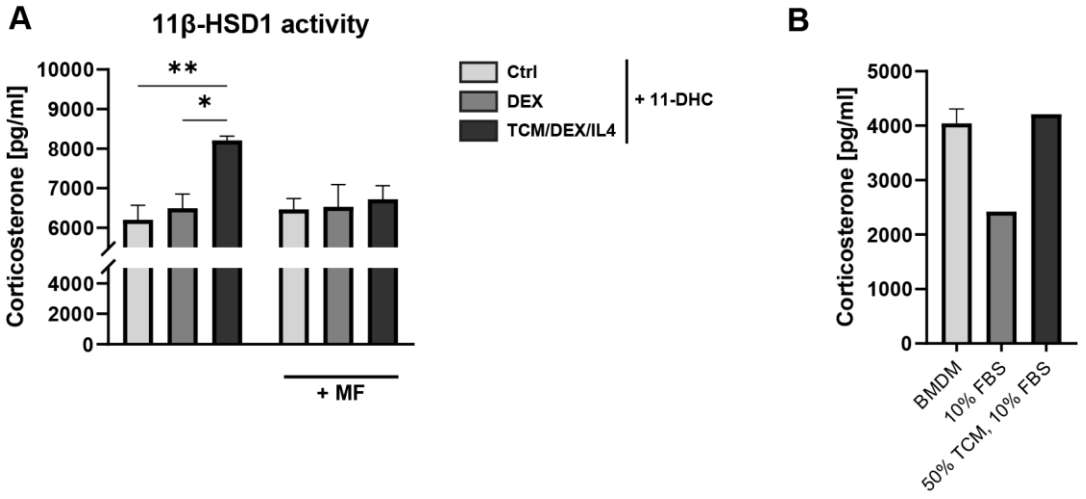

Figure 22. Conversion of 11-DHC to corticosterone by 11β-HSD1 in TAM-like BMDM.
(A) BMDM were treated with DEX or TCM/DEX/IL4 ± MF for 24 h after which cells were washed three times and incubated with growth medium containing 100 nM 11-DHC ± MF for 3 h. Formation of corticosterone was determined in the supernatants by ELISA. Data are represented as mean ± SEM of n=3. Statistically significant differences were calculated using an Unpaired t test. *, $P < 0.05$; **, $P < 0.01$. **(B)** Corticosterone levels in supernatants from unstimulated BMDM (Mean ± SEM of n=3) and in cell free medium containing 10% FBS (n=1) or 10% FBS/50% TCM (n=1).

5.6.2 *HSD11B1* is upregulated in tumours that fail to respond to aPD-1 checkpoint immunotherapy

To determine the implication of GR-driven upregulation of *HSD11B1* on the response to checkpoint immunotherapy *in vivo*, the expression of steroidogenesis pathway enzymes was analysed in murine tumour tissue. Expression of *Cyp11A1*, the first and rate-limiting enzyme of steroid biosynthesis, as well as *HSD11B1*, was identified in YUMM1.7 tumour tissue, indicating steroidogenic potential and local GC activation (**Figure 23. A, B**). In line with this, corticosterone, the main active 11-hydroxy steroid in rodents (cortisol in humans), was detected at high levels in supernatants from *ex vivo* cultured YUMM1.7 tumour explants (**Figure 24. A**), confirming the presence of local de novo steroidogenesis in the tumour. Notably, YUMM1.7 melanoma cells produce only low levels of corticosterone *in vitro*, indicating that the production of GCs is an *in vivo* acquired

mechanism or de novo steroid biosynthesis occurs in a different cell type than tumour cells. *HSD11B1* was detected in tumours from all treatment groups, however, strong upregulation was observed upon aPD-1 treatment in mice that fail to respond to aPD-1 treatment (aPD-1/GR$^{f/f}$), indicating high GC activation in the treatment group. This suggests an inhibitory mechanism of anti-tumour immune responses induced upon aPD-1 checkpoint immunotherapy. Notably, this effect was abrogated in the absence of TAM-expressed GR with lower expression of *HSD11B1*, thus lower GC activation, in tumours from GR$^{f/fLysMcre}$ transgenic mice that respond to aPD-1 checkpoint immunotherapy. *Cyp11A1* expression was detected in all treatment groups, however, an upregulation upon aPD-1 checkpoint immunotherapy was not detected, indicating that aPD-1 resistant YUMM1.7 tumours produce GCs by metabolite recycling, rather than de novo synthesis.

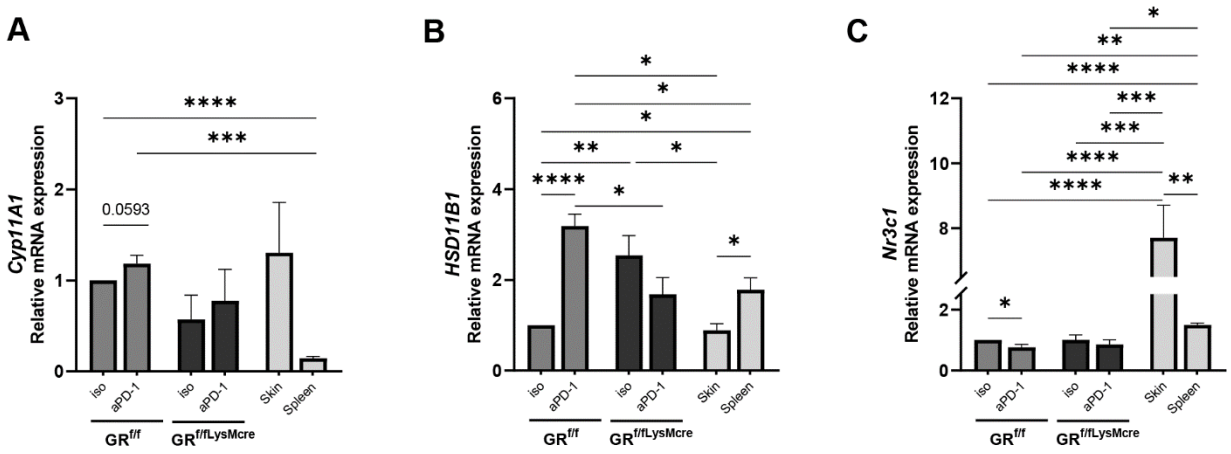

Figure 23. Expression of steroidogenic enzymes in tumour tissue.
(A) Relative expression of *Cyp11A1*, **(B)** *HSD11B1* and **(C)** *Nr3c1* in YUMM1.7 tumour tissue from aPD-1 or isotype (iso) treated GR$^{f/fLysMcre}$ transgenic or GR$^{f/f}$ wild type mice. Data are represented as mean ± SEM of n=3-5. Statistically significant differences were calculated using an Unpaired t test. *, P < 0.05; **, P < 0.01; ***, P < 0.001; ****, P < 0.0001.

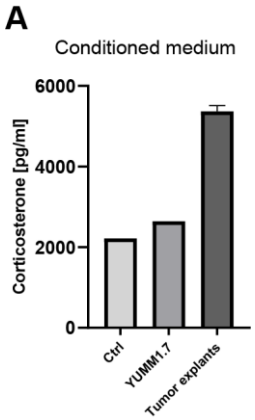

Figure 24. Local production of corticosterone in the TME.
(A) Corticosterone levels in media conditioned from *in vitro* cultured YUMM1.7 cells and *ex vivo* isolated YUMM1.7 tumour explants measured by ELISA.

5.6.3 *HSD11B1* expression in human melanomas

HSD11B1 expression in human melanomas is associates with clinical response to checkpoint immunotherapy (Melo, Herrera-Rios et al. 2023). Previous data from stimulating BMDM with DEX or TCM/DEX/IL4 has shown a polarization towards an immunosuppressive phenotype, evidenced by the upregulation of immunosuppressive markers (*Mrc1*, *CD163*) (**Figure 19**) and a strong capacity to inhibit T cell proliferation (**Figure 26**). Notably, this polarization correlated with an increased expression and elevated activity of 11β-HSD1 (**Figure 21**, **Figure 22**). To investigate the translational relevance of these findings, human skin cutaneous melanoma (SKCM) TCGA datasets were analysed using the Gene Expression Profiling Interactive Analysis (GEPIA) tool.

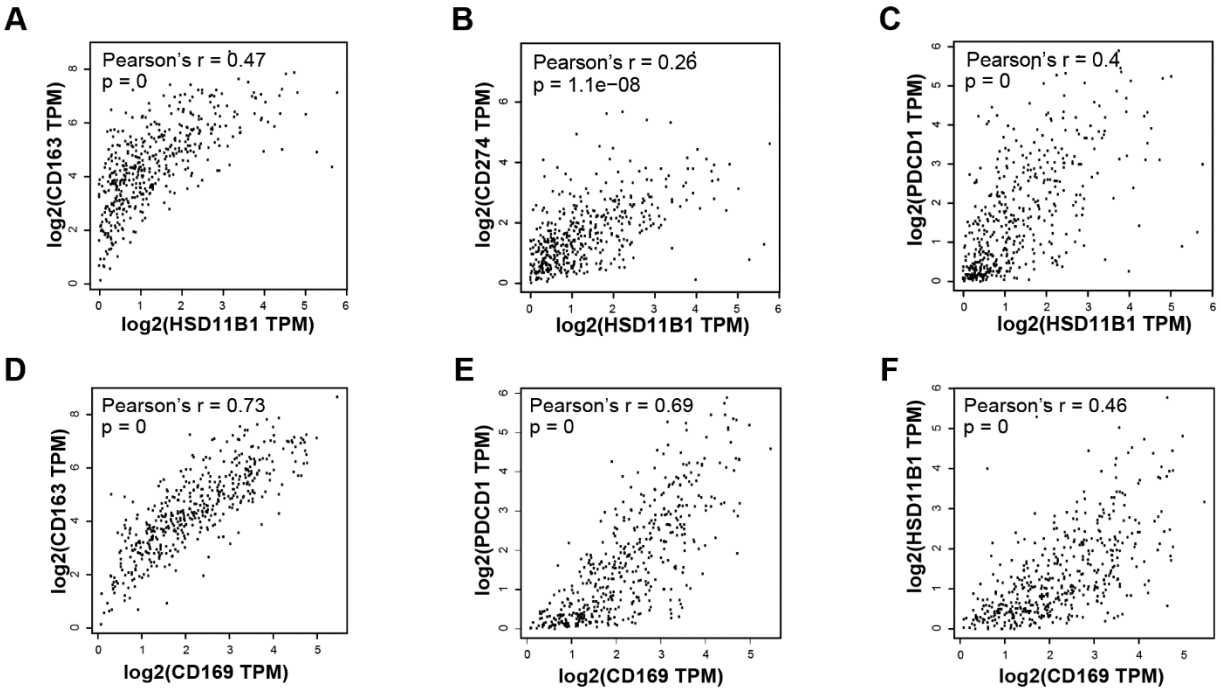

Figure 25. Correlation analysis of human SKCM TCGA datasets using the GEPIA tool.
(A) *HSD11B1* and *CD163* were positively correlated (p=0; r=0.47). **(B)** *HSD11B1* and *CD274* were positively correlated (p=1.1e-08; r=0.26). **(C)** *HSD11B1* and *PDCD1* were positively correlated (p=0; r=0.4). **(C)** *CD169* and *CD163* were positively correlated (p=0; r=0.73). **(D)** *CD169* and *PDCD1* were positively correlated (p=0; r=0.69). **(E)** *CD169* and *HSD11B1* were positively correlated (p=0; r=0.46). GEPIA uses the non-log scale for calculation and the log-scale axis for visualization.

HSD11B1 expression positively correlated with the expression of *CD163*, *CD274,* and *PDCD1* (**Figure 25. A, B, C**). *CD169* positively correlated with *CD163*, *PDCD1* and *HSD11B1* (**Figure 25. D, E, F**). In clinical data, the expression of CD163 by TAMs strongly correlates with poor prognosis in a range of cancers, including melanoma (Jensen, Schmidt et al. 2009). Recently, it was found that tumour cells have the capacity to induce CD169 expression in monocyte-derived TAMs, which was found to be associated with poor survival in patients (Cassetta, Fragkogianni et al.

2019). PD-1 is a T cell checkpoint receptor that, upon engagement by its ligands PD-L1 (B7-H1) or PD-L2 (B7-DC), inhibits T cell effector functions by inhibiting signalling downstream of the T cell receptor (TCR) (Topalian, Drake et al. 2012). Thus, expression of PD-1 ligands, and particularly PD-L1, in the TME promote immune evasion. PD-L1 expression by TAMs negatively regulates and inhibits T cell activation, reducing the efficacy of aPD-1 checkpoint immunotherapy (Tang, Liang et al. 2018). Together these data suggest a translational relevance of the previously described data.

5.7 Capacity of GR-activated TAM-like BMDM in inhibiting T cell proliferation

Immunosuppressive TAMs inhibit T cell–mediated anti-tumour immunity, decreasing the efficiency of aPD-1 checkpoint immunotherapy. To functionally validate the capacity of GR-activated TAMs to inhibit T cell proliferation, CFSE-stained splenic CD8+ T cells were activated with anti-CD3/anti-CD28 antibodies and co-cultured with DEX- or TCM/DEX/IL4-stimulated BMDM for 72 h (**Figure 26. A, B**).

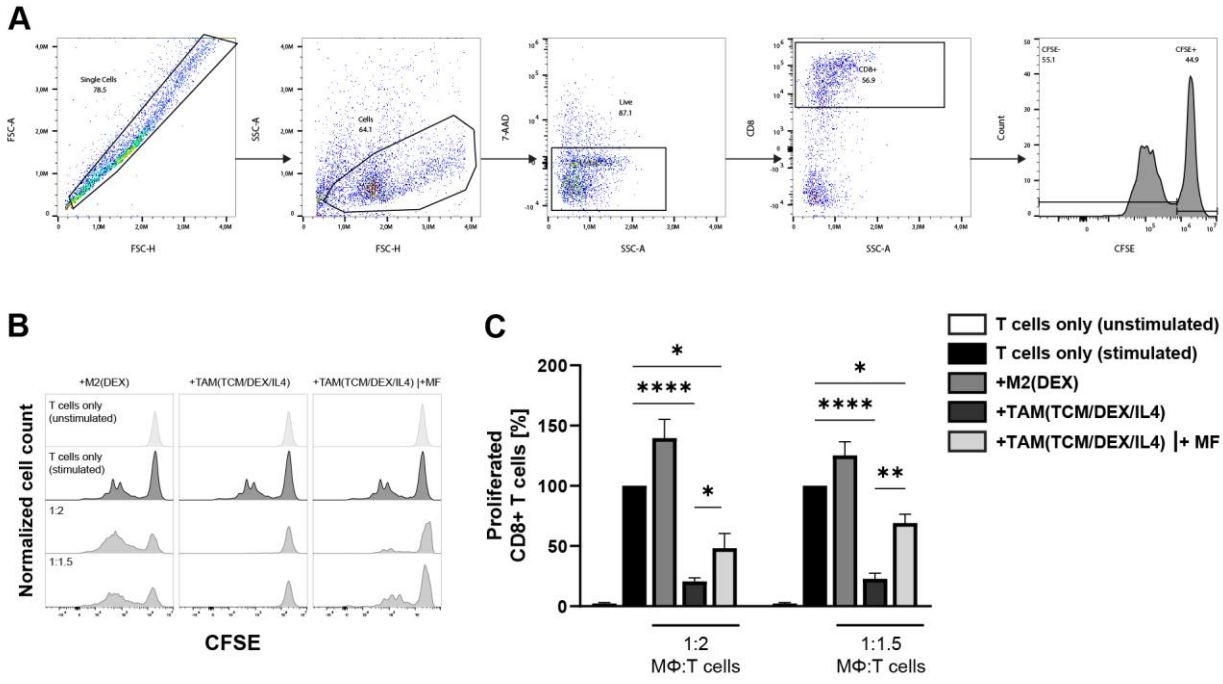

Figure 26. Suppression of T cell proliferation by TAM-like BMDM.
CFSE labelled splenic CD8+ T cells purified from healthy C57BL/6J mice were activated with plate-bound anti-CD3/anti-CD28 antibodies and co-cultured with DEX (M2(DEX)) or TCM/DEX/IL4 (TAM(TCM/DEX/IL4)) ± MF stimulated BMDM. Dilution of CFSE staining in proliferated CD8+ T cells was assessed by flow cytometry after 72 h of co-culture. **(A)** Representative data of CD8+ T cell gating (M2(DEX):T cells co-culture (1:1.5) is shown) and **(B)** CFSE staining after co-culture (cell ratios as indicated). **(C)** Quantification of proliferated CD8+ T cells. Data are represented as mean ±

SEM of n=3-6. Statistically significant differences were calculated using an Unpaired t test. *, P < 0.05; **, P < 0.01; ****, P < 0.0001.

As expected, most of the T cells proliferated after stimulation with anti-CD3/anti-CD28 antibodies when cultured alone. While DEX-stimulated BMDM were not capable of suppressing T cell proliferation in the tested M2(DEX):T cells ratios 1:2 and 1:1.5, TCM/DEX/IL4-stimulated BMDM strongly inhibited T cell proliferation in both tested cell ratios. Notably this effect was abrogated in the presence of the GR inhibitor MF, demonstrating its direct effect on inhibiting immunosuppressive functions of TAM-like BMDM (**Figure 26. C**). The data are in line with earlier shown data of enhanced *Ciita* expression upon MF treatment in BMDM and MHC-II increase in GR-deficient TAMs *in vivo*. Altogether, these findings emphasize the therapeutic potential of targeting GR in TAMs to sensitize melanoma to checkpoint immunotherapy.

5.8 Functionalized nanoparticles targeting TAMs as cancer therapy

5.8.1 Production and characterization of MF-loaded LNPs

Lipid nanoparticles (LNPs) were used as drug delivery systems for MF due to their ability to improve the pharmacokinetic properties of lipophilic drugs (calculated logP(MF) 6.193 ± 0.552, SciFinder) by solubilizing them within the lipid core, and their potential for active targeting through antibody conjugation. MF-loaded LNPs, consisting of triglyceride cores surrounded by a POPC monolayer, were developed as previously described (Zhigaltsev, Belliveau et al. 2012). PEGylated lipids (mPEG2000-DPSE) were incorporated to shield the surface from aggregation, opsonisation, and non-specific phagocytosis by macrophages and other cell types. DSPE-PEG5000-DBCO was introduced for antibody coupling via post-insertion. LNPs were formulated by rapid mixing of lipids dissolved in ethanol with an aqueous stream using a microfluidic staggered herringbone micromixer (SHMs). This method induces rapid mixing by chaotic advection of the laminar streams leading to rapid increase in the polarity of the two phases. At a critical polarity lipid precipitates form as LNPs, having the smallest possible stable structure compatible with the molecular composition.

5.8.2 Influence of flow rate ratio and total flow rate on the limit size of LNPs

First, it was investigated whether controlling the size of LNPs obtained with this method was possible. As the formation of LNPs is driven by the rate of increase in polarity, the effect of varying the flow rate ratio (FRR) between the lipid mix and the aqueous solution, as well as the total flow

rate (TFR) – the speed at which the fluid is run through the chip of the microfluidic mixer – on the particle size was determined. FRRs of 1:2, 1:4, and 1:8 were employed by maintaining a constant flow rate of 5 ml/min in the ethanolic channel while increasing the flow rates of the aqueous channel. Additionally, the TFR was varied as indicated. Results obtained from both dynamic light scattering (DLS) and nanoparticle tracking analysis (NTA) measurements of the obtained formulations showed a decrease in particle size when the FRR was increased. Similarly, an increase in the TFR also resulted in a decreased particle size (**Figure 27. A, B**).

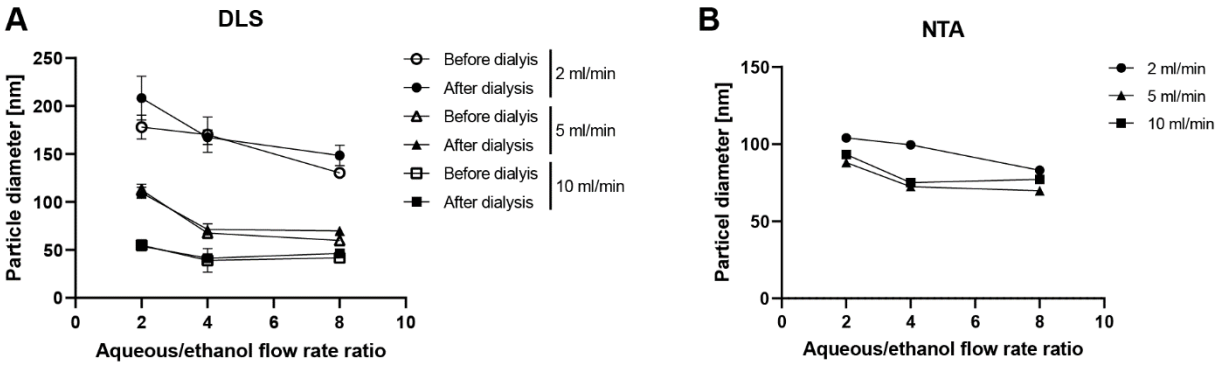

Figure 27. Effect of FRR and TFR on the limit size of LNPs.
LNPs were produced by microfluidic mixing from POPC/triolein/DSPE-mPEG2000 (55/40/5; %mol). **(A)** Size measurements obtained using DLS. Data are represented as mean ± SD of 10 measurements, repeated twice. **(B)** NTA measurement of LNPs after dialysis. Data are represented as mean ± SD of 5 captures, repeated twice.

The variation in LNP size measurements between DLS and NTA can be attributed to intrinsic differences between these two techniques. DLS determines particle size by analysing fluctuations in scattered light intensity caused by the Brownian motion of particles in the liquid medium. DLS is sensitive to the presence of larger particles, as the intensity of scattered light is proportional to the sixth power of the particle diameter. This sensitivity to larger particles can lead to an overrepresentation of their contribution in the size distribution. NTA tracks individual nanoparticles undergoing Brownian motion and relates their movement to particle size. NTA provides a number-weighted distribution of particle sizes, which is different from the intensity-weighted distribution obtained by DLS. Due to these differences in weighting the size distribution, DLS and NTA may yield slightly different results when measuring the size of LNPs in the same sample. However, since both techniques use similar physical characteristics to determine particle size, they can serve as complementary methods to verify each other's results. Limitations of NTA measurements lie in its detection threshold, which is approximately 40-50 nm in diameter. Consequently, when

employing a TFR of 10 ml/min, the population of particles generated included some that exceed the detection limit, leading to a skewing effect on the mean particle size measured in the solution.

Table 1. Polydispersity of LNP formulations at different TFR and FRR.
Data from DLS measurements of LNP formulations (POPC/triolein/DSPE-mPEG2000; 55/40/5; mol%) are represented as mean ± SD of 10 measurements, repeated twice. Percent polydispersity (%PD), polydispersity normalized to the mean size of the peak.

TFR	FRR	Before Dialysis		After Dialysis	
		%PD	SD	%PD	SD
2 ml/min	1:2	18.4	5.1	12.1	6.6
	1:4	21.4	2.7	20.9	4.3
	1:8	20.8	3.5	23.4	8.9
5 ml/min	1:2	23.0	2.3	19.5	3.2
	1:4	26.5	7.5	24.8	7.8
	1:8	25.0	3.1	28.0	9.7
10 ml/min	1:2	Multimod./35.8	13.3	Multimod./31.0	12.7
	1:4	Multimod./55.0	5.5	Multimod./33.8	10.6
	1:8	Mulitmod./41.3	15.1	Multimod./36.1	13.0

At TFRs of 5 ml/min and 2 ml/min, a uniform size distribution was observed, while at 10 ml/min, the homogeneity was found to be low, with percent polydispersity (%PD) exceeding 30% (**Table 1**). Dialysis had no relevant impact on particle size or polydispersity. For subsequent experiments, a TFR of 5 ml/min and FRR of 1:4 were selected as parameters, as the resulting formulations were characterized by low polydispersity and higher LNP concentration.

The data demonstrate that controlling the size of LNPs can be achieved through adjustments to the FRR and TFR during the microfluidic mixing process. This is attributed to the enhanced rate of mixing between the aqueous and ethanol streams at higher FRR and higher TFR, leading to a faster increase in solvent polarity.

5.8.3 Influence of the lipid composition on the limit size of LNPs

As indicated above, LNPs were composed of a lipid monolayer surrounding a hydrophobic core, with the membrane lipid consisting of POPC and the stealth-lipid mPEG2000-DPSE, while the core lipid was triolein. To evaluate the effect of the lipid composition on the limit size of LNPs, varying ratios of membrane/core lipid (40/60, 60/40, and 80/20 mol%; mPEG2000-DSPE fixed at 5 mol%) were tested. The results demonstrate that increasing the membrane/core lipid ratio led to the formation of smaller lipid nanoparticles (**Figure 28. A**), due to the increase in surface area to volume ratio with decreasing particle size.

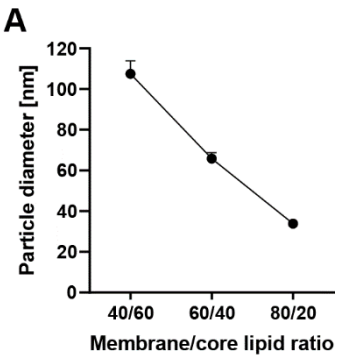

Figure 28. Effect of lipid composition on the limit size of LNPs.
LNPs were produced by microfluidic mixing from different membrane/core lipid ratios (mol/mol) at 5 ml/min TFR and 1:4 FRR. **(A)** Size measurements obtained using DLS. Data are represented as mean ± SD of 10 measurements, repeated twice.

Uniform size distribution was observed for all formulations with a tendency to higher polydispersity when particle size increased (**Table 2**). For subsequent experiments, a membrane/core lipid ratio of 60/40 mol% was selected.

Table 2. Polydispersity of LNP formulations from different lipid ratios.
Data from DLS measurements of LNP formulations (5 ml/min TFR; 1:4 FRR) are represented as mean ± SD of 10 measurements, repeated twice. Percent polydispersity (%PD), polydispersity normalized to the mean size of the peak.

Membrane/core lipid ratio	%PD	SD
40/60	19.2	3.7
60/40	22.2	1.8
80/20	24.4	10.8

In summary, the diameter of LNPs could be rationally engineered within a range of 30-200 nm. This was achieved by adjusting TFR and FRR during the microfluidic mixing process, along with modulation of the membrane/core lipid ratio. Notably, the LNP size remained consistent and reproducible across different experiments, highlighting the reliability of the manufacturing process.

5.8.4 MF can be efficiently loaded into limit size LNPs

Next, it was investigated whether MF could be loaded and retained in these LNPs. A commonly used technique for loading LNPs with poorly water-soluble drugs is to dissolve the drug in the ethanolic lipid mix prior to particle formation. Varying amounts of MF corresponding to drug-to-lipid ratios of 0.05, 0.1, 0.15, and 0.2 (mol/mol) were added to the POPC/triolein/DSPE-mPEG2000 (55/40/5; %mol) lipid mix and LNPs were prepared at 1:4 FRR and 5 ml/min TFR.

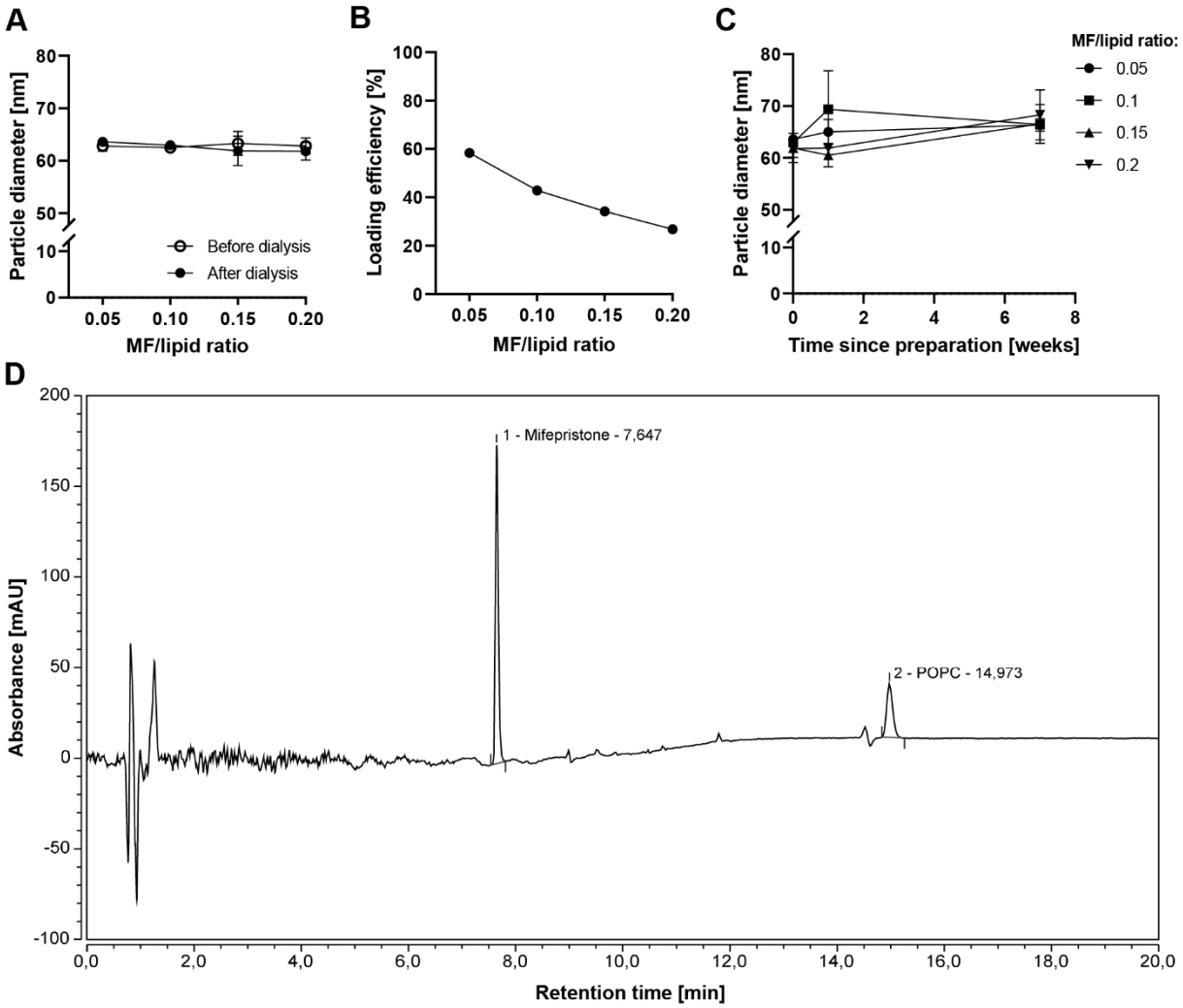

Figure 29. LNP formulations encapsulating MF.
LNPs were produced by microfluidic mixing from POPC/triolein/DSPE-mPEG2000 (55/40/5; %mol) at 5 ml/min TFR and 1:4 FRR. MF was dissolved in EtOH at 20 mg/ml and added to the lipid mix to give a drug-to-lipid ratio of 0.05, 0.1, 0.15, and 0.2 (mol/mol). **(A)** Size measurements of MF-loaded LNPs obtained using DLS. Data are represented as mean ± SD of 10 measurements, repeated twice. **(B)** Loading efficiencies were determined by quantitating both MF and lipid levels by HPLC after removing external drug from LNP encapsulated drug and comparing the respective amount to the amount applied to the nanoparticle formulation (100%). **(C)** Stability of MF-loaded LNPs over time measured by DLS. Data are represented as mean ± SD of 10 measurements, repeated twice. **(D)** Representative HPLC-UV chromatogram of MF-loaded LNPs. Separation was achieved by reversed-phase (RP) HPLC using a Nucleodur RP-18 column (100 x 4 mm, analytical) and a gradient of MeOH:water (0.9% TFA) (0–10 min: 10–99% MeOH), 1 ml/min. MF t_R=7.645 min, λ_{max}=300 nm; POPC t_R=14.973 min, λ_{max}=205 nm. The concentration of MF and POPC in the LNP formulations was determined using a calibration curve of peak area versus concentration, and total lipid content was calculated based on the POPC measurements.

The particle sizes in the MF-containing LNPs were comparable to those of the corresponding drug-free LNPs (**Figure 29. A**), and %PD was below 30%, indicating a narrow size distribution (**Table 3**). Drug loading was confirmed by reversed phase high performance liquid chromatography (RP-HPLC) with UV-spectrophotometrical detection at 300 nm. Loading efficiency, defined as the ratio of the amount of drug incorporated in nanoparticles to the amount of drug applied in

formulation of the nanoparticles, was 57.7% for 0.05 MF/lipid ratio and higher levels of available drug resulted in reduced loading efficiency.

Drug-loaded dispersions can sometimes exhibit poor storage stability, leading to the formation of crystals enriched in phase-separated drug and changes in particle size or size distribution. Therefore, the impact of drug content on long-term stability of the lipid LNPs was investigated. The particle size of LNPs remained within a limited size range during storage, with no increase in the particle size distribution. Moreover, no detectable drug release was observed over the 45-day storage period at 4°C. For subsequent experiments, 0.05 MF/lipid ratio was selected.

Table 3. Polydispersity of LNP formulations encapsulating MF.
Data from DLS measurements of LNP formulations (POPC/triolein/DSPE-mPEG2000 (55/40/5; %mol), 5 ml/min TFR; 1:4 FRR) are represented as mean ± SD of 10 measurements, repeated twice. Percent polydispersity (%PD), polydispersity normalized to the mean size of the peak.

MF/lipid ratio	Day 1		Day 7		Day 45	
	%PD	SD	%PD	SD	%PD	SD
0.05	20.7	2.6	22.1	1.8	21.7	5.4
0.1	20.7	2.8	25.4	9.5	24.1	4.2
0.15	22.0	2.2	20.8	2.7	23.9	8.2
0.2	20.4	3.5	22.8	1.1	22.4	5.0

5.8.5 Modification of MF-loaded LNPs for CD169 targeting

MF-loaded LNPs were targeted to the MΦ-specific endocytotic scavenger receptor CD169, also known as Siglec1 or Sialoadhesin (Sn), using an anti-CD169 monoclonal antibody in order to investigate the specific uptake and effect of MF on MΦ. Specifically targeting LNPs improves drug molecule uptake by selected cells, thereby enhancing drug efficacy and the therapeutic index. Targeted LNPs were produced by conjugation of LNPs with either anti-mouse CD169 (clone Ser4) or irrelevant rat IgG at the carbohydrate moiety situated in the hinge region of the antibody Fc domain. This conjugation process is unlikely to compromise the antigen binding affinity of the antibody since this region is sufficiently distant from the variable region responsible for regulating antigen interaction. The modification procedure is schematically represented in **Figure 30**. To begin, a reactive group was introduced onto the antibody by oxidizing specific glycosyl residues within the native glycans to aldehydes, employing sodium periodate ($NaIO_4$) as the oxidation reagent. Subsequently, a heterobifunctional linker was utilized, comprising an azide group for click chemistry and an oxyamine group to react with aldehydes for oxime formation (Chio and Bane 2020). This linker was employed to couple the antibody to a DBCO-functionalized drug-linker on the surface of LNPs.

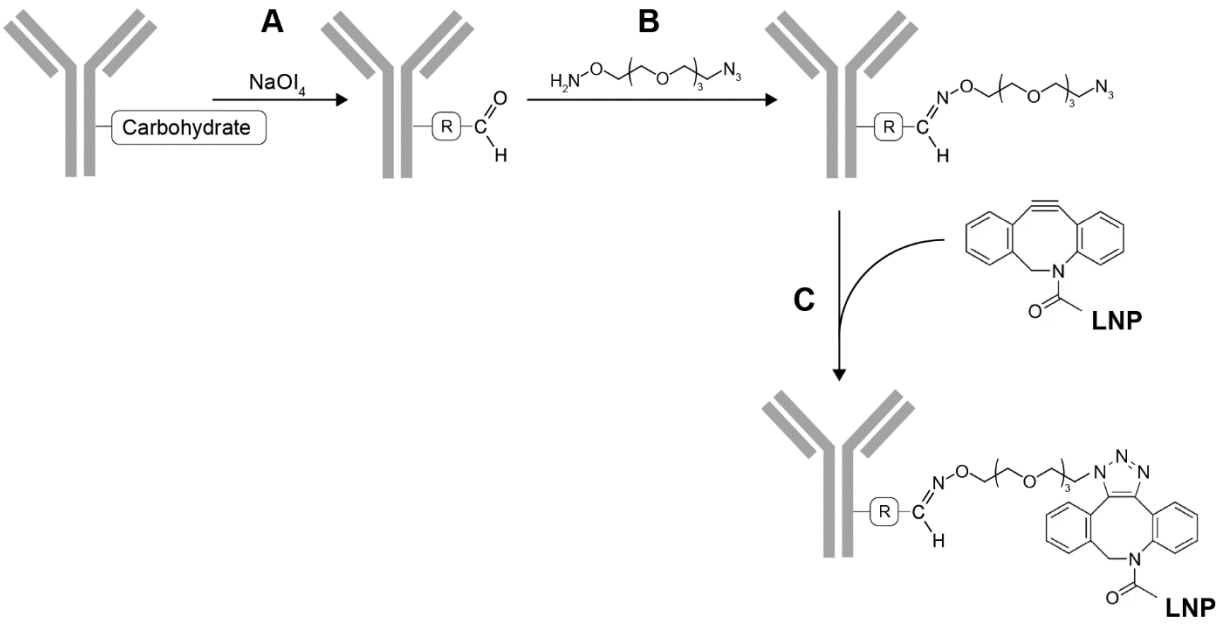

Figure 30. Schematic representation of antibody functionalization and conjugation to LNPs.
(A) Periodate oxidation of the antibody carbohydrate moiety yields aldehyde groups which are subsequently used to **(B)** conjugate aminooxy functionalized linker via oxime ligation. **(C)** Dibenzoazacyclooctyne (DBCO)-containing LNPs undergo azide-alkyne cycloaddition reaction to form a stable triazole linkage.

5.8.6 Specificity and cellular uptake of CD169-targeting LNPs

Due to their relatively large size, the primary route of entry of LNPs into the cell is via endocytosis (Manzanares and Ceña 2020). Therefore, endocytosis-related receptors on MΦ are ideal structures for macrophage-targeting therapies, facilitating fast and specific uptake of LNPs in disease-supporting MΦ and reducing non-specific uptake into other cell types. To analyse the specificity of targeting the MΦ-specific endocytotic scavenger receptor CD169, expression of CD169 by BMDM was first confirmed by FACS, with the majority of BMDM showing basal level expression of CD169 (79.2%, SEM ± 2.5%) on day 6 of differentiation (**Figure 31. A, B**). Subsequently, BMDM were incubated with targeted aCD169- or non-targeted IgG-conjugated calcein (Calc)-loaded LNPs and cellular calcein release was monitored by tracking the changes in its fluorescence intensity. Encapsulated calcein exhibits minimal fluorescence at high concentrations due to self-quenching. However, upon release from the particles, calcein undergoes dilution and subsequent dequenching, leading to an increase in fluorescence. Hence, calcein can be employed as an indicator for lipid vesicle release. When incubating BMDM with Calc-aCD169, release of calcein was observed within 4 h. In contrast, non-targeted IgG-conjugated particles showed no uptake into CD169-expressing cells with only weak fluorescence increase of 11.06%, SEM ± 1.36%, at

5 h (**Figure 31. C**). The data demonstrate fast and specific uptake of targeted particles by CD169-expressing cells with the internalization clearly mediated by CD169 and not by other macrophage receptors, since isotype-conjugated control particles were not internalized in the cell. Although the data suggest receptor-mediated endocytosis, the mechanism of internalization is not clear. Others have shown that CD169 follows the clathrin-mediated endocytosis and it constitutively recycles between the cell surface and early endosomes (Delputte, Van Gorp et al. 2011, Chen, Kawasaki et al. 2012).

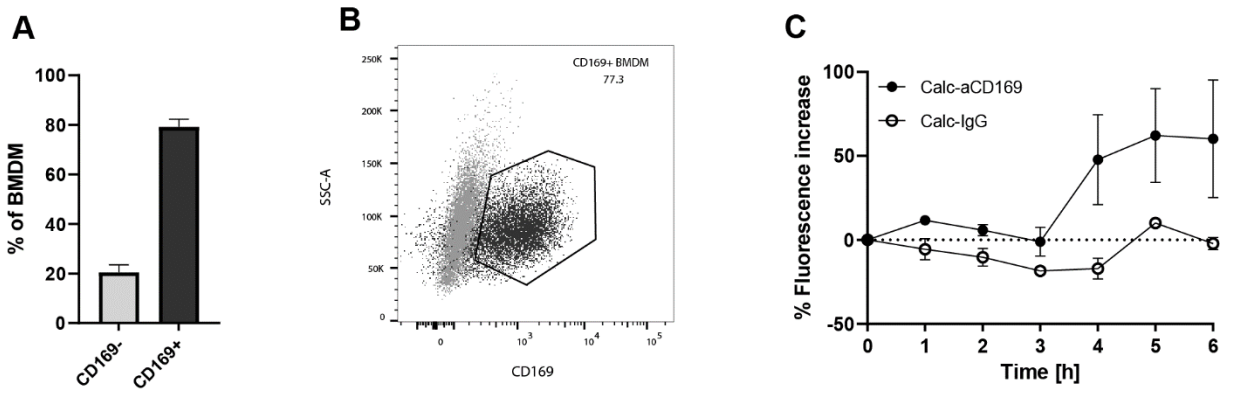

Figure 31. Time-resolved release of LNP-incorporated calcein targeted to CD169+ BMDM.
(A) Frequency of CD169+ BMDM on day 6 of differentiation. BMDM were gated as CD45+ CD11b+ F4/80+ cells. Data are represented as mean ± SEM of n=3. **(B)** Representative FACS plot overlay of CD169+ BMDM (CD45+ CD11b+ F4/80+ parent population) and unstained BMDM. **(C)** BMDM were seeded in black clear-bottom 96-well plates and incubated with Calc-aCD169 or Calc-IgG (0.5 nM total lipid) for 1 h. After three washes in complete medium, calcein release was measured at ex490/em515. Data are represented as mean ± SEM of n=3.

5.8.7 CD169-targeted MF inhibits immunosuppressive polarization of BMDM

To examine the effects of encapsulated MF, BMDM were incubated with aCD169-targeted MF-loaded (MF-aCD169) or empty (Ctrl-aCD169) LNPs for 1 h prior to a 24 h stimulation with TCM/DEX/IL4. MF-aCD169 efficiently reduced *CD163* mRNA gene expression in a dose-dependent manner, while Ctrl-aCD169 at 1.93 x 10^8 particles/ml did not affect its expression (**Figure 32. A, B**). This emphasizes the potential of CD169 as a macrophage-specific molecule allowing targeting of drugs.

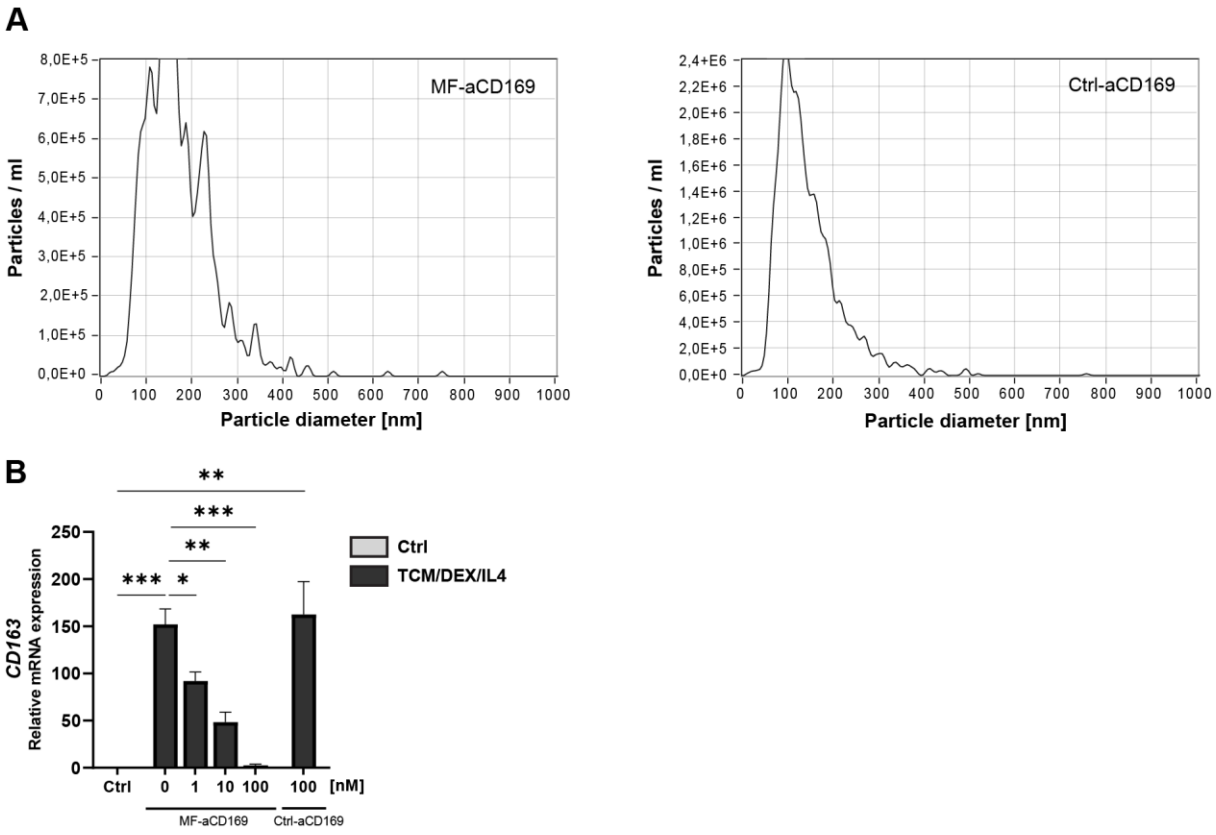

Figure 32. Delivery of MF to BMDM using aCD169-conjugated LNPs.
(A) Determination of aCD169-conjugated MF-loaded (MF-aCD169) or empty (Ctrl-aCD169) LNP concentration by NTA. LNP formulations were diluted 1:10,000 in PBS before measurement. **(B)** Relative expression of *CD163* in BMDM pre-incubated with MF-aCD169 corresponding 1 nM, 10 nM, or 100 nM (1.93×10^8 particles/ml) MF or 1.93×10^8 particles/ml Ctrl-LNPs for 1 h followed by stimulation with TCM/DEX/IL4 for 24 h. Data are represented as mean ± SEM of n=3. Statistically significant differences were calculated using an Unpaired t test. *, $P < 0.05$; **, $P < 0.01$; ***, $P < 0.001$.

5.8.8 *In vivo* biodistribution of CD169-targeted LNPs in tumour-bearing mice

To evaluate the targeting of aCD169-LNPs to CD169+ TAMs in melanoma, calcein loaded aCD169-LNPs or non-targeted control LNPs were injected i.v. in YUMM1.7 tumour-bearing mice. Subsequent *in vivo* fluorescence imaging and flow cytometry analysis showed increased accumulation of targeted LNPs in tumours by specific CD169+ TAM uptake (**Figure 33. A, B**). Calcein fluorescence was detected in major macrophage populations of spleen and liver with higher efficiency of aCD169-LNPs compared to non-targeted control LNPs (**Figure 33. C, D, E**). Notably, WPM in the spleen, characterised by high expression of CD169, demonstrated more efficient uptake of aCD169-LNPs compared to RPM that are not known to express CD169 (Davies, Jenkins et al. 2013, Borges da Silva, Fonseca et al. 2015).

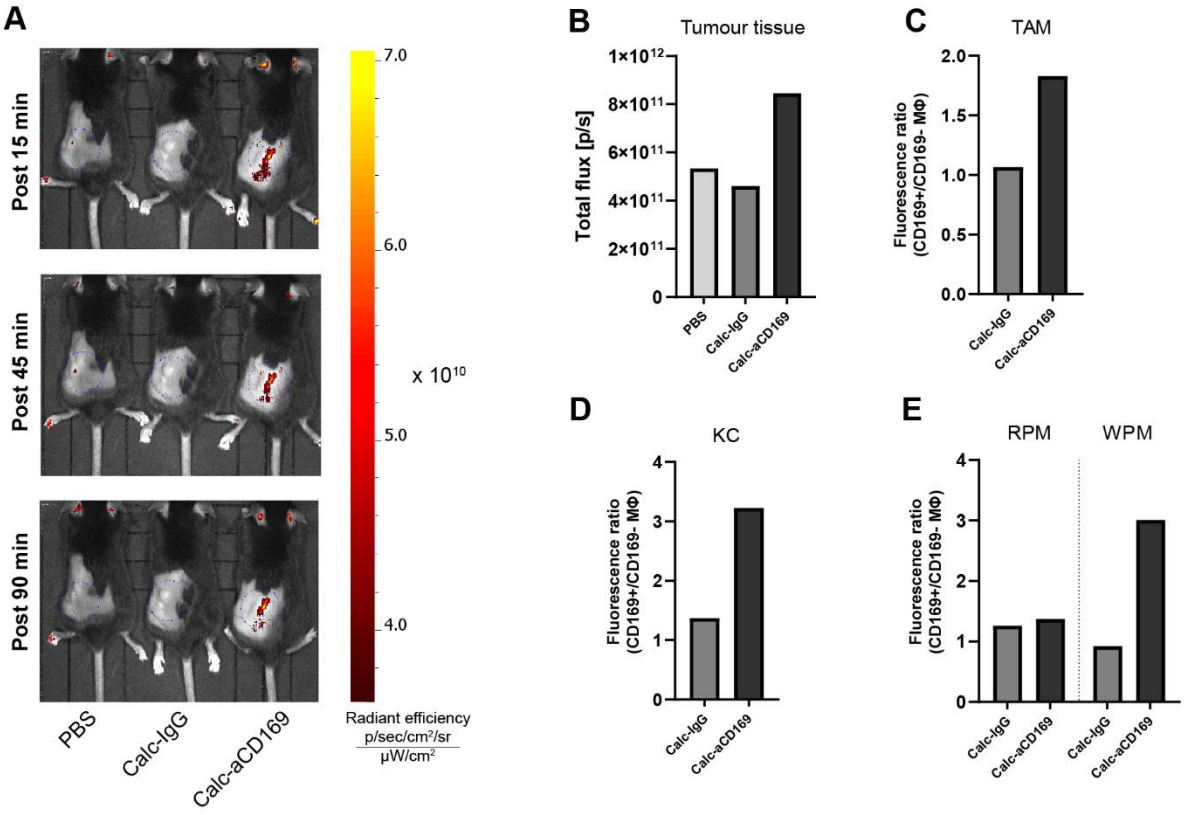

Figure 33. *In vivo* biodistribution of CD169-targeting LNPs in tumour-bearing mice.
(A) Real-time *in vivo* fluorescence images of PBS, non-targeted Calc-IgG or targeted Calc-aCD169 (5 ml/kg, 0.5 mM lipid) in YUMM1.7 tumour-bearing C57BL/6J mice (n=1) at 15, 45, 90 min post i.v. injection using an IVIS *in vivo* imaging system at ex490/em520. Living Image Software was used to subtract background autofluorescence. The colour scale on the *in vivo* images represents signal intensity, with yellow being the most intense and red being the least intense. **(B)** Semi-quantitative fluorescence results of tumour tissue 24 h post-administration. **(C)** FACS analysis of Calc-IgG and Calc-aCD169 uptake by macrophages in tumour tissue (TAMs gated as CD45+ CD11b+ F4/80+), **(D)** liver (Kupffer cells (KC) gated as CD45+ CD11b+ F4/80+) and **(E)** spleen (RPM gated as CD45+ CD11b- F4/80+; WPM gated as CD45+ CD11b+ F4/80-).

5.9 Administration of MF-aCD169 and PD-1 mAbs produced an anti-tumour effect in aPD-1-resistant melanoma

Next, the effect of MF targeted to CD169+ TAMs on the response to aPD-1 checkpoint immunotherapy was investigated in the YUMM1.7 melanoma model, which is inherently resistant to PD-1 mAbs treatment. Mice were treated with MF-aCD169 i.v. three times per week, starting on day 1, plus aPD-1 i.p. twice per week, starting on day 6 after tumour cell inoculation, and tumour development was monitored. Tumour growth was significantly reduced in aPD-1/MF-aCD169 treated mice with reduction in mean tumour volume of 79.57% compared to the Iso/Ctrl-aCD169 control group (Iso/Ctrl-aCD169: 653.89 mm^3 ± 147.21 mm^3; aPD-1/MF-aCD169: 133.58 mm^3 ± 38.21 mm^3; p=0.0108) (**Figure 34**).

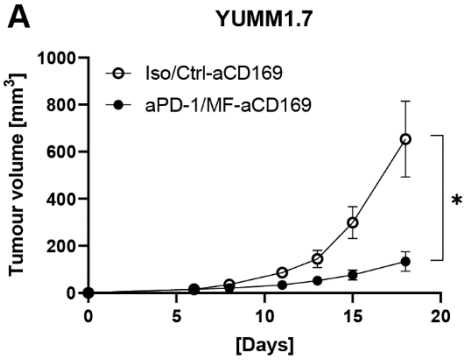

Figure 34. Administration of MF-aCD169 and PD-1 mAbs inhibited tumour progression.
(A) Mean tumour volumes of YUMM1.7 tumour-bearing C57BL/6J wild type mice treated with 12.5 mg/kg PD-1 mAbs (aPD-1) or isotype Ctrl (Iso) twice per week and 0.1 mg/kg MF-loaded (MF-aCD169) or empty control (Ctrl-aCD169) CD169-targeted LNPs three times per week. Data are represented as mean ± SEM of n=6. Statistically significant differences were calculated using an Unpaired t test. *, $P < 0.05$.

Subsequently TAMs (CD45+ CD11b+ Ly6G- SiglecF- F4/80+ cells) (**Figure 35**) and tumour-infiltrating lymphocytes (TILs) were analysed by flow cytometry. No differences were found in the frequency of total immune cells (CD45+ cells) or TAMs, however, aPD-1/MF-aCD169 treated YUMM1.7 tumours demonstrated decreased infiltration of CD169+ TAMs (**Figure 36. A**). Recently it was found that tumour cells have the capacity to induce CD169 expression in monocyte-derived TAMs, and importantly, this was found to be associated with poor survival in patients (Cassetta, Fragkogianni et al. 2019). Next, it was investigated if the phenotype of CD169+ TAMs was affected by GR inhibition. Expression of CD163 by TAMs has been shown to be a particularly strong indicator of poor prognosis in human melanoma (Jensen, Schmidt et al. 2009, Bronkhorst, Ly et al. 2011, Lee, Lee et al. 2019), and specific depletion of CD163+ TAM, defined by expression of

the mature macrophage markers F4/80 and CD169, lead to efficient tumour growth control in a mouse model of melanoma (Etzerodt, Tsalkitzi et al. 2019).

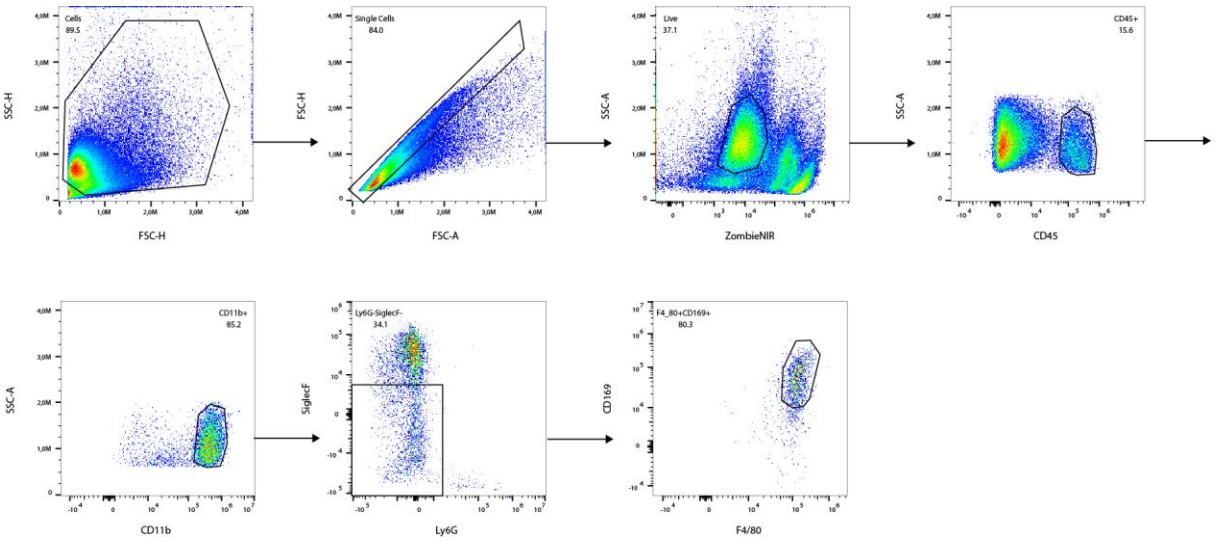

Figure 35. Gating strategy for TAMs.
TAMs: CD45+ CD11b+ Ly6G- SiglecF- F4/80+ CD169+ cells.

While decreased infiltration of CD169+ CD163+ TAMs as % of total immune cells was found in aPD-1/MF-aCD169 treated YUMM1.7 tumours (**Figure 36. B**), the expression of CD163 by CD169+ TAM was not altered (**Figure 36. C**). Upon aPD-1/MF-aCD169, CD169+ TAMs expressed higher levels of the costimulatory molecule CD86+ (**Figure 36. D**), a marker that is associated with an anti-tumour phenotype in TAMs, and in recent studies, low presence of CD86+ and high presence of CD206+ or CD163+ TAMs was correlated with more aggressive tumours (Sun, Luo et al. 2020, Xu, Jiang et al. 2021). CD206 has been widely used as a marker of pro-tumour TAMs (Allavena, Chieppa et al. 2010, Zhang, Yao et al. 2011). aPD-1/MF-aCD169 treatment of YUMM1.7 tumour bearing mice lead to prominent downregulation of CD206 (**Figure 36. E**). In line with this, CD169+ CD163- CD206- TAMs and CD169+ CD86+ CD206- TAMs were strongly increased in aPD-1/MF-aCD169 treated YUMM1.7 tumours, while CD169+ CD86- CD206+ were decreased (**Figure 36. F, G**). Together, the above results strongly suggest successful inhibition of TAM-expressed GR by CD169-targeted MF-loaded LNPs, leading to efficient reprogramming of immunosuppressive TAMs towards an activated, anti-tumour phenotype.

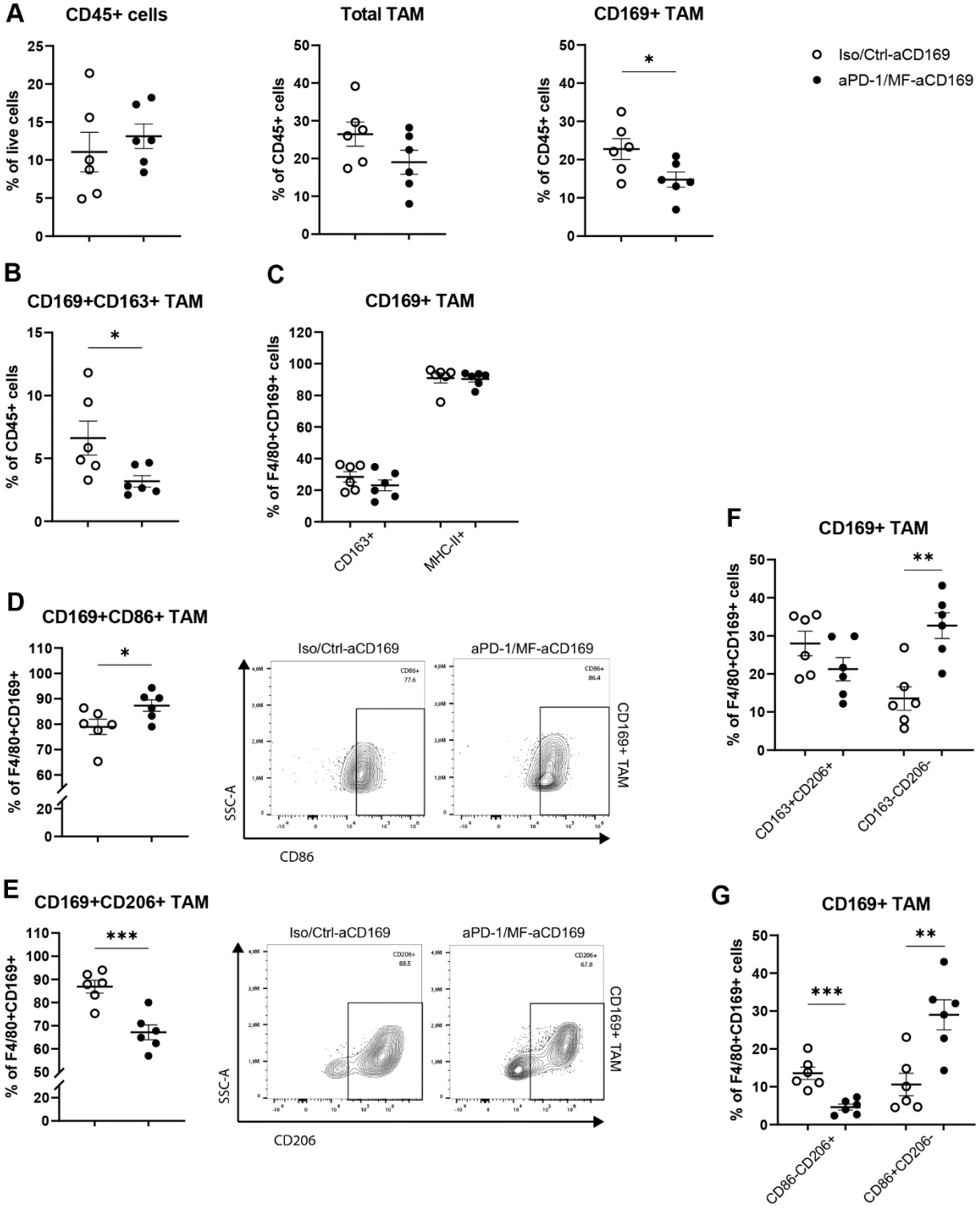

Figure 36. Characterization of TAMs in MF-aCD169/PD-1 mAbs treated YUMM1.7 tumours.
TAMs from Iso/Ctrl-aCD169 (○) or aPD-1/MF-aCD169 (●) treated mice were analysed by flow cytometry. **(A)** Frequency of CD45+ cells, total TAMs (CD45+ CD11b+ Ly6G- SiglecF- F4/80+ cells) and CD169+ TAMs. **(B)** Frequency of CD163 expressing CD169+ TAMs of CD45+ cells. **(C)** Expression of CD163 and MHC-II by CD169+ TAMs. **(D)** Frequency and representative flow plots of CD86 and **(E)** CD206 expressing CD169+ TAMs. **(F)** Co-expression of CD163 and CD206 by CD169+ TAMs. **(G)** Co-expression of CD86 and CD206 by CD169+ TAMs. Data are represented as mean ± SEM

of n=6. Statistically significant differences were calculated using an Unpaired t test. *, P < 0.05; **, P < 0.01; ***, P < 0.001.

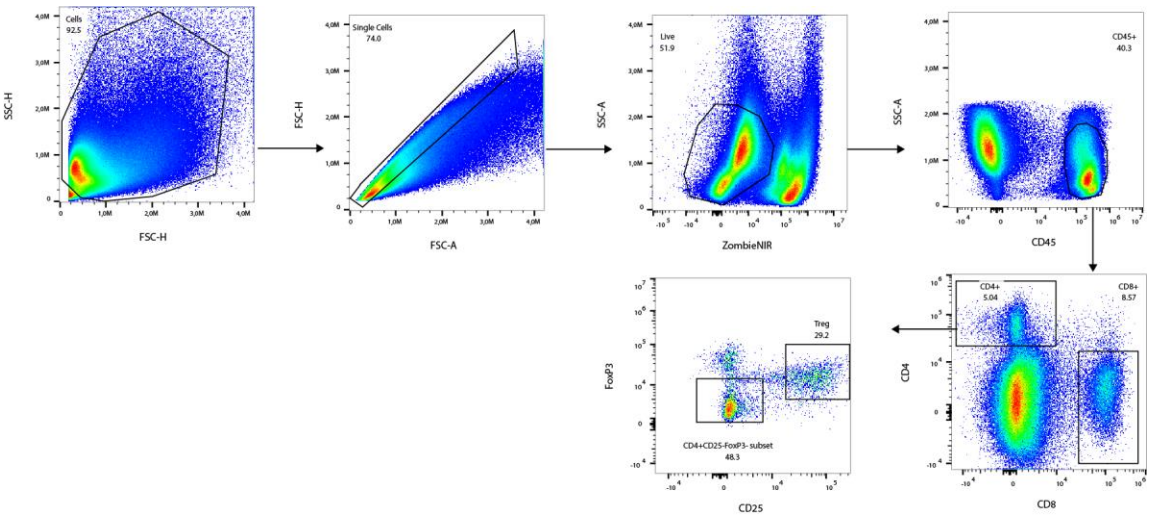

Figure 37. Gating strategy for TILs.
CD8+ T cells: CD45+ CD4- CD8+ cells, CD4+ T cells: CD45+ CD8- CD4+ FoxP3- cells, and Tregs: CD45+ CD8- CD4+ FoxP3+ CD25+ cells.

Subsequently, the effect of reprogrammed TAMs on tumour-infiltrating T cells was investigated. TILs were gated as CD45+ CD4- CD8+ cells (CD8+ T cells), CD45+ CD8- CD4+ FoxP3- cells (CD4+ T cells) and CD45+ CD8- CD4+ FoxP3+ CD25+ cells (regulator T cells, Treg) (**Figure 37**). When analysing TILs, no difference in the frequencies of CD8+ and CD4+ T cells was observed, however, aPD-1/MF-aCD169 treated YUMM1.7 tumours demonstrated decreased infiltration of Tregs (**Figure 38. A**). Tregs are a subtype of T cells with a key role in preventing autoimmune diseases and their presence in the TME inhibits the anti-tumour immune responses. The immune checkpoint molecule PD-1 has a crucial role in the mechanism of T cell exhaustion leading to tumour immune evasion. When analysing the expression of TIL expressed PD-1, decreased infiltration of CD4+ PD-1+ and CD8+ PD-1+ TILs was found in aPD-1/MF-aCD169 treated YUMM1.7 tumours (**Figure 38. B**). Numerous translational and basic studies highlight PD-1 as a key co-inhibitory receptor in the process of T cell exhaustion in tumour or chronic infection, however, PD-1 expression is also induced upon T cell activation, declining to basal levels in a few days. Therefore, it is crucial to study whether PD-1 affects effector functions of T cells or induces an exhaustion program (He and Xu 2020). Previously it was shown that expression of TIM-3 and PD-1 can be used to stratify populations of CD8+ TILs that exhibit different functional phenotypes.

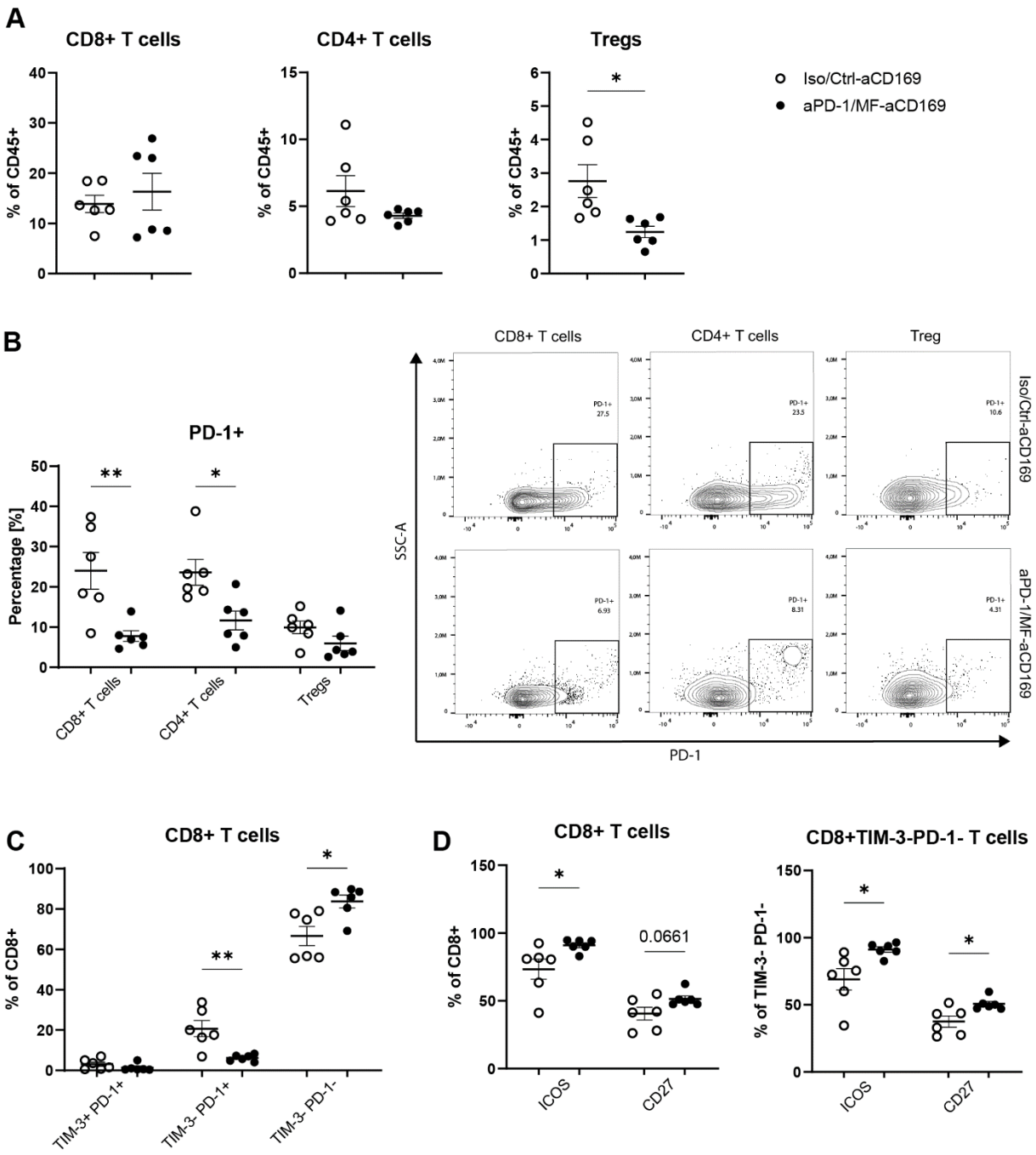

Figure 38. Characterization of TILs in MF-aCD169/PD-1 mAbs treated YUMM1.7 tumours.
TILs from Iso/Ctrl-aCD169 (○) or aPD-1/MF-aCD169 (●) treated mice were analysed by flow cytometry. **(A)** Frequency of CD8+ T cells: CD45+ CD4- CD8+, CD4+ T cells: CD45+ CD8- CD4+ FoxP3-, and Tregs: CD45+ CD8- CD4+ FoxP3+ CD25+. **(B)** Cell frequency and representative flow plots of PD-1 expressing CD8+ T cells, CD4+ T cells and Tregs. **(C)** Co-expression of Tim-3 and PD-1 by tumor infiltrating CD8 + T cells. **(D)** Expression of activation marker (ICOS, CD27) by CD8+ T cells and CD8+ TIM-3- PD- T cell subsets. Data are represented as mean ± SEM of n=6. Statistically significant differences were calculated using an Unpaired t test. *, P < 0.05; **, P < 0.01.

Specifically, CD8+ TIM-3+ PD-1+ double-positive TILs exhibit a severe dysfunctional/exhausted phenotype, CD8+ TIM-3- PD-1+ single-positive TILs exhibit weak dysfunction/exhaustion, while

CD8+ Tim-3- PD-1- double-negative TILs exhibit good effector function (Sakuishi, Apetoh et al. 2010, Anderson, Joller et al. 2016). In aPD-1/MF-aCD169 treated YUMM1.7 tumours, CD8+ T cells demonstrated improved effector functions as indicated by reduced infiltration of CD8+ TIM-3- PD-1+ single-positive T cells and increased infiltration of CD8+ TIM-3- PD-1- double-negative T cells (**Figure 38. C**). The absence of PD-1 and TIM-3 co-expression by CD8+ T cells was prominently associated with high levels of the T-cell activation markers inducible T cell costimulatory (ICOS) and CD27 (**Figure 38. D**). ICOS is a CD28 family costimulatory receptor that is expressed in recently activated or antigen-experienced T cells (Hutloff, Dittrich et al. 1999, Greenwald, Freeman et al. 2005). It binds to ICOS ligand (ICOS-L) expressed on APCs, thereby delivering costimulatory signals that enhance T cell proliferation and expression of cytokines (Metzger, Long et al. 2016). ICOS expression on CD8+ T cells responding to PD-1 blockade has previously been shown (Kamphorst, Pillai et al. 2017). CD27 signals promote survival of activated T cells and are essential for maximal T cell priming as well as memory differentiation (Yamada, Shinozaki et al. 2002, Arens, Schepers et al. 2004). Recently it was found that PD-1 blockade and CD27 stimulation synergize for CD8+ T cell-driven anti-tumour immunity (Buchan, Fallatah et al. 2018).

Collectively, the results described above strongly indicate that CD169+ TAMs responsive to GCs contribute to immunosuppression in the TME, impeding the effectiveness of T cell-based immunotherapy in the YUMM1.7 melanoma model. When GR was specifically inhibited in CD169+ TAMs, it efficiently reprogrammed their immunosuppressive phenotype into an anti-tumour state. This activation led to enhanced T cell responses, making melanoma more receptive to aPD-1 checkpoint immunotherapy.

6 Discussion

Extensive experimental and clinical research has emphasized the significant roles TAMs play in cancer progression. Consequently, there is a growing interest in developing new therapies to target TAMs. Current approaches have mainly focused on inhibiting CSF-1/CSF1R signalling, which controls macrophage development and survival, as well as the CCL2/CCR2 pathway, which regulates monocyte mobilization and recruitment. However, these strategies have shown limited effectiveness in some experimental models and clinical trials (Yang and Zhang 2017). Despite their intrinsic immune-stimulatory potential, one of the major tumour-promoting functions of TAMs is immune suppression. It has been suggested that the TME polarizes macrophages toward an alternative activation state, associated with suppression of T cell functions (Ruffell, Chang-Strachan et al. 2014). Therefore, recent research focuses on reprogramming immunosuppressive TAMs to an activated phenotype, with the goal of re-establishing a favourable immunological anti-tumour T cell response (Beltraminelli and De Palma 2020). T cell-based immunotherapy has had significant impact on the treatment of many cancers, particularly malignant melanoma (Ugurel, Röhmel et al. 2017). However, currently less than 50% of patients undergoing checkpoint immunotherapy develop long-term durable responses, the lack of response often correlating with low TIL recruitment and activation in primary tumours (Tumeh, Harview et al. 2014).

The aim of this study was to investigate the effect of GC-responsive TAMs on tumour development and efficacy of T cell based immunotherapy. GCs and GR signalling are long known to suppress immunity by acting on immune cells. However, only recently evidence has emerged that tumour-derived GCs may serve as a novel mechanism for tumour immune evasion (Anderson and Acharya 2022). Therapeutic GCs have long been administered to treat excessive inflammation in patients with asthma and autoimmune diseases, and in checkpoint immunotherapy of cancer, GCs are routinely used to manage moderate or severe immune-related adverse effects (irAEs). GCs are the recommended first-line agents for treatment of irAE but the data on their possible effects on cancer progression and immune response is conflicting, many clinical data demonstrating an association of GCs and diminished efficacy of checkpoint immunotherapy along with poorer survival (Arbour, Mezquita et al. 2018, Faje, Lawrence et al. 2018, Bai, Hu et al. 2021). Tumour-derived GCs can originate from tumour cells or infiltrating immune cells, exerting inhibitory effects on T cell activity in the tumour (Sidler, Renzulli et al. 2011, Mahata, Zhang et al. 2014, Acharya, Madi et al. 2020, Mahata, Pramanik et al. 2020, Cheng, Ma et al. 2021, Deng, Xia et al.

2021, Melo, Herrera-Rios et al. 2023, Swatler, Ju et al. 2023, Taves, Otsuka et al. 2023). However, the immunoregulatory role of tumour-derived GCs and GR signalling in TAMs remains largely unknown.

The effect of GC-responsive TAMs on tumour development was analysed in a murine melanoma model with genetic ablation of the GR in monocyte-macrophage lineage cells ($GR^{f/fLysMcre}$). Tumour growth was moderately decreased in transgenic mice, with reprogramming of immunosuppressive TAMs towards a more anti-tumour phenotype.

Specific genetic ablation of the GR in CD163+ TAMs ($GR^{f/fCD163cre}$) showed some effect on tumour growth in the B16-F10*luc2* melanoma model, however no effect in the YUMM1.7 melanoma model. It was observed that the $GR^{f/f}$ YUMM1.7 tumours were slightly too small for day 14, which was probably due to incorrect injection of tumour cells and might explain the similar tumour growth between $GR^{f/f}$ and $GR^{f/fCD163cre}$ mice. However, the effect of the genotype on tumour growth was still relatively weak, even in the B16-F10*luc2* model. Previously it was shown that specific depletion of CD163+ TAMs leads to effective tumour growth control and improved response to checkpoint immunotherapy in the YUMM1.7 model (Etzerodt, Tsalkitzi et al. 2019). This implies that depletion of immunosuppressive TAM subsets that are linked to poor prognosis is an efficient strategy for re-educating the TME, while reprogramming strategies might be more efficient in a broader targeting approach.

Next, the effect of GC-responsive TAMs on the response to checkpoint immunotherapy was analysed in a clinically relevant mouse model of melanoma, which is resistant to the current leading checkpoint immunotherapy, antiPD-1. Ablation of TAM expressed GR restored effectiveness of checkpoint immunotherapy in aPD-1–resistant melanoma and strongly promoted tumour regression. This demonstrates the relevance of GC-responsive TAMs in impeding PD-1 mAb treatment. In flow cytometry analysis, the percentage of TAMs were not different, however, their phenotype changed towards a more immunostimulatory, anti-tumour state in the $GR^{f/fLysMcre}$ transgenic model. This was indicated by lower infiltration of CD163+ and MHC-II- CD163+ TAMs, accompanied with higher infiltration of MHC-II+ TAMs and MHC-II+ CD163- TAMs. When immunophenotyping TILs, only moderate effects were observed. TIM-3- PD-1- T cells, which are known to demonstrate effector functions in the TME, were decreased in Iso/$GR^{f/fLysMcre}$ mice, however this was not the case in aPD-1/ $GR^{f/fLysMcre}$. Other markers such as PD-1 did not show any changes

between groups. Furthermore, TILs from aPD1/ $GR^{f/fLysMcre}$ YUMM1.7 tumours showed upregulation of TIM-3+ and LAG-3+ single positive cells. Usually co-expression of multiple exhaustion markers is regarded as indicative of a dysfunctional TIL phenotype, while upregulation of single markers can occur in response to activation. In a recent study, TILs with high LAG-3, but low PD-1 and TIM-3 expression (PD-1- TIM3- LAG-3+) showed higher cytotoxic potential than T cells with elevated TIM-3 alone (PD1- LAG3- TIM-3+) (Datar, Sanmamed et al. 2019). Additionally, LAG-3+ TILs were found to be associated with tumour progression and poor prognosis in different cancers (Hu, Wang et al. 2023). Due to limitations during FACS analysis, the activation state of T cells cannot be fully characterised and no clear conclusion can be drawn. Given that TAMs in YUMM1.7 tumours from transgenic $GR^{f/fLysMcre}$ mice demonstrate changes towards a more immunostimulatory phenotype, the relatively small effect on TILs are somewhat surprising, especially in combination with aPD-1 T cell stimulating checkpoint immunotherapy. It is thought that this does not sufficiently reflect the strong impact on tumour growth control observed in aPD-1/ $GR^{f/fLysMcre}$ treated YUMM1.7 tumours.

To further investigate the effect of tumour-derived GCs on macrophages, an *in vitro* setup was established. BMDM were stimulated with YUMM1.7 TCM to generate a phenotype resembling TAMs *in vivo*. As corticosterone levels were only slightly increased in TCM, DEX was added to the stimulation to be in line with the hypothesis of tumour-derived GCs promoting the immunosuppressive TAM phenotype in the TME. The production or recycling of GCs by YUMM1.7 melanoma cells is presumably either an *in vivo* acquired mechanism or occurs through de novo biosynthesis in a different cell type. Notably, mouse melanoma cell lines were recently found to express *HSD11B1* and produce corticosterone from 11-DHC (Melo, Herrera-Rios et al. 2023). IL-4 is a major activator of the immunosuppressive TAM phenotype also often present in the TME (Landskron, De la Fuente et al. 2014). Interestingly, in human melanoma, steroidogenic gene expression correlates with IL-4 expression and is key inducer of T cell steroidogenesis (Mahata, Pramanik et al. 2020). Stimulation with TCM/DEX/IL4 induced a phenotype in BMDM that resembles TAMs *in vivo*, as indicated by the upregulation of *CD163* and *Mrc1*, markers commonly found on immunosuppressive TAMs. With a significantly greater effect observed with TCM/DEX/IL4 stimulation compared to DEX alone, it is possible that factors derived from the tumour, present in the conditioned media from YUMM1.7 tumour cells along with IL-4, enhance the receptiveness of BMDM to DEX stimulation. Notably, MF was able to abrogate the polarization by DEX, even in the presence of TCM and IL-4. While *CD163* expression mostly responses to DEX stimulation, *Mrc1* is a well-known part of the IL-4-associated gene signature in macrophages and TAMs

(Wang and Joyce 2010). How the GR- and IL-4 signalling pathways interact in macrophages is currently unknown.

11β-HSD1 is an enzyme that regulates local GC activity through converting inactive GC metabolites into their active forms. DEX stimulated upregulation of *HSD11B1* in BMDM at high concentrations. Because GRs are relatively low-affinity, high-capacity receptors, they play the greatest role when cortisol levels are high. TCM/DEX/IL4 stimulation led to prominent *HSD11B1* upregulation accompanied by increased 11β-HSD1 activity in BMDM. GC activation by *HSD11B1* was recently identified as major mechanism that limits T cell-driven immune response and efficiency of PD-1 blockade in melanoma (Melo, Herrera-Rios et al. 2023). *HSD11B1* was found to be expressed in different cellular compartments of both mouse and human melanomas, most notably myeloid cells but also T cells and melanoma cells. The expression of *HSD11B1* was induced by T cell therapies, and importantly, pharmacological inhibition of *HSD11B1* during checkpoint inhibitor treatment improved the efficacy of PD-1 blockade in murine melanoma models. In line with the study by Melo and colleagues, in the present thesis, strong upregulation of *HSD11B1* expression in tumour tissue was detected upon aPD-1 checkpoint immunotherapy treatment as well. Although *HSD11B1* was induced in TAM-like BMDM, the responsible cell type *in vivo* cannot be identified here.

In certain cell types, 11β-HSD1 can be induced by GCs through a positive feed-forward mechanism. 11β-HSD1 catalyses the regeneration of active corticosterone from inactive 11-DHC, thereby amplifying GC levels and its cellular actions. Corticosterone itself increases 11β-HSD1 in an autocrine manner (Sun, He et al. 2002, Inder, Obeyesekere et al. 2012). To test, if this mechanism can be abrogated by inhibition of GR signalling in TAM-like BMDM, *HSD11B1* expression was induced in the presence of MF that does not bind to 11β-HSD1. The induction and activity of *HSD11B1* was efficiently inhibited by MF, interrupting the self-reinforcing mechanism by GCs and 11β-HSD1 in TAM-like BMDM. To validate this *in vivo*, *HSD11B1* was analysed in the $GR^{f/fLysMcre}$ transgenic melanoma model. No differences were found in *HSD11B1* expression in YUMM1.7 tumour tissue from $GR^{f/f}$ wild type and $GR^{f/fLysMcre}$ transgenic mice, however GR knockdown prominently decreased the aPD-1 induced upregulation of *HSD11B1*. This strongly suggests that GC pathway activity is part of the mechanism found in checkpoint immunotherapy resistant melanoma. Importantly, analysis of human melanoma demonstrated correlation between expression of *HSD11B1* and markers indicating immunosuppressive TAMs (*CD274*, *CD163*) underlining the translational relevance of these findings. The relevance of the self-reinforcing mechanism by GCs and 11β-HSD1 is further supported by a very recent study by Matthew D. Taves and colleagues (Taves, Otsuka et al. 2023). In this thesis, tumour-derived GCs were found to inhibit CD8+ T cell

activity and drive Treg-mediated immunosuppression. Genetic ablation of GR in Tregs, $GR^{f/fFoxP3cre}$ transgenic mice, led to restored CD8+ T cell activation and reduced tumour growth in tumours with high *HSD11B1* expression.

GCs can stem from the systemic GC production by the HPA axis or local production or activation in the tissue. To analyse if local GC biosynthesis occurs in the tumour, Cyp11A1, the first and rate-limiting enzyme of the GC biosynthesis that can be regarded as a biomarker of de novo steroidogenesis, was analysed in tumour tissue. *Cyp11A1* was expressed in YUMM1.7 tumour tissue, however, which cell type was the source of GCs in the TME remains unknown. Notably, *Cyp11A1* expression was not detected in stimulated or unstimulated BMDM, suggesting either low or absent active GC biosynthesis in BMDM or that macrophages acquire ability for GC synthesis *in vivo*. In a recent study, cells of the monocyte-macrophage lineage, cancer-associated fibroblasts (CAFs), tumour-associated DCs and T cells (mostly CD4+ T cells) expressed Cyp11A1, with cells of the monocyte-macrophage lineage being identified as the main source of de novo GC biosynthesis (Acharya, Madi et al. 2020). This was supported by effective tumour growth control in $Cyp11A1^{f/fLysMcre}$ transgenic mice, which exhibit cell specific conditional deletion of Cyp11A1 in monocyte-macrophage lineage cells. In a similar approach, ablation of Cyp11A1 in CD4+ T cells promoted anti-tumour immunity (Mahata, Zhang et al. 2014, Mahata, Pramanik et al. 2020). Another study found evidence for GC activation by HSD11B1 but not GC de novo biosynthesis in peripheral T cells, suggesting that tumour-infiltrating T cells can acquire ability for GC synthesis (Rocamora-Reverte, Reichardt et al. 2017). Additionally, Yalan Deng and colleagues identified GR signalling in cancer cells as a tumour-intrinsic mechanism of immunosuppression (Deng, Xia et al. 2021). In another study, stress-induced glucocorticoid increase upregulated Tsc22d3 in DCs, which impaired the capability of DCs to coordinate an effective anti-tumour immune response and importantly, this was abrogated by treatment with MF (Yang, Xia et al. 2019).

In line with the present work, these recent studies emphasize the importance of local GC signalling for tumour immune surveillance. Collectively, the present work shows that *HSD11B1* upregulation occurred in response to checkpoint immunotherapy in a clinically relevant mouse model of melanoma, which is resistant to PD-1 mAbs treatment. The small molecule inhibitor MF, which is approved for clinical use, showed high efficiency to inhibit induction of TAM-like phenotype and function *in vitro*. Therefore, combining MF targeted to immunosuppressive TAMs with checkpoint immunotherapy might improve cancer immunotherapy.

To specifically target TAMs in the TME, a therapeutic approach based on targeted delivery of MF using antibody-conjugated LNPs was established. Due to the relatively large size of LNPs compared with antibodies, for example, they tend to accumulate in tumour tissue via leaky vasculature, while being less able to penetrate deep into healthy tissue. This concept is called the enhanced permeability and retention (EPR) effect (Hobbs, Monsky et al. 1998, Torchilin, Levchenko et al. 2001, Ngoune, Peters et al. 2016). MF-loaded aCD169-conjugated LNPs (MF-aCD169) were produced based on a study by Zhigaltsev and colleagues (Zhigaltsev, Belliveau et al. 2012), and uptake by CD169+ BMDM and efficiency to inhibit induction of TAM-like phenotype in BMDM was validated *in vitro*. The biodistribution study confirmed preferential accumulation of aCD169-conjugated LNPs in tumour tissue and uptake by CD169 expressing macrophages in liver, spleen and tumour. Dosing of MF-aCD169 *in vivo* was estimated based on LNP concentrations previously used in the group and known serum corticosterone levels. The LNP concentration corresponded to a dose of 0.1 mg/kg MF, which is 0.002 mg MF per dose in a 20 g mouse. Given that serum corticosterone levels in mice vary between approximately 50 ng/ml and 500 ng/ml depending on the time point of measurement (Veniant, Hale et al. 2009), this was assumed a suitable dose.

The effect of MF-aCD169 on immunotherapy resistance was investigated in a clinically relevant mouse model of melanoma, which is resistant to the current leading checkpoint immunotherapy, antiPD-1. Tumour growth was effectively controlled by aPD-1/MF-aCD169 treatment of YUMM1.7 tumour-bearing mice with similar reduction in tumour sizes compared to the aPD-1/$GR^{f/fLysMcre}$ transgenic model. MF-aCD169 efficiently reprogrammed immunosuppressive TAMs towards an activated, anti-tumour phenotype, having minor impact on total TAM numbers. However, selective inhibition of GR in CD169+ TAMs profoundly reduced immunosuppressive markers (CD163, CD206) and increased expression of the activation marker CD86. Interestingly, the $GR^{f/fLysMcre}$ transgenic model was not as effective in reprogramming TAMs. Presumably this is due to the more efficient abrogation of GR signalling by MF compared to the GR knockdown in the $GR^{f/fLysMcre}$ transgenic model. Deletion efficiency and specificity of the LysM-cre mouse strain was analysed in the LysM-cre mT/mG reporter model, and demonstrated medium to high, however not complete knockdown of the GR. Additionally, the analysis was performed in the spleen of healthy mice, and no data about the activity of the LysM-cre promoter in TAMs is available. To achieve sustained reprogramming of TAMs, MF-aCD169 was injected three times per week, starting the day after tumour cell inoculation. Notably, no conclusion can be drawn about the period during which an immunostimulatory phenotype through GR inhibition is maintained by TAMs in the TME. It should

be considered that complete repopulation of tumours by MN-derived cells occurs rapidly, typically within 72 h after treatment with TAM-depleting therapies (Strachan, Ruffell et al. 2013). Whether MF-aCD169 treated TAMs persist within the tumour and the turnover of TAMs in the present thesis remains unknown.

Immunophenotyping analysis of melanoma after MF-aCD169 mediated reprogramming of TAMs did not show differences in the percentage of CD4+ or CD8+ TILs, however their phenotype was affected. This implies that a low yet more functional T cell response is effective in controlling tumour growth. TILs exhibited a more activated phenotype as indicated by downregulation of PD-1 checkpoint molecules, reduced dysfunction/exhaustion (CD8+ TIM-3- PD-1+) and increased effector functions (CD8+ TIM-3- PD-1-) in CD8+ TILs, and this was accompanied by upregulation of T cell activation marker (ICOS, CD27). In line with a recent study that showed that tumour-derived GCs suppress antitumor immunity by enhancing Treg function, MF-aCD169 mediated reprograming of TAMs led to reduced Treg infiltration (Taves, Otsuka et al. 2023).

In summary, the present thesis demonstrates a profound immunosuppressive function for GC-responsive CD169+ TAM in melanoma that is independent of the PD-1/PD-L1 axis. Specific inhibition of GR signalling in CD169+ TAMs effectively reprogrammed their immunosuppressive phenotype into an anti-tumour state. This activation led to enhanced T cell responses, making melanoma more receptive to aPD-1 checkpoint immunotherapy. Furthermore, together with previously described results from the analysis of *in vitro* generated TAMs, this confirms the suitability of MF as an agent to effectively inhibit GR signalling in TAMs *in vitro* and *in vivo*.

MF (RU-486) is an antiprogesterone and antiglucocorticoid agent that was developed in the 1980s to be taken with misoprostol for medication abortion care. It binds with high affinity (KD ≤ 10^{-9} M) to the progesterone receptor (PR) and the GR (Cadepond, Ulmann et al. 1997). While the effect of GR activation on the polarization of macrophages is well-documented, the findings about the function of PRs in macrophages are inconsistent and contradictory, studies showing inhibitory or stimulatory effects depending on the cell type used (Miller, Alley et al. 1996, Miller and Hunt 1996, Menzies, Henriquez et al. 2011, Lu, Reese et al. 2015, Cioni, Zaalberg et al. 2020). With both receptors expressed in macrophages, the effect of MF, as for other hormone antagonists, are only straightforward in cases where the effect of one particular hormone is predominant. The relevance of MF as antiglucocorticoid agent is evidenced by its clinical use in treatment of endogeneous Cushing syndrome (FDA-approval in 2012), which results from ACTH-dependent or -independent excessive production of cortisol by adrenal glands. Additionally, MF is investigated for treatment of depression and psychosis with HPA axis abnormalities (Kling, Whitfield Jr et al.

1989, Gallagher and Young 2006). In preclinical oncology studies, MF was reported to have potent anti-proliferative effects on cancer cell lines derived from tumours of the breast, endometrium, cervix, prostate, gastrointestinal tract, brain, bone and ovary (Fried, Meister et al. 1990, El Etreby, Liang et al. 1998, Cher, Towler et al. 2006, Fiscella, Bonfiglio et al. 2011, Ligr, Li et al. 2012, Wang, Yang et al. 2012, Goel, Malik et al. 2013, Wempe, Gamarra-Luques et al. 2013). However, clinical trials have not produced promising data to support its use as an anti-cancer drug (Chen, Wang et al. 2014).

Recently, MF was used to inhibit GR signalling in tumour cells in a murine model of pancreatic ductal adenocarcinoma (PDAC) (Deng, Xia et al. 2021). Administration of MF lead to PD-L1 downregulation and MHC-I upregulation in tumour cells, which in turn promoted the infiltration and activity of cytotoxic T cells, leading to enhanced anti-tumour immunity and improved response to checkpoint immunotherapy. MF was administered systemically by oral application on a schedule of twice every 3 days and a dose of 60 mg/kg MF, dissolved in vehicle solvent containing 5% dimethylacetamide and 95% olive oil. The dose was calculated based on a phase 2 clinical trial (NCT 02642939) and dose conversion between animals and humans (Nair and Jacob 2016). In humans this dose corresponds to approximately 256 mg single dose, depending on the formula used for calculation. For comparison, the recommended starting dose to treat endogenous Cushing syndrome in humans is 300 mg once daily, which may be increased to a maximum of 1200 mg once daily. For medical abortion a single dose of 200 mg MF and 800 mg misoprostol is used. Given the differences in tumour model and application method of MF, it is difficult to directly compare the two doses needed to achieve effective tumour growth control in mice between the present thesis, and the study by Yalan Deng and colleagues. With 69% oral bioavailability of MF (in humans), this corresponds to approximately 40 mg/kg i.v.. Yalan Deng and colleagues noted that, although MF plus dual checkpoint immunotherapy improved survival in tumour-bearing mice, the dose and schedule may need further optimization to improve efficacy and/or reduce possible toxicity. No further information of observed toxicities was provided, however, since MF is a clinical GR antagonist it has an established safety profile. In another study, MF was utilized to treat stress-induced increase of GCs which led to immunosuppression, thereby undermining therapy-induced anti-tumour immunity. (Yang, Xia et al. 2019). MF was administered i.p. at 4 mg/kg, dissolved in water and administered daily or every other day for 7-9 days. Interestingly, this thesis aimed to antagonize GCs stemming from the systemic blood circulation, in contrast to the present thesis and the previously described study by Yalan Deng and colleagues, which focused on tumour-

derived GCs. Notably, the dose of MF utilized in the present thesis was 0.1 mg/kg MF administered 3 times per week plus PD-1 mAbs twice per week. This dosage is significantly lower than that used in both of the previously mentioned studies.

Side effects reported in humans are associated with the MF-mediated inhibition of the negative feedback mechanism of GCs in the HPA axis, leading to HPA axis dysregulation and impeded homeostasis in GC levels. This was demonstrated by enhanced plasma ACTH and increased plasma cortisol levels during the peak of the diurnal variation in cortisol secretion in both healthy humans and patients (Bertagna, Bertagna et al. 1984, Gaillard, Riondel et al. 1984, Kling, Whitfield Jr et al. 1989, Kling, Demitrack et al. 1993). Other side effects of MF include symptoms of cortisol withdrawal, hypokalaemia, change in thyroid function and effects related to its anti-progesterone activity (Brown, East et al. 2020). This indicates that global targeting with MF could be challenging in cancer patients. GCs are important for normal body homeostasis, therefore 11β-HSD1 was previously selected for global pharmacological targeting in preclinical melanoma models (Melo, Herrera-Rios et al. 2023, Taves, Otsuka et al. 2023). This approach was chosen as HSD11B1 is upregulated in tumour tissue in response to checkpoint immunotherapy treatment, providing some specificity. Notably, Matthew D. Taves and colleagues reported that global pharmacological inhibition of 11β-HSD1 reduced tumour growth with similar efficiency compared to $GR^{f/fFoxP3}$ transgenic mice with selective GR knockdown in Tregs (Taves, Otsuka et al. 2023). Synthetic GCs are commonly used for treatment of severe irAEs (Arbour, Mezquita et al. 2018, Faje, Lawrence et al. 2018, Bai, Hu et al. 2021). Therefore, GR blockade, GC synthesis or GC activation in combination with checkpoint immunotherapy could exacerbate irAEs or increase the likelihood of their occurrence. This highlights the importance of cell-specific targeting with drugs that address tumour-derived GC and careful selection of the target. Due to the approach of targeting CD169+ TAMs, no systemic side effects of MF were expected during the present thesis. This was evidenced by fast accumulation of Calc-aCD169 in tumour tissue and uptake by CD169+ TAMs. Side effects of MF-aCD169 are mostly expected from uptake of LNPs by CD169+ macrophages in normal tissue. In mice, CD169 is expressed on bone marrow macrophages, alveolar macrophages, white pulp (metallophilic) macrophages in the spleen, and subcapsular sinus macrophages in the lymph nodes (Crocker, Kelm et al. 1991, Crocker, Mucklow et al. 1994, Nauwynck, Duan et al. 1999, Hartnell, Steel et al. 2001, Gray and Cyster 2012). Recently, expression of CD169 was also described in a subset of liver Kupffer cells (Elchaninov, Fatkhudinov et al. 2019).

Human CD169 is mainly expressed by macrophages in the perifollicular zone of the spleen, subcapsular sinus of lymph nodes and at a lower level by splenic red pulp macrophages, which is

very similar to the expression observed in mice (Steiniger, Barth et al. 1997, van Dinther, Lopez Venegas et al. 2019). Additionally, expression of CD169 was detected in conventional DCs (cDCs), but not in plasmacytoid DCs (pDCs). Also, cDCs were reported to take up sialic acid-conjugated liposomal cancer vaccines (Kawasaki, Vela et al. 2013, Van Dinther, Veninga et al. 2018, Affandi, Grabowska et al. 2020). Additionally, it was found that tumour cells have the capacity to induce CD169 expression in monocyte-derived TAMs, which was found to be associated with poor survival in patients (Cassetta, Fragkogianni et al. 2019), confirming the selection of CD169 on TAMs as a suitable target for delivery of MF.

6.1 Conclusion

In summary, the present thesis demonstrates a profound immunosuppressive function for GC-responsive TAMs in melanoma that is resistant to aPD-1 checkpoint immunotherapy. As the GC pathways and their immunoregulatory functions are conserved between mice and humans, these findings may be relevant to human melanoma. Mifepristone is a clinical GR antagonist with well-established safety profiles, suggesting a possible avenue for therapeutic targeting to increase the effectiveness of checkpoint immunotherapy in the clinic.

7 References

Abram, C. L., et al. (2014). "Comparative analysis of the efficiency and specificity of myeloid-Cre deleting strains using ROSA-EYFP reporter mice." Journal of immunological methods **408**: 89-100.

Acharya, N., et al. (2020). "Endogenous glucocorticoid signaling regulates CD8+ T cell differentiation and development of dysfunction in the tumor microenvironment." Immunity **53**(3): 658-671. e656.

Achkova, D. and J. Maher (2016). "Role of the colony-stimulating factor (CSF)/CSF-1 receptor axis in cancer." Biochemical Society Transactions **44**(2): 333-341.

Affandi, A. J., et al. (2020). "Selective tumor antigen vaccine delivery to human CD169+ antigen-presenting cells using ganglioside-liposomes." Proceedings of the National Academy of Sciences **117**(44): 27528-27539.

Ali, Z., et al. (2013). "Melanoma epidemiology, biology and prognosis." European Journal of Cancer Supplements **11**(2): 81-91.

Allavena, P., et al. (2010). "Engagement of the mannose receptor by tumoral mucins activates an immune suppressive phenotype in human tumor-associated macrophages." Clinical and Developmental Immunology **2010**.

Allavena, P. and A. Mantovani (2012). "Immunology in the clinic review series; focus on cancer: tumour-associated macrophages: undisputed stars of the inflammatory tumour microenvironment." Clinical & Experimental Immunology **167**(2): 195-205.

Anderson, A. C. and N. Acharya (2022). "Steroid hormone regulation of immune responses in cancer." Immunometabolism (Cobham (Surrey, England) **4**(4): e00012.

Anderson, A. C., et al. (2016). "Lag-3, Tim-3, and TIGIT: co-inhibitory receptors with specialized functions in immune regulation." Immunity **44**(5): 989-1004.

Andtbacka, R. H. I., et al. (2015). Phase 2, multicenter, randomized, open-label trial assessing efficacy and safety of talimogene laherparepvec (T-VEC) neoadjuvant treatment (tx) plus surgery vs surgery for resectable stage IIIB/C and IVM1a melanoma (MEL), American Society of Clinical Oncology.

Aplin, A. E., et al. (2011). "Mechanisms of resistance to RAF inhibitors in melanoma." Journal of investigative dermatology **131**(9): 1817-1820.

Arbour, K. C., et al. (2018). "Impact of baseline steroids on efficacy of programmed cell death-1 and programmed death-ligand 1 blockade in patients with non-small-cell lung cancer." Journal of Clinical Oncology **36**(28): 2872-2878.

Arens, R., et al. (2004). "Tumor rejection induced by CD70-mediated quantitative and qualitative effects on effector CD8+ T cell formation." The Journal of experimental medicine **199**(11): 1595-1605.

Arlauckas, S. P., et al. (2017). "In vivo imaging reveals a tumor-associated macrophage–mediated resistance pathway in anti–PD-1 therapy." Science translational medicine **9**(389): eaal3604.

Arwert, E. N., et al. (2018). "A unidirectional transition from migratory to perivascular macrophage is required for tumor cell intravasation." Cell reports **23**(5): 1239-1248.

Ascierto, P. A., et al. (2013). "Phase II trial (BREAK-2) of the BRAF inhibitor dabrafenib (GSK2118436) in patients with metastatic melanoma." J Clin Oncol **31**(26): 3205-3211.

Attia, M. F., et al. (2019). "An overview of active and passive targeting strategies to improve the nanocarriers efficiency to tumour sites." Journal of Pharmacy and Pharmacology **71**(8): 1185-1198.

Backer, R., et al. (2010). "Effective collaboration between marginal metallophilic macrophages and CD8+ dendritic cells in the generation of cytotoxic T cells." Proceedings of the National Academy of Sciences **107**(1): 216-221.

Bai, X., et al. (2021). "Early use of high-dose glucocorticoid for the management of irAE is associated with poorer survival in patients with advanced melanoma treated with anti–PD-1 monotherapy." Clinical cancer research **27**(21): 5993-6000.

Baschant, U. and J. Tuckermann (2010). "The role of the glucocorticoid receptor in inflammation and immunity." The Journal of steroid biochemistry and molecular biology **120**(2-3): 69-75.

Beltraminelli, T. and M. De Palma (2020). "Biology and therapeutic targeting of tumour-associated macrophages." The Journal of pathology **250**(5): 573-592.

Bertagna, X., et al. (1984). "The new steroid analog RU 486 inhibits glucocorticoid action in man." The Journal of Clinical Endocrinology & Metabolism **59**(1): 25-28.

Bonde, A.-K., et al. (2012). "Intratumoral macrophages contribute to epithelial-mesenchymal transition in solid tumors." BMC cancer **12**: 1-15.

Borges da Silva, H., et al. (2015). "Splenic macrophage subsets and their function during blood-borne infections." Frontiers in immunology **6**: 480.

Bronkhorst, I. H., et al. (2011). "Detection of M2-macrophages in uveal melanoma and relation with survival." Investigative ophthalmology & visual science **52**(2): 643-650.

Brown, D. R., et al. (2020). "Clinical management of patients with Cushing syndrome treated with mifepristone: consensus recommendations." Clinical Diabetes and Endocrinology **6**: 1-13.

Buchan, S. L., et al. (2018). "PD-1 blockade and CD27 stimulation activate distinct transcriptional programs that synergize for CD8+ T-cell–driven antitumor immunity." Clinical cancer research **24**(10): 2383-2394.

Cadepond, P., F, et al. (1997). "RU486 (mifepristone): mechanisms of action and clinical uses." Annual review of medicine **48**(1): 129-156.

Cain, D. W. and J. A. Cidlowski (2017). "Immune regulation by glucocorticoids." Nature Reviews Immunology **17**(4): 233-247.

Casanova-Acebes, M., et al. (2021). "Tissue-resident macrophages provide a pro-tumorigenic niche to early NSCLC cells." Nature **595**(7868): 578-584.

Cassetta, L., et al. (2019). "Human tumor-associated macrophage and monocyte transcriptional landscapes reveal cancer-specific reprogramming, biomarkers, and therapeutic targets." Cancer cell **35**(4): 588-602. e510.

Chen, C., et al. (2013). "Structural basis for molecular recognition of folic acid by folate receptors." Nature **500**(7463): 486-489.

Chen, J., et al. (2014). "The unique pharmacological characteristics of mifepristone (RU486): from terminating pregnancy to preventing cancer metastasis." Medicinal research reviews **34**(5): 979-1000.

Chen, W., et al. (2003). "Conversion of peripheral CD4+ CD25− naive T cells to CD4+ CD25+ regulatory T cells by TGF-β induction of transcription factor Foxp3." The Journal of experimental medicine **198**(12): 1875-1886.

Chen, W. C., et al. (2012). "Antigen delivery to macrophages using liposomal nanoparticles targeting sialoadhesin/CD169." PloS one **7**(6): e39039.

Cheng, H., et al. (2021). "The tumor microenvironment shapes the molecular characteristics of exhausted CD8+ T cells." Cancer letters **506**: 55-66.

Cher, M. L., et al. (2006). "Cancer interaction with the bone microenvironment: a workshop of the National Institutes of Health Tumor Microenvironment Study Section." The American journal of pathology **168**(5): 1405-1412.

Chio, T. I. and S. L. Bane (2020). "Click chemistry conjugations." Antibody-Drug Conjugates: Methods and Protocols: 83-97.

Cioni, B., et al. (2020). "Androgen receptor signalling in macrophages promotes TREM-1-mediated prostate cancer cell line migration and invasion." Nature communications **11**(1): 4498.

Clausen, B., et al. (1999). "Conditional gene targeting in macrophages and granulocytes using LysMcre mice." Transgenic research **8**: 265-277.

Cortez-Retamozo, V., et al. (2012). "Origins of tumor-associated macrophages and neutrophils." Proceedings of the National Academy of Sciences **109**(7): 2491-2496.

Crocker, P., et al. (1991). "Purification and properties of sialoadhesin, a sialic acid-binding receptor of murine tissue macrophages." The EMBO journal **10**(7): 1661-1669.

Crocker, P., et al. (1994). "Sialoadhesin, a macrophage sialic acid binding receptor for haemopoietic cells with 17 immunoglobulin-like domains." The EMBO journal **13**(19): 4490-4503.

Crocker, P. R. and A. Varki (2001). "Siglecs in the immune system." Immunology **103**(2): 137.

Czarnecka, A. M., et al. (2020). "Targeted therapy in melanoma and mechanisms of resistance." International Journal of Molecular Sciences **21**(13): 4576.

Datar, I., et al. (2019). "Expression analysis and significance of PD-1, LAG-3, and TIM-3 in human non–small cell lung cancer using spatially resolved and multiparametric single-cell analysis." Clinical cancer research **25**(15): 4663-4673.

Davies, L. C., et al. (2013). "Tissue-resident macrophages." Nature immunology **14**(10): 986-995.

De Palma, M. and C. E. Lewis (2013). "Macrophage regulation of tumor responses to anticancer therapies." Cancer cell **23**(3): 277-286.

De Vos van Steenwijk, P., et al. (2013). "Tumor-infiltrating CD14-positive myeloid cells and CD8-positive T-cells prolong survival in patients with cervical carcinoma." International journal of cancer **133**(12): 2884-2894.

Delputte, P. L., et al. (2011). "Porcine sialoadhesin (CD169/Siglec-1) is an endocytic receptor that allows targeted delivery of toxins and antigens to macrophages." PloS one **6**(2): e16827.

Deng, Y., et al. (2021). "Glucocorticoid receptor regulates PD-L1 and MHC-I in pancreatic cancer cells to promote immune evasion and immunotherapy resistance." Nature communications **12**(1): 7041.

Dong, H., et al. (2002). "Tumor-associated B7-H1 promotes T-cell apoptosis: a potential mechanism of immune evasion." Nature medicine **8**(8): 793-800.

El Etreby, M. F., et al. (1998). "Additive effect of mifepristone and tamoxifen on apoptotic pathways in MCF-7 human breast cancer cells." Breast cancer research and treatment **51**: 149-168.

Elchaninov, A. V., et al. (2019). "Phenotypical and functional polymorphism of liver resident macrophages." Cells **8**(9): 1032.

Ernsting, M. J., et al. (2013). "Factors controlling the pharmacokinetics, biodistribution and intratumoral penetration of nanoparticles." Journal of controlled release **172**(3): 782-794.

Etzerodt, A. and S. K. Moestrup (2013). "CD163 and inflammation: biological, diagnostic, and therapeutic aspects." Antioxidants & redox signaling **18**(17): 2352-2363.

Etzerodt, A., et al. (2020). "Tissue-resident macrophages in omentum promote metastatic spread of ovarian cancer." Journal of Experimental Medicine **217**(4).

Etzerodt, A., et al. (2019). "Specific targeting of CD163+ TAMs mobilizes inflammatory monocytes and promotes T cell–mediated tumor regression." Journal of Experimental Medicine **216**(10): 2394-2411.

Faje, A. T., et al. (2018). "High-dose glucocorticoids for the treatment of ipilimumab-induced hypophysitis is associated with reduced survival in patients with melanoma." Cancer **124**(18): 3706-3714.

Feng, M., et al. (2019). "Phagocytosis checkpoints as new targets for cancer immunotherapy." Nature Reviews Cancer **19**(10): 568-586.

Ferlay, J., et al. (2018). Global cancer Observatory: cancer today. Lyon, France: international agency for research on cancer.

Fiscella, J., et al. (2011). "Distinguishing features of endometrial pathology after exposure to the progesterone receptor modulator mifepristone." Human pathology **42**(7): 947-953.

Flaherty, K. T., et al. (2010). "Inhibition of mutated, activated BRAF in metastatic melanoma." New England Journal of Medicine **363**(9): 809-819.

Fouad, Y. A. and C. Aanei (2017). "Revisiting the hallmarks of cancer." American journal of cancer research **7**(5): 1016.

Fried, G., et al. (1990). "Peptide-containing nerves in the human pregnant uterine cervix: an immunohistochemical study exploring the effect of RU 486 (mifepristone)." Human Reproduction **5**(7): 870-876.

Gabizon, A., et al. (2003). "Pharmacokinetics of pegylated liposomal Doxorubicin: review of animal and human studies." Clinical pharmacokinetics **42**: 419-436.

Gaillard, R., et al. (1984). "RU 486: a steroid with antiglucocorticosteroid activity that only disinhibits the human pituitary-adrenal system at a specific time of day." Proceedings of the National Academy of Sciences **81**(12): 3879-3882.

Gallagher, P. and A. H. Young (2006). "Mifepristone (RU-486) treatment for depression and psychosis: a review of the therapeutic implications." Neuropsychiatric disease and treatment **2**(1): 33-42.

Gardill, B. R., et al. (2012). "Corticosteroid-binding globulin: structure-function implications from species differences." PloS one **7**(12): e52759.

Garris, C. S., et al. (2018). "Successful anti-PD-1 cancer immunotherapy requires T cell-dendritic cell crosstalk involving the cytokines IFN-γ and IL-12." Immunity **49**(6): 1148-1161. e1147.

Goel, N., et al. (2013). "Pregnancy with metastatic gastrointestinal stromal tumor (GIST) on imatinib chemotherapy: an oncologist's nightmare and obstetrician's dilemma." Journal of gastrointestinal cancer **44**: 115-117.

Gomez-Sanchez, C. E. and E. P. Gomez-Sanchez (2022). "Extra-adrenal glucocorticoid and mineralocorticoid biosynthesis." Endocrinology **163**(4): bqac016.

Goodall, S., et al. (2015). "Monoclonal antibody-targeted polymeric nanoparticles for cancer therapy–future prospects." Journal of Chemical Technology & Biotechnology **90**(7): 1169-1176.

Gray-Schopfer, V., et al. (2007). "Melanoma biology and new targeted therapy." Nature **445**(7130): 851-857.

Gray, E. E. and J. G. Cyster (2012). "Lymph node macrophages." Journal of innate immunity **4**(5-6): 424-436.

Greenwald, R. J., et al. (2005). "The B7 family revisited." Annu. Rev. Immunol. **23**: 515-548.

Han, J., et al. (2022). "Inhibition of colony stimulating factor-1 receptor (CSF-1R) as a potential therapeutic strategy for neurodegenerative diseases: opportunities and challenges." Cellular and Molecular Life Sciences **79**(4): 219.

Hanahan, D. and R. A. Weinberg (2011). "Hallmarks of cancer: the next generation." cell **144**(5): 646-674.

Haque, A. R., et al. (2019). "CD206+ tumor-associated macrophages promote proliferation and invasion in oral squamous cell carcinoma via EGF production." Scientific reports **9**(1): 14611.

Hartnell, A., et al. (2001). "Characterization of human sialoadhesin, a sialic acid binding receptor expressed by resident and inflammatory macrophage populations." Blood, The Journal of the American Society of Hematology **97**(1): 288-296.

Hashimoto, D., et al. (2013). "Tissue-resident macrophages self-maintain locally throughout adult life with minimal contribution from circulating monocytes." Immunity **38**(4): 792-804.

Hauschild, A., et al. (2012). "Dabrafenib in BRAF-mutated metastatic melanoma: a multicentre, open-label, phase 3 randomised controlled trial." The Lancet **380**(9839): 358-365.

He, X. and C. Xu (2020). "PD-1: a driver or passenger of T cell exhaustion?" Molecular cell **77**(5): 930-931.

Hobbs, S. K., et al. (1998). "Regulation of transport pathways in tumor vessels: role of tumor type and microenvironment." Proceedings of the National Academy of Sciences **95**(8): 4607-4612.

Hodi, F. S., et al. (2010). "Improved survival with ipilimumab in patients with metastatic melanoma." New England Journal of Medicine **363**(8): 711-723.

Hu, G., et al. (2023). "LAG-3+ tumor-infiltrating lymphocytes ameliorates overall survival in triple-negative breast cancer patients." Frontiers in Oncology **12**: 986903.

Hutloff, A., et al. (1999). "ICOS is an inducible T-cell co-stimulator structurally and functionally related to CD28." Nature **397**(6716): 263-266.

Inder, W. J., et al. (2012). "Evidence for transcript-specific epigenetic regulation of glucocorticoid-stimulated skeletal muscle 11β-hydroxysteroid dehydrogenase-1 activity in type 2 diabetes." Clinical Epigenetics **4**: 1-8.

Ino, Y., et al. (2013). "Immune cell infiltration as an indicator of the immune microenvironment of pancreatic cancer." British journal of cancer **108**(4): 914-923.

Jensen, T. O., et al. (2009). "Macrophage markers in serum and tumor have prognostic impact in American Joint Committee on Cancer stage I/II melanoma." J Clin Oncol **27**(20): 3330-3337.

Jensen, T. O., et al. (2009). "Macrophage Markers in Serum and Tumor Have Prognostic Impact in American Joint Committee on Cancer Stage I/II Melanoma." Journal of Clinical Oncology **27**(20): 3330-3337.

Kadmiel, M. and J. A. Cidlowski (2013). "Glucocorticoid receptor signaling in health and disease." Trends in pharmacological sciences **34**(9): 518-530.

Kalal, B. S., et al. (2017). "Chemotherapy resistance mechanisms in advanced skin cancer." Oncology reviews **11**(1).

Kamphorst, A. O., et al. (2017). "Proliferation of PD-1+ CD8 T cells in peripheral blood after PD-1–targeted therapy in lung cancer patients." Proceedings of the National Academy of Sciences **114**(19): 4993-4998.

Kashyap, A. S., et al. (2020). "Optimized antiangiogenic reprogramming of the tumor microenvironment potentiates CD40 immunotherapy." Proceedings of the National Academy of Sciences **117**(1): 541-551.

Kawasaki, N., et al. (2013). "Targeted delivery of lipid antigen to macrophages via the CD169/sialoadhesin endocytic pathway induces robust invariant natural killer T cell activation." Proceedings of the National Academy of Sciences **110**(19): 7826-7831.

Kleffel, S., et al. (2015). "Melanoma cell-intrinsic PD-1 receptor functions promote tumor growth." cell **162**(6): 1242-1256.

Kling, M., et al. (1989). "Effects of glucocorticoid antagonism with RU 486 on pituitary-adrenal function in patients with major depression: time-dependent enhancement of plasma ACTH secretion." Psychopharmacology Bulletin **25**(3): 466-472.

Kling, M. A., et al. (1993). "Effects of the glucocorticoid antagonist RU 486 on pituitary-adrenal function in patients with anorexia nervosa and healthy volunteers: enhancement of plasma ACTH and cortisol secretion in underweight patients." Neuroendocrinology **57**(6): 1082-1091.

Landskron, G., et al. (2014). "Chronic inflammation and cytokines in the tumor microenvironment." Journal of immunology research **2014**.

Lee, W. J., et al. (2019). "Prognostic significance of CD163 expression and its correlation with cyclooxygenase-2 and vascular endothelial growth factor expression in cutaneous melanoma." Melanoma research **29**(5): 501-509.

Ligr, M., et al. (2012). "Mifepristone inhibits GRβ coupled prostate cancer cell proliferation." The Journal of urology **188**(3): 981-988.

Lin, E. Y. and J. W. Pollard (2007). "Tumor-associated macrophages press the angiogenic switch in breast cancer." Cancer research **67**(11): 5064-5066.

Long, G. V., et al. (2015). "Dabrafenib and trametinib versus dabrafenib and placebo for Val600 BRAF-mutant melanoma: a multicentre, double-blind, phase 3 randomised controlled trial." The Lancet **386**(9992): 444-451.

Lu, J., et al. (2015). "Progesterone-induced activation of membrane-bound progesterone receptors in murine macrophage cells." The Journal of endocrinology **224**(2): 183.

Mahata, B., et al. (2020). "Tumors induce de novo steroid biosynthesis in T cells to evade immunity." Nature communications **11**(1): 3588.

Mahata, B., et al. (2014). "Single-cell RNA sequencing reveals T helper cells synthesizing steroids de novo to contribute to immune homeostasis." Cell reports **7**(4): 1130-1142.

Mantovani, A., et al. (2017). "Tumour-associated macrophages as treatment targets in oncology." Nature reviews Clinical oncology **14**(7): 399-416.

Manzanares, D. and V. Ceña (2020). "Endocytosis: the nanoparticle and submicron nanocompounds gateway into the cell." Pharmaceutics **12**(4): 371.

Martinez, F. O. and S. Gordon (2014). "The M1 and M2 paradigm of macrophage activation: time for reassessment." F1000prime reports **6**.

Matsumura, Y. and H. Maeda (1986). "A new concept for macromolecular therapeutics in cancer chemotherapy: mechanism of tumoritropic accumulation of proteins and the antitumor agent smancs." Cancer research **46**(12_Part_1): 6387-6392.

Mayer, L. D., et al. (1989). "Influence of vesicle size, lipid composition, and drug-to-lipid ratio on the biological activity of liposomal doxorubicin in mice." Cancer research **49**(21): 5922-5930.

Meeth, K., et al. (2016). "The YUMM lines: a series of congenic mouse melanoma cell lines with defined genetic alterations." Pigment cell & melanoma research **29**(5): 590-597.

Mehnert, W. and K. Mäder (2012). "Solid lipid nanoparticles: production, characterization and applications." Advanced drug delivery reviews **64**: 83-101.

Melo, L. M. N., et al. (2023). "Glucocorticoid activation by HSD11B1 limits T cell-driven interferon signaling and response to PD-1 blockade in melanoma." Journal for Immunotherapy of Cancer **11**(4).

Menzies, F. M., et al. (2011). "Selective inhibition and augmentation of alternative macrophage activation by progesterone." Immunology **134**(3): 281-291.

Metzger, T. C., et al. (2016). "ICOS Promotes the Function of CD4+ effector T Cells during Anti-OX40–mediated tumor rejection." Cancer research **76**(13): 3684-3689.

Miller, L., et al. (1996). "Progesterone inhibits inducible nitric oxide synthase gene expression and nitric oxide production in murine macrophages." Journal of Leucocyte Biology **59**(3): 442-450.

Miller, L. and J. S. Hunt (1996). "Sex steroid hormones and macrophage function." Life sciences **59**(1): 1-14.

Miller, W. L. (2013). "Steroid hormone synthesis in mitochondria." Molecular and cellular endocrinology **379**(1-2): 62-73.

Mills, C. D., et al. (2000). "M-1/M-2 macrophages and the Th1/Th2 paradigm." The Journal of immunology **164**(12): 6166-6173.

Movahedi, K. and J. A. Van Ginderachter (2016). "The ontogeny and microenvironmental regulation of tumor-associated macrophages." Antioxidants & redox signaling **25**(14): 775-791.

Munn, D. H. and A. L. Mellor (2007). "Indoleamine 2,3-dioxygenase and tumor-induced tolerance." Journal of Clinical Investigation **117**(5): 1147-1154.

Muzumdar, M. D., et al. (2007). "A global double-fluorescent Cre reporter mouse." genesis **45**(9): 593-605.

Nair, A. B. and S. Jacob (2016). "A simple practice guide for dose conversion between animals and human." Journal of basic and clinical pharmacy **7**(2): 27.

Nauwynck, H., et al. (1999). "Entry of porcine reproductive and respiratory syndrome virus into porcine alveolar macrophages via receptor-mediated endocytosis." Journal of General Virology **80**(2): 297-305.

Ngoune, R., et al. (2016). "Accumulating nanoparticles by EPR: A route of no return." Journal of controlled release **238**: 58-70.

Nirschl, C. J. and C. G. Drake (2013). "Molecular pathways: coexpression of immune checkpoint molecules: signaling pathways and implications for cancer immunotherapy." Clinical cancer research **19**(18): 4917-4924.

Panettieri, R. A., et al. (2019). "Non-genomic effects of glucocorticoids: an updated view." Trends in pharmacological sciences **40**(1): 38-49.

Paolillo, M. and S. Schinelli (2019). "Extracellular matrix alterations in metastatic processes." International Journal of Molecular Sciences **20**(19): 4947.

Picard, M., et al. (2018). "An energetic view of stress: Focus on mitochondria." Frontiers in neuroendocrinology **49**: 72-85.

Platz, A., et al. (2008). "Human cutaneous melanoma; a review of NRAS and BRAF mutation frequencies in relation to histogenetic subclass and body site." Molecular oncology **1**(4): 395-405.

Pognan, F., et al. (2022). "Liver enzyme delayed clearance in rat treated by CSF1 receptor specific antagonist Sotuletinib." Current Research in Toxicology **3**: 100091.

Pol, J., et al. (2016). First oncolytic virus approved for melanoma immunotherapy, Taylor & Francis. **5:** e1115641.

Postow, M. A., et al. (2015). "Nivolumab and ipilimumab versus ipilimumab in untreated melanoma." New England Journal of Medicine **372**(21): 2006-2017.

Priya, S., et al. (2022). "Surface modification of lipid-based nanocarriers: A potential approach to enhance targeted drug delivery." ACS omega **8**(1): 74-86.

Qian, B.-Z., et al. (2011). "CCL2 recruits inflammatory monocytes to facilitate breast-tumour metastasis." Nature **475**(7355): 222-225.

Ravnan, M. C. and M. S. Matalka (2012). "Vemurafenib in patients with BRAF V600E mutation–positive advanced melanoma." Clinical therapeutics **34**(7): 1474-1486.

Ries, C. H., et al. (2014). "Targeting tumor-associated macrophages with anti-CSF-1R antibody reveals a strategy for cancer therapy." Cancer cell **25**(6): 846-859.

Robert, C., et al. (2015). "Pembrolizumab versus ipilimumab in advanced melanoma." New England Journal of Medicine **372**(26): 2521-2532.

Rocamora-Reverte, L., et al. (2017). "T-cell autonomous death induced by regeneration of inert glucocorticoid metabolites." Cell death & disease **8**(7): e2948-e2948.

Rodriguez, P. C., et al. (2004). "Arginase I production in the tumor microenvironment by mature myeloid cells inhibits T-cell receptor expression and antigen-specific T-cell responses." Cancer research **64**(16): 5839-5849.

Rotte, A., et al. (2018). "Nobel committee honors tumor immunologists." Journal of Experimental & Clinical Cancer Research **37**(1): 1-3.

Ruffell, B., et al. (2014). "Macrophage IL-10 blocks CD8+ T cell-dependent responses to chemotherapy by suppressing IL-12 expression in intratumoral dendritic cells." Cancer cell **26**(5): 623-637.

Sakuishi, K., et al. (2010). "Targeting Tim-3 and PD-1 pathways to reverse T cell exhaustion and restore anti-tumor immunity." Journal of Experimental Medicine **207**(10): 2187-2194.

Salmaso, S. and P. Caliceti (2013). "Stealth properties to improve therapeutic efficacy of drug nanocarriers." Journal of drug delivery **2013**.

Scherholz, M. L., et al. (2019). "Chronopharmacology of glucocorticoids." Advanced drug delivery reviews **151**: 245-261.

Scherphof, G. L., et al. (1994). "Intrahepatic distribution of long-circulating liposomes containing polyethylene glycol) distearoyl phosphatidylethanolamine." Journal of liposome research **4**(1): 213-228.

Schreiber, R. D., et al. (2011). "Cancer immunoediting: integrating immunity's roles in cancer suppression and promotion." Science **331**(6024): 1565-1570.

Shtivelman, E., et al. (2014). "Pathways and therapeutic targets in melanoma." Oncotarget **5**(7): 1701.

Sidler, D., et al. (2011). "Colon cancer cells produce immunoregulatory glucocorticoids." Oncogene **30**(21): 2411-2419.

Slominski, R. M., et al. (2020). "Extra-adrenal glucocorticoid biosynthesis: implications for autoimmune and inflammatory disorders." Genes & Immunity **21**(3): 150-168.

Stahn, C. and F. Buttgereit (2008). "Genomic and nongenomic effects of glucocorticoids." Nature clinical practice Rheumatology **4**(10): 525-533.

Steiniger, B., et al. (1997). "The species-specific structure of microanatomical compartments in the human spleen: strongly sialoadhesin-positive macrophages occur in the perifollicular zone, but not in the marginal zone." Immunology **92**(2): 307-316.

Strachan, D. C., et al. (2013). "CSF1R inhibition delays cervical and mammary tumor growth in murine models by attenuating the turnover of tumor-associated macrophages and enhancing infiltration by CD8+ T cells." Oncoimmunology **2**(12): e26968.

Sun, D., et al. (2020). "CD86+/CD206+ tumor-associated macrophages predict prognosis of patients with intrahepatic cholangiocarcinoma." PeerJ **8**: e8458.

Sun, K., et al. (2002). "Intracrine induction of 11β-hydroxysteroid dehydrogenase type 1 expression by glucocorticoid potentiates prostaglandin production in the human chorionic trophoblast." Biology of reproduction **67**(5): 1450-1455.

Swatler, J., et al. (2023). "Tumors recycle glucocorticoids to drive Treg-mediated immunosuppression." The Journal of clinical investigation **133**(18).

Swenson, C., et al. (2001). "Liposome technology and the development of Myocet™(liposomal doxorubicin citrate)." The Breast **10**: 1-7.

Tang, H., et al. (2018). "PD-L1 on host cells is essential for PD-L1 blockade–mediated tumor regression." Journal of Clinical Investigation **128**(2): 580-588.

Taves, M. D., et al. (2011). "Extra-adrenal glucocorticoids and mineralocorticoids: evidence for local synthesis, regulation, and function." American Journal of Physiology-Endocrinology and Metabolism **301**(1): E11-E24.

Taves, M. D., et al. (2023). "Tumors produce glucocorticoids by metabolite recycling, not synthesis, and activate Tregs to promote growth." The Journal of clinical investigation **133**(18).

Testori, A., et al. (2009). "Surgery and radiotherapy in the treatment of cutaneous melanoma." Annals of oncology **20**: vi22-vi29.

Topalian, S. L., et al. (2012). "Targeting the PD-1/B7-H1(PD-L1) pathway to activate anti-tumor immunity." Current Opinion in Immunology **24**(2): 207-212.

Torchilin, V., et al. (2001). "p-Nitrophenylcarbonyl-PEG-PE-liposomes: fast and simple attachment of specific ligands, including monoclonal antibodies, to distal ends of PEG chains via p-nitrophenylcarbonyl groups." Biochimica et Biophysica Acta (BBA)-Biomembranes **1511**(2): 397-411.

Tronche, F., et al. (1999). "Disruption of the glucocorticoid receptor gene in the nervous system results in reduced anxiety." Nature genetics **23**(1): 99-103.

Tuckermann, J. P., et al. (2007). "Macrophages and neutrophils are the targets for immune suppression by glucocorticoids in contact allergy." The Journal of clinical investigation **117**(5): 1381-1390.

Tumeh, P. C., et al. (2014). "PD-1 blockade induces responses by inhibiting adaptive immune resistance." Nature **515**(7528): 568-571.

Ugurel, S., et al. (2017). "Survival of patients with advanced metastatic melanoma: the impact of novel therapies–update 2017." European Journal of Cancer **83**: 247-257.

van Dinther, D., et al. (2019). "Activation of CD8+ T cell responses after melanoma antigen targeting to CD169+ antigen presenting cells in mice and humans." Cancers **11**(2): 183.

van Dinther, D., et al. (2018). "Functional CD169 on macrophages mediates interaction with dendritic cells for CD8+ T cell cross-priming." Cell reports **22**(6): 1484-1495.

Van Dinther, D., et al. (2018). "Comparison of protein and peptide targeting for the development of a CD169-based vaccination strategy against melanoma." Frontiers in immunology **9**: 1997.

Veniant, M., et al. (2009). "Time of the day for 11β-HSD1 inhibition plays a role in improving glucose homeostasis in DIO mice." Diabetes, Obesity and Metabolism **11**(2): 109-117.

Verma, S. and P. Utreja (2019). "Vesicular nanocarrier based treatment of skin fungal infections: Potential and emerging trends in nanoscale pharmacotherapy." Asian journal of pharmaceutical sciences **14**(2): 117-129.

Wang, B., et al. (2011). "Transition of tumor-associated macrophages from MHC class II hi to MHC class II low mediates tumor progression in mice." BMC immunology **12**: 1-12.

Wang, H.-W. and J. A. Joyce (2010). "Alternative activation of tumor-associated macrophages by IL-4: priming for protumoral functions." Cell cycle **9**(24): 4824-4835.

Wang, S., et al. (2020). General and direct method for preparing oligonucleotide-functionalized metal-organic framework nanoparticles. Spherical Nucleic Acids, Jenny Stanford Publishing**:** 671-682.

Wang, Y., et al. (2012). "Mifepristone-inducible caspase-1 expression in mouse embryonic stem cells eliminates tumor formation but spares differentiated cells in vitro and in vivo." Stem Cells **30**(2): 169-179.

Wempe, S. L., et al. (2013). "Synergistic lethality of mifepristone and LY294002 in ovarian cancer cells." Cancer growth and metastasis **6**: CGM. S11124.

White, P. C., et al. (1997). "11β-Hydroxysteroid dehydrogenase and its role in the syndrome of apparent mineralocorticoid excess." Pediatric research **41**(1): 25-29.

Wynn, T. A., et al. (2013). "Macrophage biology in development, homeostasis and disease." Nature **496**(7446): 445-455.

Wyrwoll, C. S., et al. (2011). "11β-hydroxysteroid dehydrogenases and the brain: from zero to hero, a decade of progress." Frontiers in neuroendocrinology **32**(3): 265-286.

Xu, G., et al. (2021). "The Ratio of CD86+/CD163+ Macrophages Predicts Postoperative Recurrence in Stage II-III Colorectal Cancer." Frontiers in immunology **12**: 724429.

Xu, M., et al. (2021). "Role of the CCL2-CCR2 signalling axis in cancer: mechanisms and therapeutic targeting." Cell proliferation **54**(10): e13115.

Yamada, S., et al. (2002). "Involvement of CD27/CD70 interactions in antigen-specific cytotoxic T-lymphocyte (CTL) activity by perforin-mediated cytotoxicity." Clinical & Experimental Immunology **130**(3): 424-430.

Yang, H., et al. (2019). "Stress–glucocorticoid–TSC22D3 axis compromises therapy-induced antitumor immunity." Nature medicine **25**(9): 1428-1441.

Yang, H., et al. (2020). "CCL2-CCR2 axis recruits tumor associated macrophages to induce immune evasion through PD-1 signaling in esophageal carcinogenesis." Molecular Cancer **19**: 1-14.

Yang, L. and Y. Zhang (2017). "Tumor-associated macrophages, potential targets for cancer treatment." Biomarker research **5**: 1-6.

Zen, M., et al. (2011). "The kaleidoscope of glucorticoid effects on immune system." Autoimmunity reviews **10**(6): 305-310.

Zhang, B., et al. (2011). "M2-polarized tumor-associated macrophages are associated with poor prognoses resulting from accelerated lymphangiogenesis in lung adenocarcinoma." Clinics **66**(11): 1879-1886.

Zhigaltsev, I. V., et al. (2012). "Bottom-up design and synthesis of limit size lipid nanoparticle systems with aqueous and triglyceride cores using millisecond microfluidic mixing." Langmuir **28**(7): 3633-3640.

Zhong, W., et al. (2020). "Comparison of the molecular and cellular phenotypes of common mouse syngeneic models with human tumors." Bmc Genomics **21**: 1-17.

Zhou, Y., et al. (2007). "Impact of single-chain Fv antibody fragment affinity on nanoparticle targeting of epidermal growth factor receptor-expressing tumor cells." Journal of molecular biology **371**(4): 934-947.

Zhu, Y., et al. (2017). "Tissue-resident macrophages in pancreatic ductal adenocarcinoma originate from embryonic hematopoiesis and promote tumor progression." Immunity **47**(2): 323-338. e326.

8 Acknowledgments

I would like to thank all those who made this doctoral thesis possible and supported it. My work was conducted under the supervision of Prof. Dr. med. Astrid Schmieder (Dermatology, University Hospital Würzburg) in the Department of Dermatology, Medical Faculty Mannheim of Heidelberg University, and financed by the Research Training Group 2099 “Hallmarks of Skin Cancer”, Deutsche Forschungsgemeinschaft (DFG). The development of lipid nanoparticles was conducted at the Department of Biomedicine, Aarhus University, under supervision of Prof. Dr. Anders Etzerodt. I would like to thank everyone who supported my work: Prof. Dr. Anders Etzerodt (Aarhus University) and Prof. Dr. Toby Lawrence (King’s College London) provided the CD163-cre mouse. Anders Etzerodt also produced the CD169 antibodies and provided valuable support in formulation development and testing of lipid nanoparticles. Rikke Kongsgaard Rasmussen (Aarhus University) and Henriette Mathiesen (Aarhus University) significantly contributed to the process of nanoparticle formulations, functionalizing antibodies and conjugating them to nanoparticles. Furthermore, Morgane Moulan (Aarhus University) provided help in the animal facility and during general lab work. Rebekka Bitsch (Clinical Cooperation Unit Dermato-Oncology, Medical Faculty Mannheim of Heidelberg University) developed the protocol for T cell activation and Feyza Gul Ozbay Kurt (Clinical Cooperation Unit Dermato-Oncology, Medical Faculty Mannheim of Heidelberg University) helped to establish the assay of BMDM mediated suppression of T cell proliferation. Stephanie Uhlig from the FlowCore Mannheim provided valuable support during FACS measurements and analysis. Güllü Davarci (Molecular Imaging and Radiochemistry, Medical Faculty Mannheim of Heidelberg University) provided access and help in setting up HPLC measurements of nanoparticles and Noémie Laurent (Department of Urology, Medical Faculty Mannheim of Heidelberg University) provided support with nanoparticle tracking analysis. Ana Stojanovic (Department of Immunobiochemistry, Medical Faculty Mannheim of Heidelberg University) helped with the analysis of B16-F10*luc2* tumour at the LSR Fortessa. Furthermore, Raquel Baccetto (Dermatologie, Medical Faculty Mannheim of Heidelberg University), Dr. Kai Schledzewski (Dermatologie, Medical Faculty Mannheim of Heidelberg University) and Marcel Müller (Dermatologie, Medical Faculty Mannheim of Heidelberg University) helped with breeding multiple mouse lines. Raquel Baccetto also provided valuable support during general lab work. Finally, I would like to thank Prof. Dr. med. Astrid Schmieder and Prof. Dr. Viktor Umanksy (Clinical Cooperation Unit Dermato-Oncology, Medical Faculty Mannheim of Heidelberg University) for their support during my work.